Spin - photon entanglement with NV center in diamond for quantum repeater applications

Von der Fakultät 8 Mathematik und Physik der Universität Stuttgart
zur Erlangung der Würde eines Doktors der Naturwissenschaften
(Dr. rer. nat.) genehmigte Abhandlung

Vorgelegt von

DZHAVID DZHAVADZADE

aus Baku, Aserbaidschan

Hauptberichter:	Prof. Dr. Jörg Wrachtrup
Mitberichter:	Prof. Dr. Peter Michler
Tag der mündlichen Prüfung:	13. September 2024

3. Physikalisches Institut

Universität Stuttgart

2024

Contents

List of Abbreviations and Figures

AOM - Acousto-optical modulator
APD - Avalanche photo detector
AWG -Arbitrary waveform generator
CNOT - Controlled NOT quantum gate
EOM - Electro-optical modulator
EOD - Electro-optical deflector
FID - Free induction decay
FPGA - Field-programmable gate array
ISC - Intersystem crossing
MW - Microwave
NV center - Nitrogen- Vacancy center
ODMR - Optically detected magnetic resonance
PLE - Photoluminescence emission
PM - Polarization maintaining
PSB - Phonon side bands
RF - Radio frequency
SSR - Single shot readout
UMZI - Unbalanced Mach-Zehnder interferometer
ZFS - Zero Field Splitting
ZPL - Zero phonon line

List of Figures

Summary

From a technological development perspective, humanity has made significant advancements since the mid-20th century. This progress began with the creation of new technologies used in production, data processing, simulations, medicine, and other aspects of daily life. We are now on the verge of another technological revolution, which will change the world fundamentally. The maturation of quantum technologies is moving them from experimental laboratories to industrial applications. The growing interest from corporations and national governments highlights this shift.

Quantum communication lines, or quantum Internet, are one of the promising technologies of the future. Beyond secure communication, the quantum Internet could facilitate cloud computing on quantum computers or distributed computing across multiple quantum devices. Additionally, there are potential applications in enhancing the sensitivity of telescopes, synchronizing clocks for improved GPS accuracy, and other uses that are yet to be discovered.

Quantum repeaters, leveraging the phenomenon of spin-photon entanglement, are crucial for the practical implementation of quantum technologies. The key to their operation is the fundamental quantum entanglement effect between quantum memory and a flying qubit - a photon. Among the platforms capable of generating such a spin-photon entanglement, the NV centers stand out due to their excellent coherent properties and high state readout efficiency. The adjacent nuclear spins

in NV centers further expand their potential applications. It should be mentioned that the NV center has drawbacks such as spectral diffusion, especially in a cavity, and a low Debye-Waller factor. However, it is a good tool for initial spin-photon entanglement experiments, paving the way to other platforms that might be better suited for this purpose.

In this work, the experimentally robust spin state - photon' time bin' type of entanglement was demonstrated, a critical component for constructing a quantum network. The entangled state was generated and verified first with the electron spin of the NV center and later with the intrinsic nuclear ^{14}N spin. For both cases, the entangled state was measured in ZZ and, which is more complex, in XX basis. For this, an unbalanced Mach-Zehnder interferometer (UMZI) was utilized to control the phase of the photonic qubit, enabling the conversion of temporal modes into spatial ones and facilitating phase adjustments. The standard approach to converting temporal photon states into spatial ones was modified, doubling the conversion rate due to the efficient routing of photons - achieved by replacing the passive Beam Splitter with an active Electro-Optical Deflector (EOD) at the input of the UMZI.

Because of the strong interaction with the electron spin of the NV center, nuclear ^{14}N spin is not the best candidate for the quantum memory role. Alternatively,^{13}C spins from the surrounding environment, emerging as promising candidates. These spins offer superior coherence times and the potential for use in quantum error correction schemes, enhancing the robustness and reliability of quantum information storage. Initial steps have been taken to characterize the spin bath environment, identifying two ^{13}C spins with coupling strengths in the range of 10-100 kHz. These preliminary findings underscore the viability of ^{13}C spins as a quantum memory medium, providing a foundation for further investigation and optimization.

Finally, all experiments related to entanglement have a relatively low rate, so to collect sufficient data, the setup must work stable for a long time. It is also worth

noting that measurements on a XX basis are very sensitive to the photon phase, which imposes additional requirements on the setup. To achieve this, great efforts were put into developing a stable code with on-the-fly calibration of all transitions, monitoring the state of the NV center, as well as effective data management. Despite the difficulties mentioned, the setup was assembled and debugged, which allowed all the measurements mentioned above to be performed.

Zusammenfassung

Aus Sicht der technologischen Entwicklung hat die Menschheit seit Mitte des 20. Jahrhunderts bedeutende Fortschritte gemacht. Dieser Fortschritt begann mit der Etablierung neuer Technologien, in verschiedenesten Bereichen, wie zum Beispiel Produktion, Datenvearbeitung, Simulation und Medizin. Nun stehen wir vor einer weiteren technologischen Revolution, die die Welt grundlegend verändern wird.

Unterschiedlichste Quantentechnologien stehen zur Zeit an der Schwelle zwischen universitärer Grundlagenforschung und industrieller Anwendung.

Zwei der vielversprechendsten Technologien in diesem Zusammenhang stellen Quantenkommunikation und Quanteninternet dar. Neben der sicheren Kommunikation könnte das Quanteninternet das Cloud Computing auf Quantencomputern oder das dezentrale Rechnen auf mehreren Quantengeräten erleichtern. Darüber hinaus gibt es potenzielle Anwendungen zur Erhöhung der Empfindlichkeit von Teleskopen, zur Synchronisierung von Uhren für eine verbesserte GPS-Genauigkeit und viele weitere, bisher unentdeckte, Anwendungsgebiete.

Quanten-Repeater, die sich das Phänomen der Spin-Photonen-Verschränkung zunutze machen, sind für die praktische Umsetzung von Quantentechnologien von entscheidender Bedeutung. Der Schlüssel zu ihrer Funktion ist der grundlegende Quantenverschränkungseffekt zwischen einem Quantenspeicher und einem mobilen Qubit - einem Photon. Unter den Plattformen, die in der Lage sind, eine solche Spin-Photonen-Verschränkung zu erzeugen, stechen die NV-Zentren aufgrund ihrer

hervorragenden kohärenten Eigenschaften und ihrer hohen Ausleseeffizienz hervor. Die benachbarten Kernspins in NV-Zentren erweitern ihr Anwendungspotenzial noch weiter. Hierbei soll erwähnt werden, dass NV-Zentren auch Nachteile haben, wie z. B. spektrale Diffusion, insbesondere in einem Hohlraum, und einen niedrigen Debye-Waller-Faktor. Trotzdem eignet sich das NV-Zentrum als Plattform für erste spin-Photonen-Verschränkungsexperimente und ebnet den Weg für andere Plattformen, die für diesen Zweck besser geeignet sein könnten.

In dieser Arbeit wurde die experimentell robuste Spin-Zustand-Photon-Zeitbin-Verschränkung demonstriert, die eine entscheidende Komponente für den Aufbau eines Quantennetzwerks darstellt. Der verschränkte Zustand wurde zunächst mit dem Elektronenspin des NV-Zentrums und später mit dem intrinsischen Kernspin 14N erzeugt und verifiziert. In beiden Fällen wurde der verschränkte Zustand in der ZZ- und, was komplexer ist, in der XX-Basis gemessen. Dazu wurde ein unausgeglichenes Mach-Zehnder-Interferometer (UMZI) verwendet, um die Phase des photonischen Qubits zu kontrollieren, was die Umwandlung von zeitlichen in räumliche Modi ermöglicht und die Phasenanpassung erleichtert. Der Standardansatz zur Umwandlung von zeitlichen in räumliche Photonenzustände wurde modifiziert und die Umwandlungsrate aufgrund der effizienten selektiven Verteilung der Photonen verdoppelt, indem der passive Strahlteiler durch einen aktiven elektrooptischen Deflektor (EOD) am Eingang des UMZI ersetzt wurde.

Wegen der starken Wechselwirkung mit dem Elektronenspin des NV-Zentrums ist der Kernspin 14N nicht der beste Kandidat für die Rolle des Quantenspeichers. Als vielversprechende Alternative kommen 13C-Spins aus der Umgebung des NV-Zentrums in Frage. Diese Spins bieten längere Kohärenzzeiten und das Potenzial für den Einsatz in Quantenfehlerkorrekturschemata, wodurch die Robustheit und Zuverlässigkeit der Quanteninformationsspeicherung erhöht wird. Es wurden erste Schritte zur Charakterisierung der Spinbadumgebung unternommen und zwei

13C-Spins mit Kopplungsstärken im Bereich von 10-100 kHz identifiziert. Diese vorläufigen Ergebnisse unterstreichen die Eignung von 13C-Spins als Quantenspeichermedium und bilden eine Grundlage für weitere Untersuchungen und Optimierungen.

Generell ist die Zählrate aller Experimente im Zusammenhang mit Quantenverschränkung relativ gering. Deshalb sind die Anforderungen an Stabilität und Robustheit des experimentellen Aufbaus über einen langen Zeitraum sehr hoch, um genügend Messdaten zu sammeln. Außerdem reagieren Messungen in XX-Basis sehr empfindlich auf die Photonenphase, weshalb auch für diese Experimente hohe Sabilitätsanforderungen vom experimentellen Aufbau erüllt werden müssen. Um diese Anforderungen zu erfüllen wurde ein großer Fokus auf die Entwicklung eines robuste Programmierung des Experiments gelegt, inklusive automatisierter spektraler Verfolgung der Übergangsfrequenzen, Überwachung des NV-Zustands und effektiven Datenmanagement. Trotz der genannten Schwierigkeiten konnte der experimentelle Aufbau realisiert und getestet werden, sodass alle oben genannten Messungen erfolgreich durchgeführt werden konnten.

Chapter 1

Introduction to Entanglement

This chapter will discuss an essential concept of quantum entanglement - a cornerstone of quantum mechanics and a crucial element in quantum communications. The historical development of the idea, starting with the foundational work on the EPR paradox and the subsequent formulation of Bell's inequality, will be mentioned. These concepts have shaped our understanding of quantum mechanics and reality and laid the groundwork for modern quantum communication theories. Some practical methods and knowledge that are important in the context of the experimental work will also be mentioned. The chapter will also discuss several intriguing quantum communication protocols, highlighting their potential applications and their unique advantages over classical methods.

1.1 Separable and Entangled states

Assume there are two qubits $|\psi_A\rangle, |\psi_B\rangle$, system's quantum state should be described. In general, the pure state of the system can be represented as:

$$|\psi_{AB}\rangle = \sum_{i,j} |i\rangle_A |j\rangle_B \tag{1.1}$$

where $|i\rangle_A, |j\rangle_B$ are basis states of two qubits. If the state of two a qubits-system can be factorized as a tensor product of individual state $|\psi_{AB}\rangle = |\psi_A\rangle \otimes |\psi_B\rangle$, then the state $|\psi_{AB}\rangle$ is called separable, otherwise entangled [119]. The textbook example of the entangled states is Bell states [99]:

$$\begin{aligned}
\left|\Phi^+\right\rangle &= \frac{1}{\sqrt{2}}(|0\rangle_A |0\rangle_b + |1\rangle_A |1\rangle_B) \\
\left|\Phi^-\right\rangle &= \frac{1}{\sqrt{2}}(|0\rangle_A |0\rangle_b - |1\rangle_A |1\rangle_B) \\
\left|\Psi^+\right\rangle &= \frac{1}{\sqrt{2}}(|0\rangle_A |1\rangle_b + |1\rangle_A |0\rangle_B) \\
\left|\Psi^-\right\rangle &= \frac{1}{\sqrt{2}}(|0\rangle_A |1\rangle_b - |1\rangle_A |0\rangle_B)
\end{aligned}$$

It can be shown that Bell states form the basis for a qubits system. The measurement of individual qubits is mathematically described by partial trace operation,

$$\rho_A = \sum_j (I_A \otimes \langle j|_B)(|\psi_{AB}\rangle \langle\psi_{AB}|)(I_A \otimes |j\rangle_B) \tag{1.2}$$

applying projecting operator to one of the qubits. It can be shown, that when individual measurements are performed in the z-basis on entangled qubits in a state such as $|\Phi^+\rangle$, the resulting individual density matrices will be equal to the maximally mixed state $\rho_A = \rho_B = \frac{1}{2}(|0\rangle\langle 0| + |1\rangle\langle 1|)$, but at the same time the results itself will be correlated. Even when separated by large distances, this mutual dependence between particles persists. When one particle's property is measured, the entangled state of the other particle instantaneously changes, which may be in logical contradiction with the principle of locality. However, it is crucial to understand that no information travels between them. So, even though it seems counterintuitive, the theory of relativity still holds.

Another feature, specifically important for this thesis, is that if one qubit accumulates some phase between its basis states and is measured (traced out in terms of density matrix), the accumulated phase will "stay in the system" and could be measured on another qubit.

In summary, entanglement is a crucial idea in quantum mechanics that significantly affects essential physics and valuable technologies. Studying it has helped to understand quantum mechanics better and could change understanding of computing, communication, and information security.

1.2 Einstein Podolsky Rosen paradox

In general, the measurement procedure for entangled states has non-trivial aspects that have caused well-known discussions in the past. In particular, it is worth mentioning the Einstein Podolsky Rosen paradox [43] [20], where they argued the incompleteness of quantum theory. In the past, the Einstein-Podolsky-Rosen paradox and the following discussion between Bohr and Einstein were significant in explaining important physical ideas like "measurement," "completeness of theory," "physical reality," and "state of a system."

The idea of the paradox is the following: Imagine there are two particles, and they interact from the point of time $t = 0$ until some point of time $t = T$, and suppose there is no interaction between them afterward (for example, they were directed in a different direction). Let us say they have the same coordinate and momentum values but are not known to us. It can arise, for example, during spontaneous parametric scattering, which is the decay of a photon into two others with lower energy. The wave function of the system can be written as:

$$\Psi(x_1, x_2) = \int_{-\infty}^{+\infty} exp\left[(2\pi ih)(x_1 - x_2 + x_0)p\, dp\right] \tag{1.3}$$

where x_0 is some constant. The exact position of the first particle can now be measured and, out of this, the exact position of the second particle can be calculated. Alternatively, one can measure the momentum of the first particle and, this way, calculate the momentum of the second particle - it is important to note that operators of momentum and coordinate are non-commutative, therefore these two values cannot be measured together. In these two different cases, the second particle will be described by two different wave functions, which are eigenfunctions of noncommutating operators. The nonobvious part here is how it is possible that one can influence the second particle, only manipulating the first one. How did it happen that the wave function of the second particle could take different values before it got any "signal" from the first one? To remind - in the special theory of relativity, the signal cannot travel faster than the speed of light, whereas, in the case of two particles, this happens immediately. Does it mean there were some "local hidden parameters" in the system from the beginning, or can quantum mechanics violate the "local realism" principle?

1.3 Bell Inequality

In 1964, John Bell wrote his famous paper "On the Einstein Podolsky Rosen Paradox" [10] [12], which showed that local hidden variable models could not, in general, reproduce predictions of quantum mechanics. In other words, one can conduct serial experiments, the statistical result of which can confirm or disprove the existence of hidden variables in quantum mechanics [13].

There are many equivalent variations of the main idea [25]. Below is a simplified one, that keep the essence [29]:

1. Imagine someone sends messages (via fields, particles etc) far away in some direction
2. Every message has four parameters that could be measured and can take the value ± 1
3. These messages have some statistical distribution at the moment of sending
4. Imagine there are two receivers, "Even" and "Odd", both are located far away, in the same direction from the sender as the messages sent. So that the sender does not know who will receive each of the messages exactly and cannot use this knowledge (which does not exist) to manipulate the statistics of the messages.
5. For each message received, let "Even" receiver "flip a coin" and decide whether to measure parameter number 2 or 4.
6. The "Odd" receiver does the same, but measures parameter 1 or 3
7. This way, the "Even" receiver can calculate the average values of the parameters 2 and 4, and the "Odd" receiver of the parameters 1 and 3.

Let us now introduce the notation A_2, A_4 for the results of measurements done by "Even" receiver and A_1, A_3 by "Odd", and let us consider an expression that includes the results of just one measurement by each observer:

$$A_1A_2 + A_1A_4 + A_3A_2 - A_3A_4$$

This can written as

$$A_1A_2 + A_1A_4 + A_3A_2 - A_3A_4 = A_2(A_1 + A_3) + A_4(A_1 - A_3)$$

Because $A_1 = \pm 1$ and $A_3 = \pm 1$, one of the sums in parentheses is always zero and another is ± 2, taking into account that $A_2 = \pm 1$ and $A_4 = \pm 1$, so that:

$$A_1A_2 + A_1A_4 + A_3A_2 - A_3A_4 = A_2(A_1 + A_3) + A_4(A_1 - A_3) = \pm 2$$

which in turn means that averaging over multiple measurements will give:

$$\langle A_1A_2 + A_1A_4 + A_3A_2 - A_3A_4 \rangle \leq 2$$

Let us also make three following assumptions:

1. ***Realism*** The measurement of one particle does not change or distort initial statistics. The value was always in the message, and the measurement only extracted it without changing it [11]. In other words, the realism principle states that before any measurements are conducted, all objects possess "objectively existing" values for their parameters and characteristics, regardless of the potential measurements that could be performed on them.
   Possible violations could look, for example, as follows: the act of measurement introduces disturbances into the system, changing its state and then measuring

it, giving the value for a new state as an outcome. Moreover, such disturbances are random and have their own probability distribution, which is unrelated to the initial message's probability distribution.

2. ***Locality*** No statistical correlation exists between one receiver's flip-coin decisions (from point 5) and anything (decisions or results) on another receiver. This is true if there is fundamentally no possibility of any connection between two recipients. More generally, the principle of locality (or proximity) asserts that an object is influenced solely by its immediate environment. For an action at one point to impact another point, there must be something in the space between them that mediates the interaction, such as a wave or particle crossing the in-between space.
   If this violation consistently occurs, it implies non-locality. This is because measurements made by "Even" and "Odd" observers may be completely distant from each other in a relativistic sense, with no possibility of cause-and-effect relationships between them.

3. ***Absence of Superdeterminism*** There is no external third force that influences both the Even" and "Odd" "coin toss" at the same time.

   Superdeterminism is the idea that not only the actions of the material world, and not only the behavior and consciousness of individuals, but also the behavior and consciousness of individuals when conducting experiments to understand the material world or interpret their findings, are predetermined or controlled by a higher power. If this point is wrong, the decisions made by two observers may seem random to them. However, in reality, there is a recognizable pattern within this apparent randomness, influenced by a higher force, like the will of God or so. Gerard t'Hooft added this argument in his letter to Bell - Bell's original idea did not contain this point. In his response, Bell agreed that this *idea “breaks” his whole reasoning. Overall, the superdeterminism hypothesis is untestable because it allows for the postulation that certain relationships have existed since the Big Bang.*

Under these assumptions, the law of probability theory can be applied: “The average of the sum is equal to the sum of the averages,” so the formula mentioned above can be rewritten in a form called CHSH inequality [29]

$$|\langle A_1 A_2\rangle + \langle A_1 A_4\rangle + \langle A_3 A_2\rangle - \langle A_3 A_4\rangle| \leq 2 \tag{1.4}$$

If quantum mechanics could be explained by theories involving hidden variables that act locally [47], then the Inequality 1.4 should always be satisfied. Let us prove that it is not a case. For this, consider the sender prepare two particles (qubits) in the entangled state

$$|\Psi\rangle = \frac{|01\rangle - |10\rangle}{2}$$

The ”Odd” receiver measures the observables

$$A_1 = \sigma_z$$
$$A_3 = \sigma_x$$

and the "Even" receiver measures either of the two other observables

$$A_2 = -\frac{\sigma_x + \sigma_z}{\sqrt{2}}$$
$$A_4 = \frac{\sigma_x - \sigma_z}{\sqrt{2}}$$

then, the sender can calculate the quantum expectation value for pairs of these observables using the Born rule and get:

$$\langle A_1 A_2 \rangle = \frac{1}{\sqrt{2}} \qquad \langle A_1 A_4 \rangle = \frac{1}{\sqrt{2}} \qquad \langle A_3 A_2 \rangle = \frac{1}{\sqrt{2}} \qquad \langle A_3 A_4 \rangle = -\frac{1}{\sqrt{2}}$$

so the expression in the Inequality 1.4 will be equal to $2\sqrt{2}$. This value exceeds the classical limit[79], which was based on local realism assumptions [53] [3][57]. Thus, one of the three assumptions is not satisfied. In the most famous "Copenhagen" interpretation [44], realism is sacrificed, making the theory local and not needing to contain superdeterminism. In this interpretation, any measurement, as well as any interaction, disrupts the system's state (known as "wave function collapse") - the system is getting projected into one of the eigenstates with corresponding measured value. The value of a quantity is precisely determined only in eigenstates. In other states, there is merely a probability distribution of what will occur if a measurement is conducted. Einstein, being a supporter of local realism, liked to say in this regard that the Moon does not disappear from the sky, even if no one observes it.
All in all, quantum entanglement is an exceptional and counterintuitive property of quantum particles that makes us think seriously about the structure of our world.

1.4 No-cloning theorem

The fundamental theorem in quantum communication and computing is the No-cloning theorem, which states that it is impossible to create an identical copy of an arbitrary unknown quantum state [140] [34]. If there is some subsystem B in a state $|0_B\rangle$, then to make it a copy of an unknown subsystem A in-state $|\Psi_A\rangle$ or $|\Phi_A\rangle$, there are only two different operations one can perform on the AB system:

1. The system can be either measured and, this way, projected subsystem A onto one of its eigenstates, partially losing information about the initial state of subsystem A (which is a bad scenario)

2. or one can apply some Unitary operator U, such that

$$U|\Psi_A\rangle|0_B\rangle = |\Psi_A\rangle|\Psi_B\rangle$$
$$U|\Phi_A\rangle|0_B\rangle = |\Phi_A\rangle|\Phi_B\rangle$$

for all $|\Psi_A\rangle$ and $|\Phi_A\rangle$. Let us conjugate the second equation and calculate the scalar product:

$$\langle 0_B|\langle\Phi_A|U^\dagger U|\Psi_A\rangle|0_B\rangle = \langle\Phi_B|\langle\Phi_A|\Psi_A\rangle|\Psi_B\rangle$$

thus

$$\langle\Phi|\Psi\rangle = |\langle\Phi|\Psi\rangle|^2$$

which is not true in general (only if $\langle\Phi| = |\Psi\rangle$ or they are orthogonal), so that the no-cloning theorem is proven.

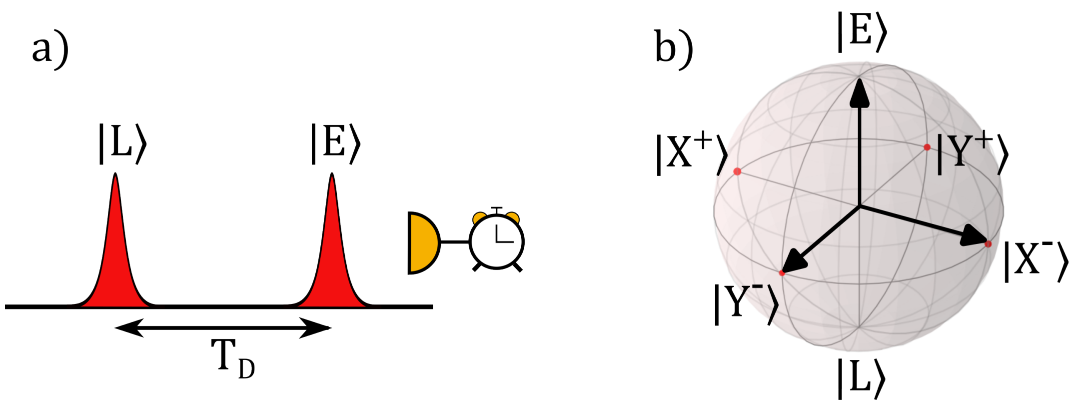

FIGURE 1.1: a) Time bin encoding, $|Early\rangle$ and $|Late\rangle$ photons separated by T_D b) Bloch Sphere for the photon qubit in the basis $\{|Early, Late\rangle\}$

1.5 Time bin entanglement

There are various methods to encode a photon qubit, with polarization being the most well-known [100][131][30]. However, frequency, spatial mode, or photon number [139] can also be encoding techniques. Another noteworthy degree of freedom is the time-bin mode (temporal mode), where basis states are defined by the emission time [129] [136]. This form of entanglement is more robust experimentally and practical than polarization-based entanglement. This practicality arises because modern optical fibers generally do not maintain polarization, making the current fiber infrastructure unsuitable for real-life applications involving polarization-based entanglement.

The photon could be emitted either in time mode $|Early\rangle$ (emission time $t = 0$) or $|Late\rangle$ (emission time after delay $t = T_D$), and these two states are orthogonal, so form a basis [22]. To measure the photon qubit projection to $\langle Z\rangle$ - basis, the detection time of the photon needs to bee measured (see Figure 1.1 a).

The equal superposition state could look like this:

$$|\Psi\rangle = \frac{1}{\sqrt{2}}(|Early\rangle + |Late\rangle e^{i\phi})$$

Where ϕ is the phase between two basis states, and for particular phases, $|X^{\pm}\rangle, |Y^{\pm}\rangle$ can defined as (see Figure 1.1):

$$\begin{aligned} |X^{\pm}\rangle &= \frac{1}{\sqrt{2}}(|E\rangle \pm |L\rangle) \\ |Y^{\pm}\rangle &= \frac{1}{\sqrt{2}}(|E\rangle \pm i\,|L\rangle) \end{aligned}$$

Typically, in experiments, people use an unbalanced Mach-Zehnder interferometer to have control over the phase of the photon and to be able to measure its state in $\langle X\rangle$ or $\langle Y\rangle$ bases Figure 1.2 a). This interferometer has long and short arms, so the length difference is perfectly matched with a time delay between optical pulses: $\Delta L = T_D c$, where c - speed of light (let us assume refractive index equals 1). At the outputs of the interferometer, two detectors measure photon clicks. Plotting a "photons arrival time histogram" results in three distinct peaks (Figure 1.2 b) corresponding to three possible cases

- The earliest click can happen if the photon in $|Early\rangle$ state takes $|Short\rangle$ path
- The latest click happens when the photon in $|Late\rangle$ state takes $|Long\rangle$ path
- In the middle peak, photons in states $|Early, Long\rangle$ or $|Late, Short\rangle$ can be detected.

The middle peak is used - the information "in which time bin the photon was emitted" is erased there. Moreover, spatial modes $|Short\rangle, |Long\rangle$ can now be used instead of

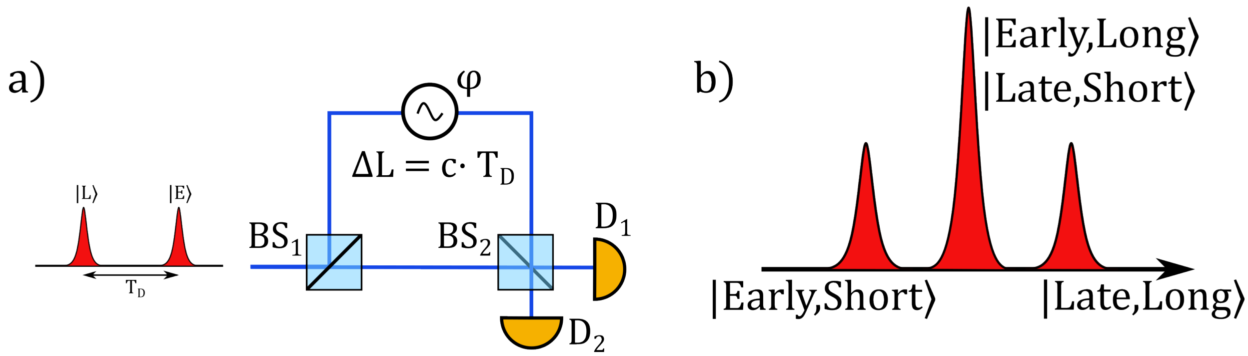

FIGURE 1.2: a) Unbalanced Mach-Zehnder Interferometer to control the photon's phase. The time-bin encoded photon enters the interferometer, and detection happens on the detectors at the output b) Photon arrival time histogram, the mapping of time bins to spatial modes happens in the central peak

temporal modes $|Early\rangle, |Late\rangle$ - because now there is a one-to-one match between them, so basis conversion has happened. On a spatial basis, a photon acquires phase as it propagates. Specifically, for a photon, the phase acquired over a distance equal to its wavelength λ is 2π; this is possible to implement experimentally.

The beam splitter operator looks as $\pi/2$ rotation around X-axis on the Bloch sphere Figure 1.1:

$$\hat{B} = \frac{1}{\sqrt{2}}\begin{pmatrix} 1 & i \\ i & 1 \end{pmatrix} \tag{1.5}$$

The phase acquisition in the long arm of the interferometer with respect to the short arm is quantum mechanically equivalent to rotation around the Z-axis on the Bloch sphere:

$$\hat{L} = \frac{1}{\sqrt{2}}\begin{pmatrix} 1 & o \\ 0 & e^{i\phi} \end{pmatrix} \tag{1.6}$$

So that, overall, the first beam splitter redefines the basis, then before the second one, the rotation around the Z axis on the Bloch Sphere equator is happening, with the following $\pi/2$ rotation around X axis on the second beam splitter. The interference pattern on the second beam splitter depends on the acquired phase ϕ. It is interesting to analyze the $G^{(1)}$ correlation function of the photon clicks on two different spatial modes [22]:

$$G^{(1)} = \langle a_i^\dagger(t) a(t)_i \rangle \tag{1.7}$$

where a_i and $a_i^\dagger$ are annihilation and creation operators of the photon in detectors spatial modes ($i = \{1, 2\}$ for D_1 and D_2 on Figure 1.2 a, respectively). Due to the introduced time delay and relative phase in the long arm of the interferometer, the mode can be defined as follows [102]:

$$a(t) \rightarrow a(t) + e^{i\phi} a(t - T_D) \tag{1.8}$$

with this, the fisrt order correlation $G^{(1)}$ functions reads as follows:

$$\begin{aligned} G^{(1)}(t, \phi) =& \langle a^\dagger(t) a(t) \rangle + e^{-i\phi} \langle a^\dagger(t - T_D) a(t) \rangle + e^{i\phi} \langle a^\dagger(t) a(t - T_D) \rangle + \langle a^\dagger(t - T_D) a(t - T_D) \rangle \\ =& \langle a^\dagger(t) a(t) \rangle + 2\cos(\phi) \| \langle a^\dagger(t) a(t - T_D) \rangle \| + \langle a^\dagger(t - T_D) a(t - T_D) \rangle \end{aligned} \tag{1.9}$$

the three terms correspond to 3 different detection windows. The middle one is the most interesting and only phase-dependent. So introduction of early and late operators $a_E(t) = a(t)$, $a_L(t) = a(t + T)$ and integration over the detection window yields:

$$\int G^{(1)}(t, \phi)\, dt \propto \rho_{EE} + \rho_{LL} + 2\cos(\phi) |\rho_{EL}| \tag{1.10}$$

Sweeping the phase ϕ yields to oscillations with a visibility $V = 2|\rho_{EL}|$. This particularly shows the need for a phase-stabilized interferometer to get better visibility.

1.6 Fidelity estimation, tomography

Let us now discuss how the quality of the prepared state can be measured. Imagine one wants to create a quantum state ρ_{target}, but in reality, due to imperfections and, for example, not ideal quantum gates, one can only create a state ρ_{real}. How to estimate the closeness of these two states? The standard measure is Fidelity, which can be defined for two arbitrary quantum states ρ, σ as follows [99][70]:

$$F(\rho,\sigma) = \left[tr\sqrt{\sqrt{\rho}\sigma\sqrt{\rho}}\right]^2 \tag{1.11}$$

For pure states, for example, $\rho = |\Psi\rangle\langle\Psi|$, the expression simplifies, because pure state is always projector $\sqrt{\rho} = \rho$:

$$F(\rho,\sigma) = \langle\Psi|\,\sigma\,|\Psi\rangle \tag{1.12}$$

and if both states are pure $\rho = |\Psi\rangle\langle\Psi|$, $\sigma = |\Phi\rangle\langle\Phi|$:

$$F(\rho,\sigma) = |\langle\Psi|\Phi\rangle|^2 \tag{1.13}$$

For any quantum states ρ, σ the Quantum state Fidelity satisfies some important properties:

1. **Bounded:** $0 \leq F(\rho,\sigma) \leq 1$
2. **Symmetric:** $F(\rho,\sigma) = F(\sigma,\rho)$
3. **Tensor product Multiplicativity:**
   $F(\rho_1 \otimes \rho_2, \sigma_1 \otimes \sigma_2) = F(\rho_1,\sigma_1) \cdot F(\rho_2,\sigma_2)$
4. **Unitary invariance:** $F(\rho,\sigma) = F(U\rho U^\dagger, U\sigma U^\dagger)$

Let us look more closely at how to calculate Fidelity if one of the states is a pure Bell state [19][16]. In other words, the goal is to estimate "how close the created state ρ^{real} is to the pure Bell state ρ^{Bell}," which is the state to create. For example consider Bell state $|\Psi^+\rangle$:

$$\left|\Psi^+\right\rangle = \frac{1}{\sqrt{2}}(|10\rangle + |01\rangle)$$

The density matrix for this state is

$$\rho_{\Psi^+} = \left|\Psi^+\right\rangle \left\langle\Psi^+\right| = \begin{pmatrix} 0 & 0 & 0 & 0 \\ 0 & 1 & 1 & 0 \\ 0 & 1 & 1 & 0 \\ 0 & 0 & 0 & 0 \end{pmatrix} \tag{1.14}$$

and using the Equation 1.12 with density matrix ρ:

$$F = \left\langle\Psi^+\right| \rho \left|\Psi^+\right\rangle = \frac{1}{2}(\rho_{22} + \rho_{33} + 2Re(\rho_{23})) \tag{1.15}$$

ρ_{22}, ρ_{33} are diagonal elements (populations) that are usually straightforward to measure. The question is how to measure the off-diagonal phase dependent element $Re(\rho_{23})$? To estimate it, one can perform a trick when applying $\pi/2$ rotation around $y - axis$ for both spins, mapping off-diagonal elements to diagonal (effectively, measuring qubit-pair in XX basis).

$$\tilde{\rho} = \left(\sqrt{Y} \otimes \sqrt{Y}\right)\rho\left(\sqrt{Y}^\dagger \otimes \sqrt{Y}^\dagger\right) \tag{1.16}$$

where Y operator is a π-rotation around $y - axis$:

$$\sqrt{Y} = exp\left[-\frac{i}{\hbar} S_y \frac{\pi}{2}\right] \tag{1.17}$$

After this transformation, the contrast between correlations in anti-correlations in XX basis can be represented through off-diagonal elements in ZZ basis as:

$$\tilde{\rho_{11}} + \tilde{\rho_{44}} - \tilde{\rho_{22}} - \tilde{\rho_{33}} = 2Re(\rho_{23}) + 2Re(\rho_{14}) \tag{1.18}$$

From the definition of the density matrix, there is a bound

$$|2Re(\rho_{14})| \leq \sqrt{\rho_{11}\rho_{44}} \tag{1.19}$$

so, the lower bound for $2Re(\rho_{23})$ is:

$$2Re(\rho_{23}) \geq \tilde{\rho_{11}} + \tilde{\rho_{44}} - \tilde{\rho_{22}} - \tilde{\rho_{33}} - 2\sqrt{\rho_{11}\rho_{44}} \tag{1.20}$$

which for Fidelity formula 1.15 gives:

$$F \geq \frac{1}{2}(\rho_{22} + \rho_{33} - 2\sqrt{\rho_{11}\rho_{44}} + \tilde{\rho_{11}} + \tilde{\rho_{44}} - \tilde{\rho_{22}} - \tilde{\rho_{33}}) \tag{1.21}$$

This formula can be used to estimate the lower bound of generated state fidelity when one wants to create Bell state $|\Psi^+\rangle$. Note that the formula has only diagonal elements of 2 density matrices ρ $(ZZ - basis)$ and $\tilde{\rho}$ $(XX - basis)$, which are populations and easy to measure with an NV center system.

1.7 Entanglement as a resource (applications of the entanglement)

Entanglement as a resource is a cornerstone concept in the field of quantum networks, offering a wide range of transformative applications. This section explores how entangled quantum states can be harnessed to enable advanced functionalities that

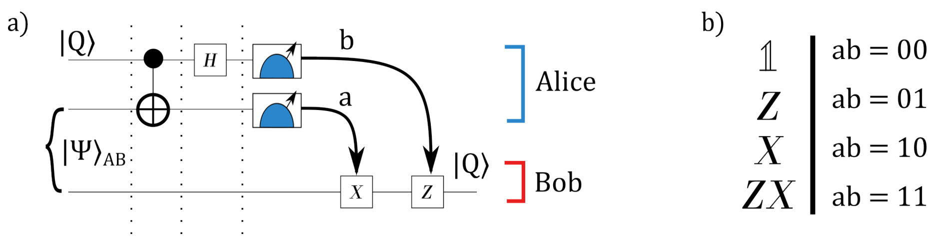

FIGURE 1.3: a) Quantum circuit of the Quantum State Teleportation protocol b) Table of operators that Bob must apply to his qubit depending on the result Alice received

surpass classical limitations. Key applications include quantum key distribution for secure communication [14], quantum teleportation for state transfer without physical transmission [15], the synchronization of quantum clocks [76], telescope-baseline extension [52] or cloud-based quantum computing [24]. By leveraging the unique properties of entanglement, such as non-local correlations and superposition, these applications not only enhance the performance and security of networked systems but also lay the groundwork for the development of a global quantum internet [138].

1.7.1 Quantum State Teleportation

One of the exciting application of the entangled states is the quantum teleportation protocol [21][58], which allows the sender to transmit quantum information to the receiver.

Imagine Alice has a qubit in state $|Q\rangle = \alpha|0\rangle + \beta|1\rangle$, which she wants to send to Bob, but she is only able to send classical information. Additionally, Alice and Bob share entangled pair of qubits $|\Psi\rangle_{AB} = \frac{1}{\sqrt{2}}(|00\rangle + |11\rangle)$.

The experiment diagram is shown on the Figure 1.3 a). Let us follow the system's state after each operation to see how one gets the desired result. The initial state of the system is:

$$|\pi\rangle_0 = |\Psi\rangle_{AB} |Q\rangle = \frac{1}{\sqrt{2}}(\alpha |000\rangle + \alpha |110\rangle + \beta |001\rangle + \beta |111\rangle)$$

, Where the first qubit is Bob's entangled qubit, the second is Alice's entangled qubit, and the third is a qubit, which state one wants to transfer. The state of the system turns into the following one after application of the $CNOT$ operator:

$$|\pi\rangle_1 = \frac{1}{\sqrt{2}}(\alpha |000\rangle + \alpha |110\rangle + \beta |011\rangle + \beta |101\rangle)$$

It can be seen that from now on, the state of the three qubits system is entangled. Then Alice performs Hadamard gate on the third qubit, which makes the state of the system:

$$|\pi\rangle_2 = \frac{1}{\sqrt{2}}(\alpha |00\rangle |+\rangle + \alpha |11\rangle |+\rangle + \beta |01\rangle |-\rangle + \beta |10\rangle |-\rangle) =$$
$$= \frac{1}{2}\Big[\alpha |00\rangle (|0\rangle + |1\rangle) + \alpha |11\rangle (|0\rangle + |1\rangle) + \beta |01\rangle (|0\rangle - |1\rangle) + \beta |10\rangle (|0\rangle - |1\rangle)\Big] =$$
$$= \frac{1}{2}\Big[\alpha |000\rangle + \alpha |001\rangle + \alpha |110\rangle + \alpha |111\rangle + \beta |010\rangle - \beta |011\rangle + \beta |100\rangle - \beta |101\rangle\Big] =$$
$$= \frac{1}{2}\Big[(\alpha |0\rangle + \beta |1\rangle) |00\rangle + (\alpha |0\rangle - \beta |1\rangle) |01\rangle + (\alpha |1\rangle + \beta |0\rangle) |10\rangle + (\alpha |1\rangle - \beta |0\rangle) |11\rangle\Big]$$

Written in such a form, it might seem that α and β now also reflect the state of Bob's qubit, even though no communication between Alice and Bob has happened yet (despite the shared entangled pair before the start of the experiment). This is just because one can freely rearrange scalar trough tensor product. Nevertheless, some interesting insights can be seen already. In the next step, Alice will measure her qubits (numbers 2 and 3 in our notations); it can already be seen that the probabilities of the four possible measurement outcomes are uniform:

$$\begin{aligned}
Pr(ab = 00) =& \frac{1}{4} ||\alpha |0\rangle + \beta |1\rangle ||^2 = \frac{1}{4} \\
Pr(ab = 10) =& \frac{1}{4} ||\alpha |0\rangle - \beta |1\rangle ||^2 = \frac{1}{4} \\
Pr(ab = 01) =& \frac{1}{4} ||\alpha |1\rangle + \beta |0\rangle ||^2 = \frac{1}{4} \\
Pr(ab = 11) =& \frac{1}{4} ||\alpha |1\rangle - \beta |0\rangle ||^2 = \frac{1}{4}
\end{aligned}$$

so, it doesn't depend on $alpha, beta$ - the qubit Alice wants to transmit. It is essential that Alice does not gain any information about the state she wants to transmit - otherwise, it would contradict the no-cloning theorem. First, she destroys the state when measuring it, and second, from her point of view, the measurement outcomes are random bits. Alice then sends these bits to Bob, and Bob performs $X - gate$ if a=1 and $Z - gate$ if b=1 (see Figure 1.3 b). Following this algorithm, Bob always gets on his side the original state

$$\alpha |0\rangle + \beta |1\rangle == |Q\rangle$$

finishing the state teleportation protocol. As was said already, Alice does not have this state anymore, which is mandatory. One can also show that the same calculations are also valid if the qubit $|Q\rangle$ is entangled with some system γ:

$$|Q\rangle_{\gamma} = \alpha |0, \gamma_0\rangle + \beta |1, \gamma_1\rangle$$

To sum up, the protocol shows how, with one distributed entangled qubit pair and two classical bits, one can teleport the quantum state over distance.

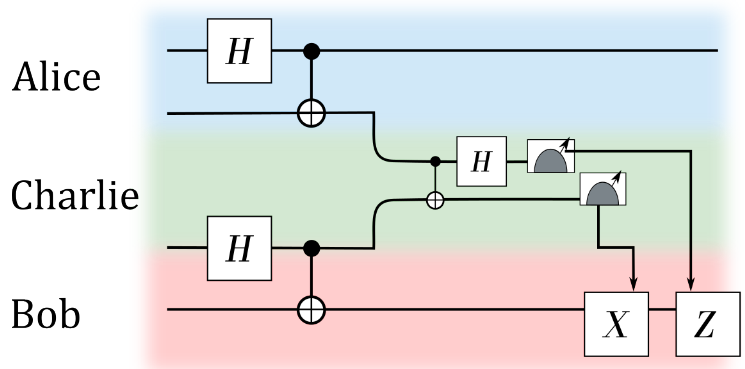

FIGURE 1.4: Quantum diagram of the Entanglement Swapping (entanglement Teleportation) protocol

1.7.2 Entanglement Swapping, Entanglement Teleportation

Quantum Entanglement swapping or Entanglement teleportation is a fascinating and powerful operation underlying scalable quantum communication lines, and more [94][61]. It allows entangling two particles that never interacted in the past by consuming a Bell pair and two bits of classical information. In this protocol, three parties - Alice and Bob want to establish communication, and the intermediate node is Charlie. The protocol consists of 4 parts, see Figure 1.4:

1. **Initial Entanglement** Alice has two qubits $|A, A'\rangle$, which she entangles inside her lab with the consistent use of the Hadamard and CNOT gates. This is a well-known procedure for creating a Bell pair; depending on the initial states

of the two qubits, different Bell states are obtained, namely:

$$|0,0\rangle \rightarrow \left|\Phi^+\right\rangle = \frac{1}{\sqrt{2}}(|00\rangle + |11\rangle)$$
$$|0,1\rangle \rightarrow \left|\Psi^+\right\rangle = \frac{1}{\sqrt{2}}(|01\rangle + |10\rangle)$$
$$|1,0\rangle \rightarrow \left|\Phi^-\right\rangle = \frac{1}{\sqrt{2}}(|00\rangle - |11\rangle)$$
$$|1,1\rangle \rightarrow \left|\Psi^-\right\rangle = \frac{1}{\sqrt{2}}(|01\rangle - |10\rangle)$$

The same thing is done by Bob with his qubits $|B, B'\rangle$, for simplicity, assume they both created state $|\Phi^+\rangle$ and the common state of 4 qubit system is:

$$|\Psi\rangle_{AA'BB'} = \frac{1}{2}\Big[|0000\rangle + |0011\rangle + |1100\rangle + |1111\rangle\Big]$$

Which can be rewritten (notice that qubits positions are also re-ordered):

$$\begin{aligned}|\Psi\rangle_{A'B'AB} = \frac{1}{2\sqrt{2}}\Big[&\left|\Phi^+\right\rangle(|00\rangle + |11\rangle)\\ &+\left|\Psi^+\right\rangle(|01\rangle + |10\rangle)\\ &+\left|\Psi^-\right\rangle(|01\rangle - |10\rangle)\\ &+\left|\Phi^-\right\rangle(|00\rangle - |11\rangle)\Big]\end{aligned} \tag{1.22}$$

2. **Bringing particles together** As second step, they both keep one qubit ($|A\rangle$ and $|B\rangle$) each and send another ($|A'\rangle$ and $|B'\rangle$) to intermediate station Charlie. These particles are then made to interact in a specific way, called a Bell State

Measurement (BSM).

3. **Measurement and Results transfer** BSM is a joint quantum mechanical measurement to determine which of the four Bell states the pair $|A', B'\rangle$ were. The measurement of qubit states happens after the CNOT gate, followed by the Hadamard gate. The mapping rule is the opposite of the rule for Bell states creation:

$$\begin{aligned} \left|\Phi^{+}\right\rangle &\rightarrow |0,0\rangle & \left|\Psi^{+}\right\rangle &\rightarrow |0,1\rangle \\ \left|\Phi^{-}\right\rangle &\rightarrow |1,0\rangle & \left|\Psi^{-}\right\rangle &\rightarrow |1,1\rangle \end{aligned}$$

   So, BSM projects two never interacted with qubits $|A, B\rangle$ to a superposition state, according to Equation 1.22.

4. **New Entanglement Generation** As a last step, the intermediate party Charlie communicates the outcome of the measurement to Bob, who could apply local rotational gates to his qubit $|B\rangle$, to bring the newly entangled pair $|AB\rangle$ to the desired pre-agreed state.

The operation of Entanglement Swapping is very crucial in the development of quantum networks. It allows for the creation of long-distance entanglement, essential for secure communication channels and quantum computing. For example, instead of qubits $|A\rangle$ and $|B\rangle$, one can have quantum memories $|M_1\rangle$ and $|M_2\rangle$, entangled with photons $|A'\rangle$ and $|B'\rangle$ respectively, so joint Bell State Measurement in the middle station establish a quantum entanglement link between $|M_1\rangle$ and $|M_2\rangle$. The critical and crucial condition here is that photons $|A'\rangle$ and $|B'\rangle$ must be indistinguishable, which adds experimental complexity to the scheme.

In summary, quantum entanglement swapping is a process where entanglement is transferred between particles that have not directly interacted. This enables the creation of new entangled pairs and facilitates the development of robust distance quantum communication systems.

1.8 Remote Entanglement protocols

Entanglement links play a crucial role in remote entanglement distribution, which is essential for various applications [74]. However, losses in quantum communication lines limit the range of the entanglement links, posing a significant challenge [84]. Quantum repeaters are used to address this issue. Quantum repeaters extend the range of entanglement links by creating entanglement between intermediate nodes, effectively maintaining the integrity of the quantum states over longer distances. These repeaters are also based on the idea of remote entanglement distribution, ensuring that quantum information can be transmitted reliably across vast distances, thus enabling the development of large-scale quantum networks. Quantum entanglement, by its nature, is generated locally through physical interactions between quantum systems, meaning one should locally entangle quantum particles and then use one to deliver the entanglement to another communicating party. The particle kept can be called a quantum memory, and the particle delivered a flying qubit. The most natural candidate for the flying qubit role is a photon, which can be transferred via low-loss optical fibers. Moreover, as it is clear now, the most fundamental building block for remote quantum communication is the ability to create a photon entangled with a memory qubit. Different possible protocol topologies define the photon path and include a high-level quantum diagram describing the Entanglement distribution [18]. Three possible schemes for implementing these entanglement links are considered: detection-in-midpoint, sender-receiver, and source-in-midpoint protocols [69].

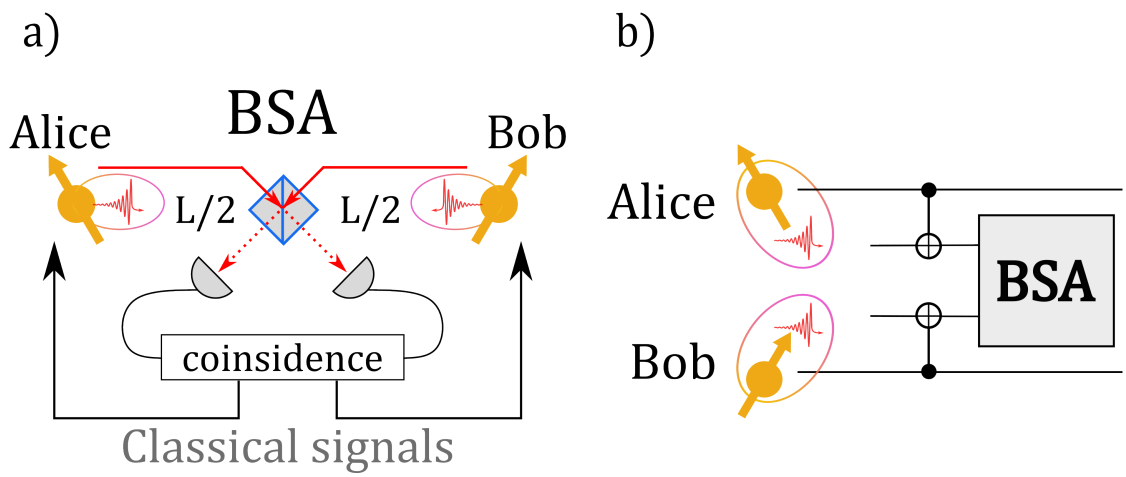

FIGURE 1.5: Detection-in-Midpoint scheme a) Hardware arrangement. Repeaters are separated by the distance L and the photons interact in the midpoint. Successful Bell State Measurement reported to communicating parties via classical channel. b) Quantum Circuit of the Detection-in-Midpoint scheme (equivalent to the one shown in Fig. 1.4)

In the **detection-in-midpoint scheme**, both senders create memory-photon entanglements at the end nodes, and the entangled photons are sent to the receiver, which is located in the midpoint [122][42][45]. The receiver has a Bell state analyzer (BSA) that performs the measurement and communicates the success or failure of the entanglement attempt via the classical channel[134]. Senders could have N memory qubits[150] so that the repeaters at the end nodes can generate photons at regular intervals synchronized to τ_{clock}. With this, the time for one round of communication takes the time τ_{round}:

$$\tau_{round} = \tau_{link} + N\tau_{clock} \tag{1.23}$$

where τ_{link} is a delay time related to the confirmation signal traveling. The probability of successfully entangling two memory qubits can be defined as p:

$$p = p_{BSA}(p_{optical})^2 \tag{1.24}$$

Where p_{BSA} is a probability of successful BSA outcome given that two photons arrived at the receiver station and $p_{optical}$ is the probability of successful photon transmission to the receiver point (coupling efficiency to the transmission line and transmission through the optical fiber over a distance of $L/2$ to the BSA point). With this, the average rate of entanglement distribution can be estimated as follows:

$$R = \frac{Np}{\tau_{round}} \tag{1.25}$$

The detection-in-midpoint protocol allows for relatively easy distributed decision-making but uses memory qubits inefficiently. Each qubit is locked for at least τ_{link} while waiting for a signal from the BSA, with a success probability of p for each transmission attempt. This topology only requires photon emission from spins, beam-splitter interference of photons, and single-photon detections at the central station.

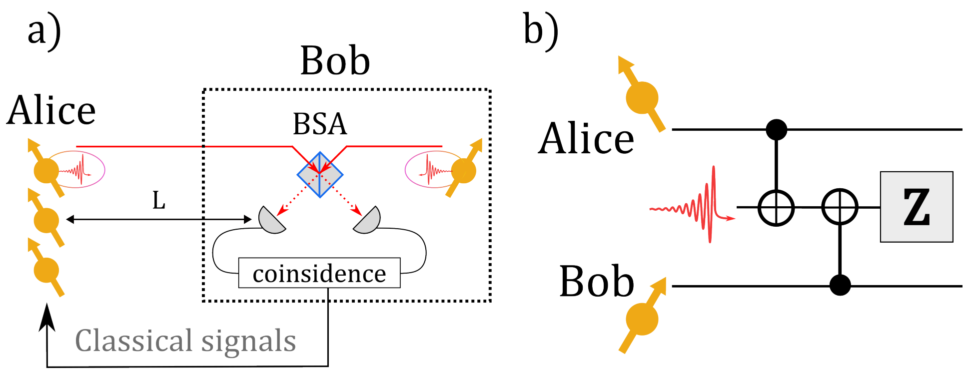

FIGURE 1.6: Sender-Receiver scheme a) Hardware arrangement. Repeaters are separated by the distance L, but the photons interact at the point of Bob's repeater, which allows him to make fast decisions about memory reset procedure. Successful Bell state measurement reported to Alice via classical channel. b) Possible Quantum Circuit of the Sender-Receiver scheme, when the one photons getting entangled with two communicating parties consequently.

High-fidelity entanglement can be achieved without needing efficient spin-photon interfaces like optical cavities. Additionally, the time overhead for classical communication is reduced by half, as endpoints communicate solely with the detection point, eliminating the need for direct communication between them.

The sender-receiver protocol involves direct entanglement distribution from the sender to the receiver [92]. This protocol is a possible modification of the previous one when the scheme is asymmetric. In this scheme, Bob has a shorter distance to the BSA so that his memory qubits are locked up for a shorter duration, allowing the potential use of fewer memory qubits. The example where BSA has been entirely moved into a repeater node of Bob is considered Figure 1.6 a. This setup allows Bob to make near-instantaneous decisions about his memory qubits, reducing the entanglement distribution time compared to the detection-in-midpoint protocol. It is worth mentioning that in this scheme, every node acts as a receiver on the "left" link and as a sender on its "right" link. So, Bob receives entangled photons from the "left" (from Alice) and tries to entangle this photon with his memory qubit by entanglement swap operation. Knowing almost instantly when entanglement is established changes the repeater's operation. With Alice having many memory qubits (N_A) and Bob having fewer ($N_B < N_A$), Bob can sequentially process each incoming photon with the same memory qubit by resetting it after a failed attempt, allowing him to use fewer qubits than Alice. The round time is defined by the time during which Alice's memory qubits are locked:

$$\tau'_{round} = 2\tau_{link} + N_A\tau_{clock} \tag{1.26}$$

This formula is given in the approximation $\tau_{clock} \ll \tau_{link}$, where τ_{clock} is the longest of two times - detector recovery and memory reset time. Moreover, to fairly compare the rate with the detection-in-midpoint protocol, the total number of memory qubits on Alice and Bob's side will be introduced as a fixed number $2N = N_A + N_B$; with this, the rate could be estimated:

$$R' < \frac{pN_A}{2\tau_{link} + N_A\tau_{clock}} < \frac{pN}{\tau_{link} + N\tau_{clock}} = R \tag{1.27}$$

Although the sender-receiver protocol has a lower average rate than detection-in-midpoint (although it can be shown that the rates are almost similar if$N_B \approx pN_A$), it offers several practical advantages. The main one is that sender-receiver topology does not require an intermediary station for memories to become entangled; however, the classical communication time for the heralding signal is twice as long compared to detection-in-midpoint, as it needs to travel the whole distance instead of half.

Lastly, **the source-in-midpoint protocol** places the entanglement source at

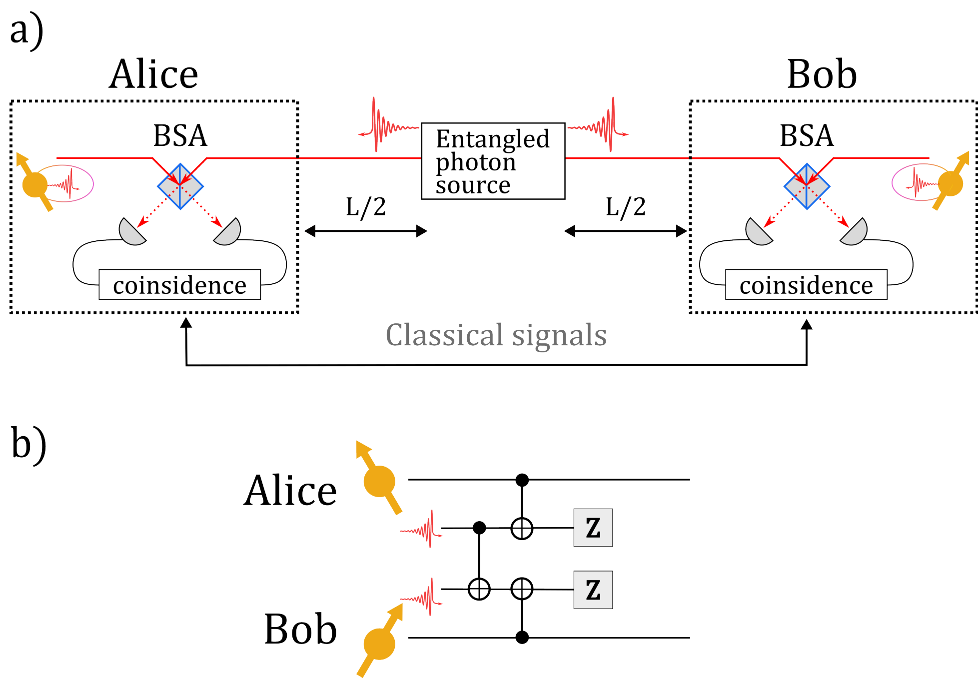

FIGURE 1.7: Source-in-midpoint a) Hardware arrangement. Repeaters are separated by the distance L. The entangled photon source is located in the middle and distributes the entangled pairs. Communicating parties do Bell state measurements on their sides and report each other's successful measurements. b) Quantum circuit of the source-in-midpoint scheme - entangled photons getting entangled with quantum memories.

the midpoint between the sender and receiver [68]. For each of the arriving entangled photons, both parties are performing BSA, allowing them to reset their memory quickly in case of entanglement failure Figure 1.7. The successful link establishment is reported to each other. Both previously mentioned protocols are ultimately limited by memory lock-up delays at the sender interface, so in the third one, both communicating parties are receivers. The round duration in this scheme is given by:

$$\tau'' = \tau_{link} + K\tau_{clock} \tag{1.28}$$

where K is the number of communication bins (communication transmissions). After K time bins, the protocol waits for τ_{link} to confirm entanglement, which occurs if both receivers entangled photons in the same bin, corresponding to photons from the same entangled pair. It can be shown that the rate could be expressed as:

$$\frac{R''}{R} \approx \frac{1}{2p_{optical}} \tag{1.29}$$

R'' scales with $p_{optical}$, when R and R' with $(p_{optical})^2$. Source-in-midpoint is more complex than detection-in-midpoint and sender-receiver due to its need for additional optical hardware, including two BSAs, more single-photon detectors, and an entangled photon source.

Despite this complexity, source-in-midpoint uses memory qubits more efficiently, potentially reducing the number needed compared to the other protocols. The source-in-midpoint protocol is less sensitive to the signal losses represented by $p_{optical}$, making it particularly well-suited for early prototypes of quantum repeaters. Each of these schemes offers different advantages and can be selected based on the specific requirements of the quantum communication network.

Chapter 2

The NV-center as a platform for Entanglement generation

This chapter focuses on the Nitrogen-Vacancy (NV) center in diamond, the defect used for the experimental realization of the spin-photon entanglement in this thesis. It overviews the NV center's properties, including its energy level scheme and the charge states. The discussion covers the ground state ${}^3A_2$ and excited state ${}^3E$ configurations, along with the level structure of the NV^0 charge state. Additionally, the chapter explores the methods for optical manipulation of the NV center, detailing processes such as initialization and readout. These aspects are critical for understanding the NV in achieving and controlling spin-photon entanglement.

2.1 The NV^- center in diamond

The crystal lattice of a diamond is made up of carbon atoms and forms a large band gap of $\approx 5.5eV$. The Nitrogen-Vacancy center (NV-center) is a point defect with a C_{3V} symmetry inside a diamond lattice [81]. It consists of a Nitrogen atom (that replaces a carbon atom) and a vacancy in the adjacent position (see Figure 2.2 a), the $N - V$ line defines a quantization axis [36]. The NV-center can be found in a neutral charge state NV^0 (it is formed by five electrons - three from carbons and two from nitrogen) or negative state NV^- (six electrons) [87] when an additional electron comes from the surrounding environment (see Figure 2.2 b). In this work, the NV-center is mainly considered as the NV^- state if the opposite is not mentioned. Many optical properties of the defect can be derived from the group theory, by combining available atomic orbitals [87] [28].

The six electrons form an energy level structure within the band gap, allowing optical transitions between ground and the excited triplets at a wavelength of $\approx 637nm$ [32] (see Figure 2.1). The combination of the six electrons has a common spin of 1 and the different sublevels of the ground and the excited states have given spin projections.

Under the excitation (resonant or not), the NV-center emits single photons from the transitions between ${}^3E \rightarrow {}^3A_2$ levels [151]. Because of a relatively low Debye-Waller factor of 3%, the majority of the NV - center fluorescence is associated with phonon sidebands (PSB) ranging from 600nm to 800nm [86] [48]. Another decay channel is associated with an inter-system crossing (ISC) [36] [113] from the excited state to the metastable singlet states ${}^1A - {}^1E$, from which the NV-center decays to the ground triplet. This process is non-coherent and spin-mixing.

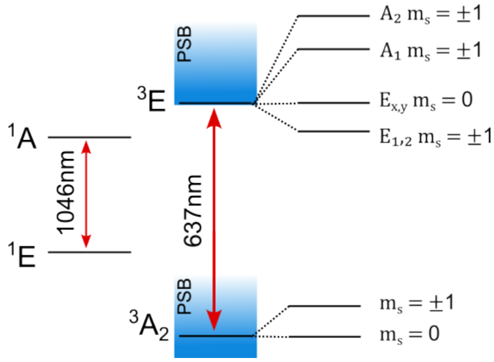

FIGURE 2.1: Level Structure of the NV^- center. The ground state triplet $^3A_2$ is separated from the excited state ^3E by $\approx 637nm$. The singlet states ^1A and ^3E are often called metastable state. They are responsible for inter-system crossing decay.

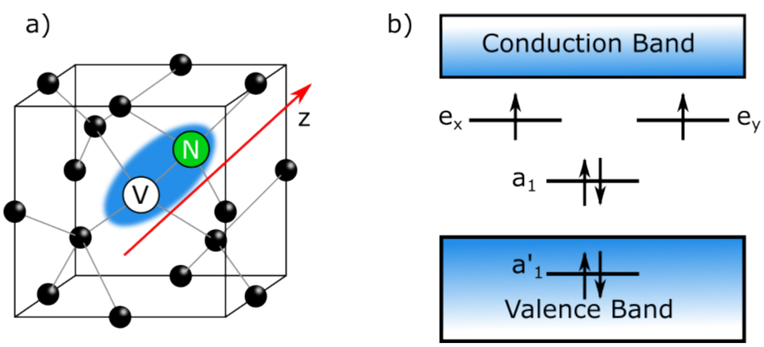

FIGURE 2.2: NV structure a) The NV center in the crystall latice of the diamond, the $N-V$ axis defines the quantazation axis. b) Scheme of the NV center free orbitals filling with electrons

2.1.1 Ground State $^3A_2$ of the NV center

The full system (NV) Hamiltonian The NV center always has an intrinsic Nitrogen spin (^{14}N in this work), coupled to the electron spin of the NV center via a hyperfine interaction. The full system Hamiltonian can be represented as a sum of the electron spin Hamiltonian and the Hamiltonian associated with the intrinsic ^{14}Nitrogen spin.

Electron spin Hamiltonian The NV-center's electron ground state consists of three spin sub-levels ($|m_s = 0, \pm 1\rangle$) [66]. When no magnetic field is present, the $|m_s = \pm 1\rangle$ sub-levels have the same energy (degenerate) and separated from the $|m_s = 0\rangle$ sub-level by a distance of around $2.87GHz$, which happens due to the spin-spin interaction and known as the Zero-Field splitting (ZFS). Application of an external magnetic field can eliminate the degeneracy of the $|m_s = \pm 1\rangle$ sub-levels through the Zeeman effect. The effective electron spin Hamiltonian is given by [83]

$$H_{el}^{GS} = DS_z^2 + E(S_x^2 - S_y^2) + \gamma_e \mathbf{B} \cdot \mathbf{S} \tag{2.1}$$

where $\mathbf{S}$ is a vector of the spin matrices for spin 1, $\gamma_e = 2.8$ MHz/G is a gyromagnetic ratio, $D = 2.87$GHz is the Zero Field Splitting [115] and E is an off-axis parameter influenced mainly from local strain. The measurement of the E parameter can be used as a principle of NV - based temperature [107] [132] or the electric field [37] sensors.

$$S_x = \frac{1}{\sqrt{2}} \begin{pmatrix} 0 & 1 & 0 \\ 1 & 0 & 1 \\ 0 & 1 & 0 \end{pmatrix} S_y = \frac{1}{i\sqrt{2}} \begin{pmatrix} 0 & 1 & 0 \\ -1 & 0 & 1 \\ 0 & -1 & 0 \end{pmatrix} S_z = \frac{1}{\sqrt{2}} \begin{pmatrix} 1 & 0 & 0 \\ 0 & 0 & 0 \\ 0 & 0 & -1 \end{pmatrix}$$

In case of a weak magnetic field misalignment ($B_z >> B_\perp$), the $NV - center$ transitions can be calculated by the following formula

$$f_{\pm 1} = D \pm \sqrt{E^2 + (\gamma_e B_z)^2} \tag{2.2}$$

Intrinsic ^{14}Nitrogen spin The NV center is always associated with an intrinsic nuclear spin of the Nitrogen [56] (in this work only ^{14}N is considered), which can serve as a quantum memory. The ^{14}N has a spin equal to 1 and leads to a hyperfine interaction, which is given by the following Hamiltonian:

$$H_{hf} = QI_z^2 + \gamma_N \mathbf{B} \cdot \mathbf{I} + \mathbf{S} \cdot \mathbf{A} \cdot \mathbf{I} \tag{2.3}$$

where $Q = -4.96$ MHz [36][56][121] is a quadruple splitting parameter, $\gamma_N = 0.3$ kHz/G is gyromagnetic ratio and $\mathbf{A}$ is hyperfine tensor. In case of ^{14}N the last part could be expressed as

$$\mathbf{S} \cdot \mathbf{A} \cdot \mathbf{I} = A_\parallel S_z I_z + \frac{A_\perp}{2}(S_+ I_- + S_- I_+) \tag{2.4}$$

where $A_\parallel = -2.19$ MHz and $A_\perp = -2.7$ MHz [56] are parallel and perpendicular components of the hyperfine interaction. Because of this, energy scheme for two electron sublevels ($|m_s = 0, -1\rangle$) looks as shown in the Figure 2.3.

The allowed transitions are marked with arrows - red for electron transitions (MW) and violet for nuclear transitions (RF). It can be seen, that nuclear transitions are possible on three frequencies: $Q, Q + A_\parallel, Q - A_\parallel$ (Zeeman shift is neglected).

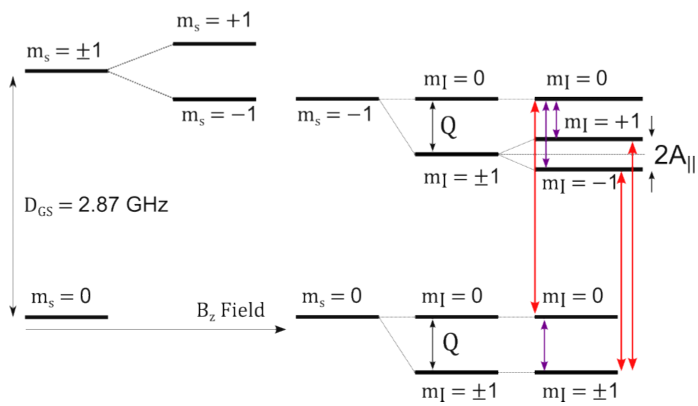

FIGURE 2.3: Ground state levels, influence of magnetic field, quadruple splitting and hyperfine interaction (shown only for states $|0, -1\rangle$). Red lines show allowed MW transitions, that change electron spin projection m_s, violet lines represent RF transitions between ^{14}N sublevels (with different spin projections m_I.

2.1.2 Excited State ^3E of the NV center

At low temperatures, the reduction in phonon mixing within the excited state enables a clearer resolution of all the levels and transitions. The NV center's excited state comprises six levels (two triplets) [8], and their positions are significantly influenced by the local electric field, formed by the charge bath and a strain. The impact of the strain can be analyzed in terms of its parallel and perpendicular components (projection to the main quantization axis). The parallel strain uniformly shifts all levels, whereas the relationship with perpendicular strain is more complex, as illustrated in a Figure 2.4

Transitions from the ground states to the excited states exhibit spin selectivity and spin conservation, allowing to see all resonant lines, corresponding to different transitions and particularly, allowing access to the E_y and E_x levels solely through resonant excitation from the ground state sublevel with $|m_s = 0\rangle$ spin projection [71].

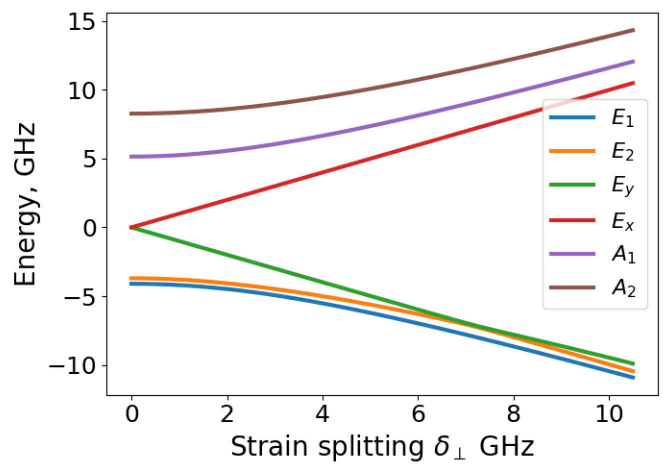

FIGURE 2.4: Excited state levels dependence under different values of the perpendicular strain $\delta_\perp$

The distance between the E_y and E_x levels is precisely twice the transverse strain. In subsequent applications, specifically, the E_y level will be exclusively employed for reading out the state of the NV center, as well as for the creation of the spin-photon entanglement. The two orthogonal transition dipoles associated with these transitions lead to a pronounced linear polarization of the emitted photons and of course, the excitation efficiency is influenced by the polarization of the excitation laser (it will be important in cross-polarization part, see 4.1.2).

Other levels are linked to the spin sub-levels $|m_s = \pm 1\rangle$ of the ground state and can be used to initialize the NV center to a state with a spin projection of $|m_s = 0\rangle$. In the experiment, the $E_{1,2}$ levels were specifically used for this purpose. The Photo Luminescence Emission (PLE) spectrum of the NV center used in this work was measured and typical value of perpendicular strain was in a range of a few GHz.

As was said before, the positions of all the levels in the ${}^3E$ excited state are strain-dependent and can be described as a sum of the unperturbed H_{el}^{ES} and interaction

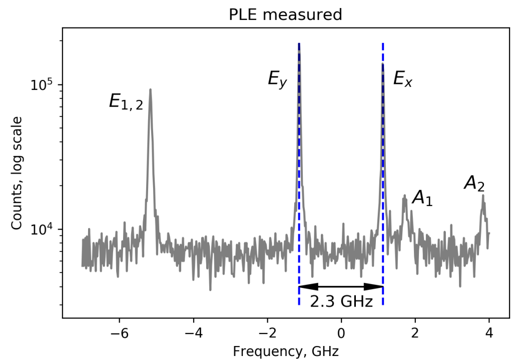

FIGURE 2.5: Low temperature PLE spectrum of the NV center, the distance between E_x and E_y is equal to $2\delta_\perp$

V_{el}^{ES} Hamiltonians [36] :

$$H_{el}^{ES} = D_{ES}^{\parallel} S_z^2 - \lambda_{ES}^{\parallel}\sigma_y \otimes S_z + D_{ES}^{\perp}[\sigma_z \otimes (S_y^2 - S_x^2) - \sigma_x \otimes (S_y S_x + S_x S_y)] + \\ + \lambda_{ES}^{\perp}[\sigma_z \otimes (S_x S_z + S_z S_x) - \sigma_x (S_y S_z + S_z S_y)] \quad (2.5)$$

where $\sigma_{x,y,z}$ are Pauli matrices related to orbital coupling and $S_{x,y,z}$ are spin 1 operators, $D_{ES}^{\parallel} = 1.42$ GHz [95], $D_{ES}^{\perp} = 0.775$ GHz ,$\lambda_{ES}^{\parallel} = 5.3$ GHz, $\lambda_{ES}^{\perp} = \frac{0.2}{\sqrt{2}}$ GHz [8]. This Hamiltonian has two degenerate levels, related to spin projection $|m_s = 0\rangle$, which can be removed by the strain factor in interaction Hamiltonian:

$V_{el}^{ES} = d_{ES}^{\parallel}(E_z + \delta_z) + d_{ES}^{\perp}(E_x + \delta_x)\sigma_z - d_{ES}^{\perp}(E_y + \delta_y)\sigma_x + \mu_B(l_{ES}^{\parallel}\sigma_y + g_{ES}^{\parallel}S_z)B_z + \mu_B g_{ES}^{\perp}(S_x B_x + S_y B_y)$ where $d_{ES}^{\parallel}, d_{ES}^{\perp}$ are the components of the ^3E electron dipole moment, $l_{ES}^{\parallel}$ is ^3E orbital magnetic moment [114], $g_{ES}^{\parallel}, g_{ES}^{\perp}$ are components of ^3E electronic g-factor tensor.

It can be noticed, that the electric field and strain are included in Hamiltonian as one term - which means, that level positions can be tuned via Stark effect [125].

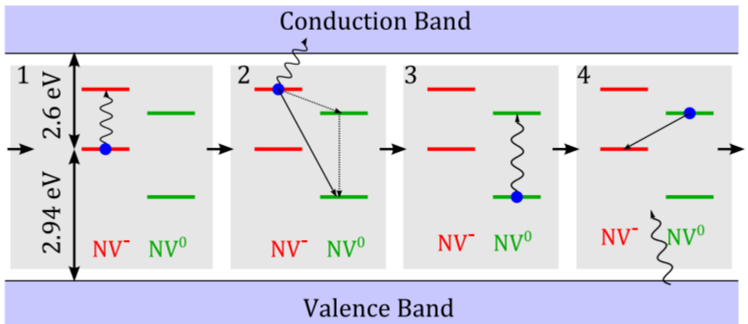

FIGURE 2.6: NV^- center Ionization - Recombination scheme. 1) first photon excites the NV^-. 2) Second photon excites the electron to the conduction band, creating NV^0 state. 3) First photon excites the NV^0 center. 4) An electron from the valence band is excited, thus creating NV^- state. Taken from [2]

It might be useful if two or more NV centers should be entangled, so they all must emit ZPL photons of the same frequency (to have them indistinguishable). Local electric field fluctuations also cause spectral diffusion effect.

2.1.3 NV^0 level structure

The NV^- center has two unbounded electrons and one of them can be ionized, putting the NV^- center into another charge state called NV^0 [50]. For most of the experiments in this work, the NV^0 state is undesired and below the ionization and recombination mechanisms are discussed.

Well known, that at the wavelengths of the experiment, the ionization is two photon process [123]. First photon excites the electron from the ground state and the second photon brings the electron to the conduction band, leading to the NV^- ionization (see Figure 2.6). This process is getting more pronounced under resonant

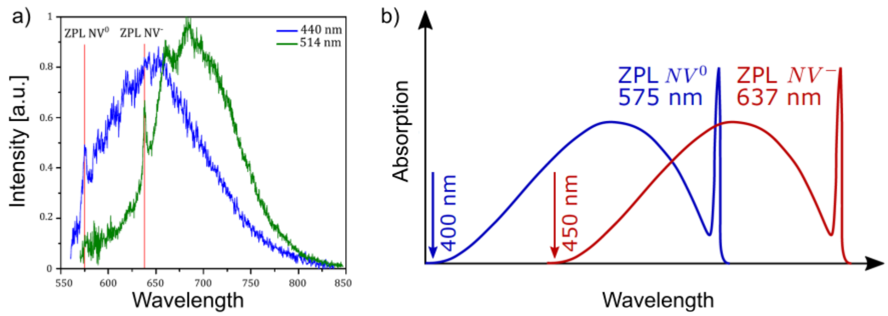

FIGURE 2.7: a) The NV spectra emission under 440nm excitation (blue, yielding NV^0 spectra) and under 514nm (green, yielding NV^-). Taken from [2]. b) Illustration of absorption spectra of the NV^0 (blue) and NV^- (red). Adapted from [9]

excitation (because the first-photon excitation becomes a lot more probable). Recombination of the NV^0 center back to the NV^- charge state is also a two photon process - first photon excites the electron and the second photon brings an electron from valence band to the ground state level of the NV^- center (see Figure 2.6).

The absorption spectra of both charge states are given in a Figure 2.7 b [9]. Because of this, the steady state populations ratio of the NV^-, NV^0 charge states under continuous laser illumination depends on laser wavelength - for example it is 70/30% for 532nm laser and 10/90 % for 594nm. Moreover, the pronounced Zero-photon lines can clearly be seen at 575nm and 637nm, that are also presented on emission spectra (see Figure 2.7 a) [2]. Due to the fact that the emission spectra are separated, by selecting suitable filters, it is possible to regulate the contribution of the different charge states to the detected signal and moreover to detect quantum jumps from one charge state to another (see Figure 2.8). Under a detuned from resonance 575nm illumination, the NV center jumps from the negatively charged NV^- state (bright in the used confocal setup) to neutrally charged NV^0 state in

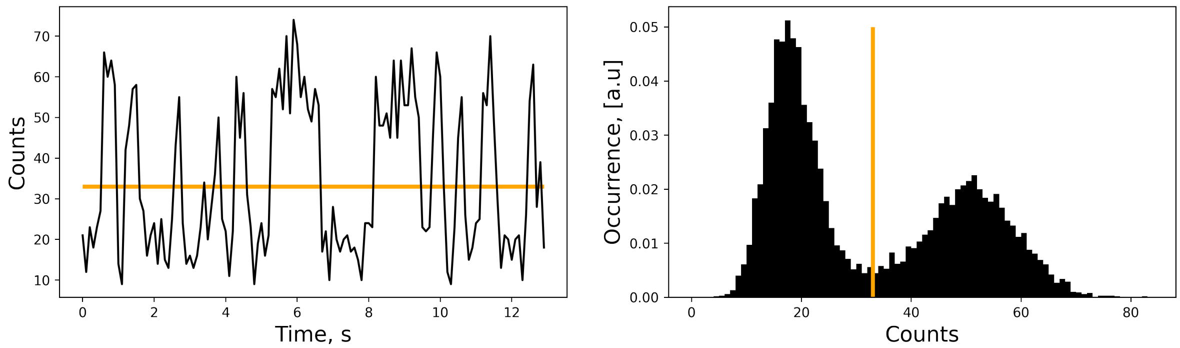

FIGURE 2.8: a) Time trace of the single NV fluorescence - the behaviour is reflecting quantum jumps between the bright NV^- and the dark NV^0 states. Yellow line is the threshold. b) Histograms of detected photons within detection window. Two distributions, corresponding to NV^0 and NV^- states, can clearly be seen, yellow line shows the threshold.

a time-scales of seconds (see Figure 2.8 a). Using this timetrace, the counts distribution can be ploted and the threshold between two charge states can be clearly defined. This allows to distinguish two different charge states (see Figure 2.8 b). Of course, this dynamics is laser's power and wavelength dependent, thus under 575nm excitation (resonant to NV^0 state), the distribution, corresponding to NV^0 state vanishes (because recombination rate becomes way higher, than ionization one). In general, bringing NV^0 back to the desired NV^- state requires strong laser pulse, which could cause additional spectral diffusion. From this point of view, the use of a laser resonant with a NV^0 transition looks very logical, since in this case the required energy is much less.

Detailed experimental research of the NV^0 levels and transitions were done in a recent study [5]. In this thesis the PLE of NV^0 was also measured, when the 575nm laser frequency was scanned, accompanied with a signal detection in phonon-side

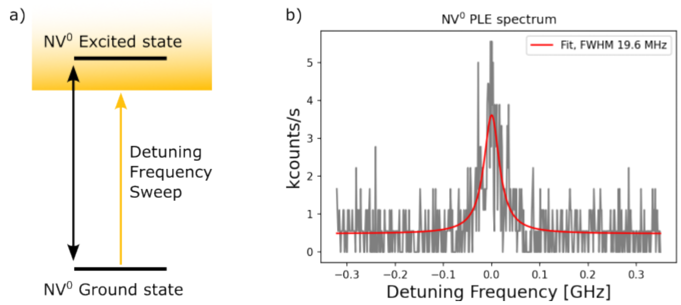

FIGURE 2.9: NV^0 Photo Luminescence Emission (PLE) of the NV^0 charge state a) Scheme of the experiment, laser frequency scan and photons detection at the same time. b) Measured PLE signal from the NV center in the neutral charge state NV^0.

bands (see Figure 2.9).

2.2 NV-center optical manipulation

2.2.1 NV-center initialization

Any measurement protocol has to start with preparation of the NV center in a well-defined state [35]. In the case of the NV center, it is necessary to ensure the correct charge state and then the initialization of the electron spin. The first can be achieved by applying a repump laser and a procedure for checking the charge state (simultaneous activation of two lasers, resonant to different spin projections, with parallel counting of the number of photons) [105] [16]. To initialize the electron spin, the intersystem crossing with the metastable state can be used. For instance, under application of the laser at frequency of $E_{1,2}$ transition (spin selective to $|m_s = \pm 1\rangle$ spin projection) the electron of the NV center does few transitions between ground $^3A_2$ and excited ^3E states, and at some point get decayed to the metastable ^1A

singlet, from which it decays to the ground $^3A_2$ state (trough ^1E state). It can decay to any of the different spin-projection sublevels, but if it decays to the state $|m_s = \pm1\rangle$, then the process gets repeated, whereas for the $|m_s = 0\rangle$ state the laser excitation is not resonant anymore - this way the population accumulates in $|m_s = 0\rangle$ state. Similar reasoning can be applied for initialization to the $|m_s = \pm1\rangle$ state, but then the laser radiation must be resonant with the E_x or E_y transitions (both have spin projection $|m_s = 0\rangle$). In the experiment, when resonant laser pulses are continuously applied, with the parallel registration of the photon arriving time, it can be seen, that after some time photons are not coming anymore, indicating that the laser is not resonant anymore (the NV center is in the non-resonant ground state sublevel). The behavior of the fluorescence time-trace could be approximated with decaying exponent, which is faster for $|m_s = \pm1\rangle$ due to the stronger coupling of these sublevels to the metastable state. Out of this graphs initialisation fidelity can be estimated to reach impressive values of 99% [112]. The exponents rates are power dependent, showing saturation behavior, but it should be noted, that at high laser powers the laser excitation may not remain selective, because of power broadening (It is especially important to pay attention to this when choosing a polarization of the excitation laser in a cross-polarization scheme). In certain experiments, collection purity was improved by sacrificing pump efficiency, which required increasing the excitation laser power.

2.2.2 NV-center readout

The main advantage of reading out the $|m_s = 0\rangle$ ground state of the NV center and not the $|m_s = \pm1\rangle$ is different couplings to the metastable state, thus the electron will do more excitation-photon emission events before decaying to off-resonant state through ISC - in other words the $|m_s = 0\rangle$ state is brighter [146][31][49].

To read out the state of the NV center, the E_y transition was chosen and not E_x, because the $A_1(m_s = \pm 1)$ transition is relatively close to the E_x and can also be excited due to power broadening effect, thus destroying spin-selectivity of the readout procedure (please keep in mind, that the statement can be invalid for different strain and magnetic field configurations). Because of the relatively low collection efficiency the emitted photons can be lost. However state readout fidelity can be increased, when claiming the $|m_s = 0\rangle$ if more than defined threshold amount of photons are detected. By increasing the threshold, the state readout fidelity also increases, but unfortunately at the same time the rate reduces. To estimate the fidelity the following simple measurement can be done - first the NV center is prepared in different initial states and then the state is simply read out, while measuring amount of the detected photons. Then two "number of counts" histograms [112] can be plotted; they correspond to two different initial states and the the threshold should be chosen. The infidelity $(1 - F)$ could be estimated as

$$1 - F = \frac{\sum_{n=thr}^{\infty} y_1}{\sum_{n=thr}^{\infty} y_0} \tag{2.6}$$

where y_0 and y_1 are the histogram counts, corresponding to the initial states $m_s = 0$ and $m_s = 1$ respectively.

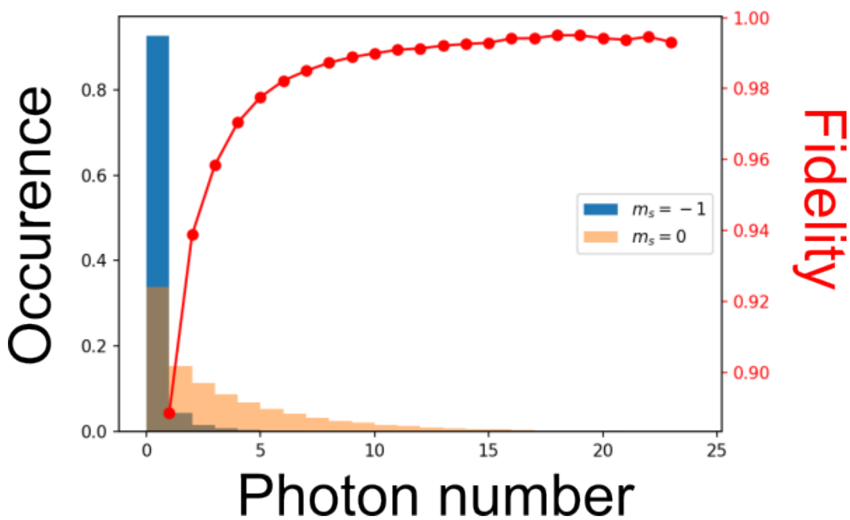

FIGURE 2.10: Number of detected photons histogram, when the NV center is initialized to the state $|m_s = 0\rangle$ (orange) and $|m_s = -1\rangle$ blue. The red curve shows the fidelity for different threshold levels

Chapter 3

Basic Spin Manipulation techniques

Precise control over the electron states of the NV center is essential to generate spin-photon entanglement. The chapter describes the fundamental techniques and mentions the technical details of their implementation. By detailing these basic techniques, the chapter provides an understanding of the NV center's spin state dynamics and procedures required to implement and utilize spin-photon entanglement.

3.1 Optically Detected Magnetic Resonance (ODMR)

The important advantage of the NV center is the possibility to measure its electron spin state using optical excitation [54]. It works even at non-resonant excitation because excited state levels with $|m_s = 0\rangle$ projection have weaker coupling to the long-lived metastable state, compared to the $|m_s = \pm 1\rangle$ states. Thus, if the NV center is in the $|m_s = \pm 1\rangle$ state, it emits on average fewer photons, being under laser excitation, because it "spends" more time in the non-radiative metastable state [135]. The fluorescence difference between the bright state $|m_s = 0\rangle$ and dark state $|m_s = \pm 1\rangle$ is called contrast and can reach 30% [40]. *Because of the spin-selectivity of the resonant transitions at low temperature, the contrast between different spin projections can theoretically reach* 100%.

To find the resonance frequencies between the ground state levels $|m_s = 0 \leftrightarrow \pm 1\rangle$, one can do the following experiment: initialize NV center to the $|m_s = 0\rangle$ ground state and then apply MW π-pulses at different frequencies with a following readout [40]. Once the frequency of the MW matches the transition frequency, the electron state of the NV center will be flipped from the bright state to the dark state, and the consecutive readout will show a dip in the number of detected photons (Figure 3.1).

If a magnetic field is introduced, the energy levels $|m_s = \pm 1\rangle$ shift with respect to the $|m_s = 0\rangle$ state because of the Zeeman-splitting. As a results, also ODMR transition splits into two peaks for the $|m_s = 0 \leftrightarrow -1\rangle$ and $|m_s = 0 \leftrightarrow +1\rangle$ transitions. Both peaks are centered around the ZeroField Splitting (ZFS) ($D_{GS} \approx 2.87$ GHz) and must consist of 3 dips, that correspond to 3 possible hyperfine ^{14}N states [151]. The distance between nuclear dips must be equal $A_{\parallel}$, which is ≈ 2.19 MHz. Because of the dependency of the ODMR resonance frequency on the external magnetic field, ODMR is a useful technique to measure DC magnetic fields.

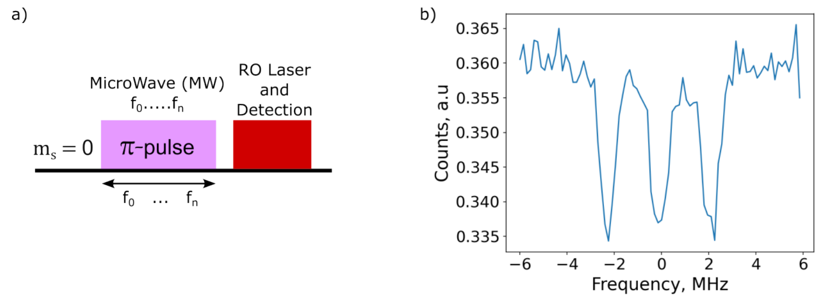

FIGURE 3.1: ODMR a) Scheme of the experiment, a $\pi - pulse$ is applied to the initialized NV center at different frequencies, followed by a readout b) Obtained ODMR spectrum, the three dips correspond to resonances with three different ^{14}N hyperfine sublevels

3.2 Rabi Oscillations

To understand the dynamics of $NV center$ under a coherent MW drive (e.g. during an ODMR measurement), one should consider its Hamiltonian under external perturbation V_{MW}:

$$V_{MW} = \gamma_e B_x S_x cos(2\pi\nu t) \tag{3.1}$$

where γ_e is electron g-factor (2.8 MHz/G), B_x is magnetic field amplitude of the MW drive, S_x is spin matrix and ν is the driving frequency.

The total Hamiltonian $H_0 + V_{MW}$ will be given by:

$$H = H_{el}^{GS} + V_{MW} = DS_z^2 + \gamma_e B_z S_z + \gamma_e B_x S_x cos(2\pi\nu t) \tag{3.2}$$

In matrix form, it will be given by:

$$H = \begin{pmatrix} D + \gamma_e B_z & \frac{1}{2}\gamma_e B_x cos(2\pi\nu t) & 0 \\ \frac{1}{2}\gamma_e B_x cos(2\pi\nu t) & 0 & \frac{1}{2}\gamma_e B_x cos(2\pi\nu t) \\ 0 & \frac{1}{2}\gamma_e B_x cos(2\pi\nu t) & D - \gamma_e B_z \end{pmatrix} \tag{3.3}$$

To focus on the dynamics of the spin system introduced by the MW drive, the total Hamiltonian H can be transformed into the interaction picture under the rule: $\tilde{H} = UHU^{\dagger} + i\hbar(\frac{\mathrm{d}}{\mathrm{dt}}U)U^{\dagger}$, where $U = \exp\{-i2\pi\nu t S_z\}$ is an evolution operator. Utilizing the Rotating Wave Approximation (RWA), the interaction picture Hamiltonian simplifies to:

$$\tilde{H} = \begin{pmatrix} \Delta_+ & \Omega_R & 0 \\ \Omega_R & 0 & \Omega_R \\ 0 & \Omega_R & \Delta_- \end{pmatrix} \tag{3.4}$$

where $\Omega_R = \frac{1}{2}\gamma_e B_x$ is Rabi frequency [109] [66], which reflects the strengths of the coherent drive, $\Delta_{\pm} = D \pm \gamma_e B_z - \nu$ are detunings from resonant transition frequencies $(m_s = |0\rangle \leftrightarrow |\pm 1\rangle$. Under a magnetic field, the transitions are getting well-separated compared to Ω_R, so one can treat the NV center Hamiltonian as a 2-level system. In this case, the probability amplitudes of a two-level system can be written as

$$c_0(t) = \left\{ c_0(0)\left[\cos\left(\frac{\Omega t}{2}\right) - \frac{i\Delta}{\Omega}\sin\left(\frac{\Omega t}{2}\right)\right] + c_1(0)\frac{i\Omega_R}{\Omega}\sin\left(\frac{\Omega t}{2}\right)e^{-i\phi}\right\} e^{i\Delta t/2}$$
$$c_1(t) = \left\{ c_1(0)\left[\cos\left(\frac{\Omega t}{2}\right) + \frac{i\Delta}{\Omega}\sin\left(\frac{\Omega t}{2}\right)\right] + c_0(0)\frac{i\Omega_R}{\Omega}\sin\left(\frac{\Omega t}{2}\right)e^{i\phi}\right\} e^{-i\Delta t/2}$$

where Δ is detuning and $\Omega = \sqrt{\Omega_R^2 + \Delta^2}$ is so-called general Rabi frequency. The probabilities of NV center to be in states $|0\rangle$ and $|1\rangle$ are given by $|c_0(t)|^2$ and $|c_1(t)|^2$ and under initial condition $c_0(0) = 1, c_1(0) = 0$, the population difference is given by:

$$W(t) = |c_0(t)|^2 - |c_1(t)|^2 = \left(\frac{\Delta^2 - \Omega_R^2}{\Omega^2}\right)\sin^2\left(\frac{\Omega t}{2}\right) + \cos^2\left(\frac{\Omega t}{2}\right) \tag{3.5}$$

The oscillations of the state population are called Rabi Oscillations. One can notice from the formula that the Rabi oscillations are getting faster in the case of detuning, but the contrast is reduced. It is easy to understand using Bloch Sphere representation - In the case of detuning, the oscillation is happening around the axis, with a z-projection proportional to the detuning Δ.

3.2.1 MW and RF Rabi oscillations

In Figure 3.2 a the experimental sequence to measure the Rabi oscillations between 2 ground sub-levels $|m_s = 0\rangle \leftrightarrow |m_s = -1\rangle$ is shown, measured under constant external magnetic field of ≈ 80 Gauss. The microwave frequency was resonant to the transition (≈ 2.66 GHz) and was applied through the $20\mu m$ wire, placed next to the NV center. Starting from the initialized state $|m_s = 0\rangle$ microwaves for time τ (sweeping parameter) were applied with the following state readout.

The resulting Rabi measured on the NV oscillations are shown in Figure 3.2 b. One can see the effect of detuning mentioned above.

The Rabi oscillations could also be measured between 2 hyperfine ^{14}N sublevels (for example $|m_s = 0, m_I = 0 \leftrightarrow m_s = 0, m_I = -1\rangle$), that are separated by ≈ 4.9 MHz. The experimental results are shown in Figure 3.3. One needs to apply higher power than electron-level drive to drive this transition because of the lower gyromagnetic ratio of nuclear spin(0.3kHz/G) compared to electron (2.8 MHz/G).

one should keep in mind that the setup (particularly wires in the cryostat) have a specific transmission response - so that the transmission is higher at low frequencies.

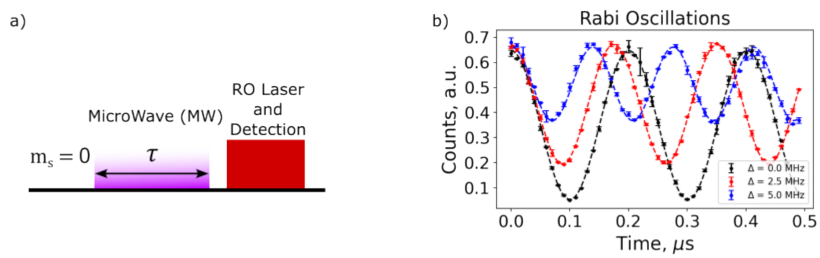

FIGURE 3.2: MW Rabi Oscillations a) Scheme of the experiment, an MW pulse of different duration is applied to the initialized *NV* center, followed by a readout. b) Obtained data - with detuning, the oscillation frequency increases, but the contrast decreases.

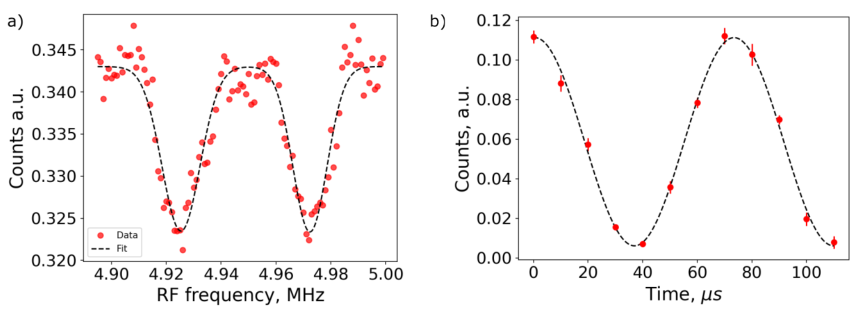

FIGURE 3.3: Nuclear measurements a) Nuclear ODMR - dips correspond to transitions between hyperfine levels with $|m_I = 0 \leftrightarrow \pm 1\rangle$ nuclear projections in the $|m_s = 0\rangle$ electron spin subspace b) RF driven Rabi oscillations between $|m_I = 0 \leftrightarrow -1\rangle$ hyperfine sub-levels of the $|m_S = 0\rangle$ subspace

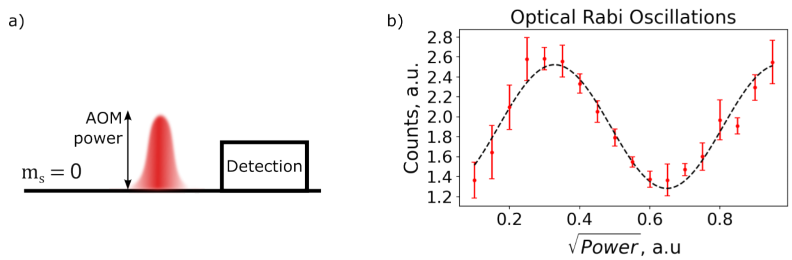

FIGURE 3.4: Optical Rabi a) In the Scheme of the experiment, a 2ns Gaussian shape pulse is applied to the initialized NV center, followed by a readout. The power of the pulse is swept via AOM. b) Obtained data - Rabi oscillations under laser pulse power sweep.

3.2.2 Optical Rabi oscillations

Rabi oscillations under coherent drive could also be implemented between ground and excited state levels, for example ($|m_s = 0\rangle$ of ground state and $|E_y\rangle$ of the excited state). In this case, the transition frequency corresponds to $637nm$ visible light, and the electrical dipole is driven using a resonant laser [16].

However, because of the short lifetime of the excited state ($\approx 12ns$ [67]), it is not possible to sweep the duration of the driving pulse. Instead tthe duration of the drive is kept constant, while the power of the laser excitation is varied. In this case a short Gaussian-shaped pulse of FWHM $= 2ns$ was applied through the EOM, and the AOM controlled the pulse power.

3.3 Quantum gates

In the experiment, both the NV center electronic spin and ^{14}N nuclear spin were considered as qubits, on which quantum gates [89] can be performed [126] [133]. For example, the application of a resonant MW or RF signal for the defined durations,

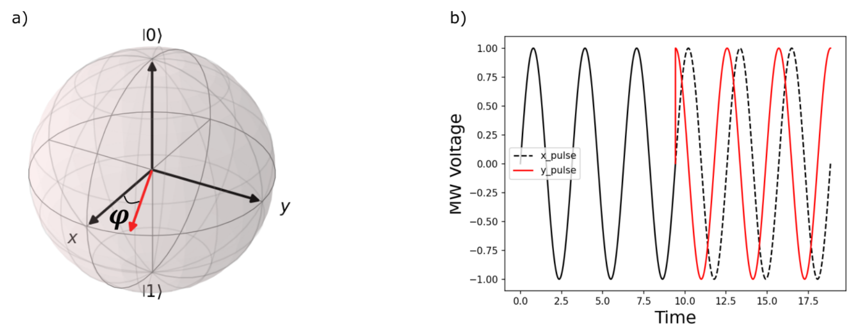

FIGURE 3.5: Rotation Pulse Phase. a) Bloch sphere, the red arrow shows the rotation axis, turned by angle ϕ from the x-axis. b) Signal in time, black curve is rotation around x axis and red curve around y

corresponding to a population swap, is called π - pulse, $\tau_\pi = \pi/\Omega_R$. Similarly, it is logical to call the pulse of the duration $\tau_\pi/2$ as $\pi/2$ - pulse and so on [39]. An important concept is the phase of the rotation pulse. If one imagines the Bloch Sphere, the sinusoidal, resonant MW (for example) pulse is driving the 2-level system of the NV center around an in-equatorial axis (for example, x - the first pulse defines the zero-phase and rotational axis). If one changes the phase of MW drive by ϕ, then the rotation will occur around an axis rotated from the original one by an angle ϕ (see Figure 3.5 a). This way the pulse could be called π_y if the phase was changed by $\pi/2$ or $\pi_{\pi/3}$ if the phase was changed by $\pi/3$.

One can also implement 2-qubit gates between the electron spin of the NV center and nuclear spin ^{14}N qubits [143][149][6]. For instance, ^{14}N spin exhibits varying transition frequencies depending on different projections of the electron spin. Consequently, selecting an RF frequency resonant for one transition renders it non-resonant for another. Therefore, when applying a π-pulse, a nuclear spin flip occurs only if the electron is in the specified state - which is called a CNOT gate. A comparable approach can be employed in a CNOT gate where the control qubit is the nuclear

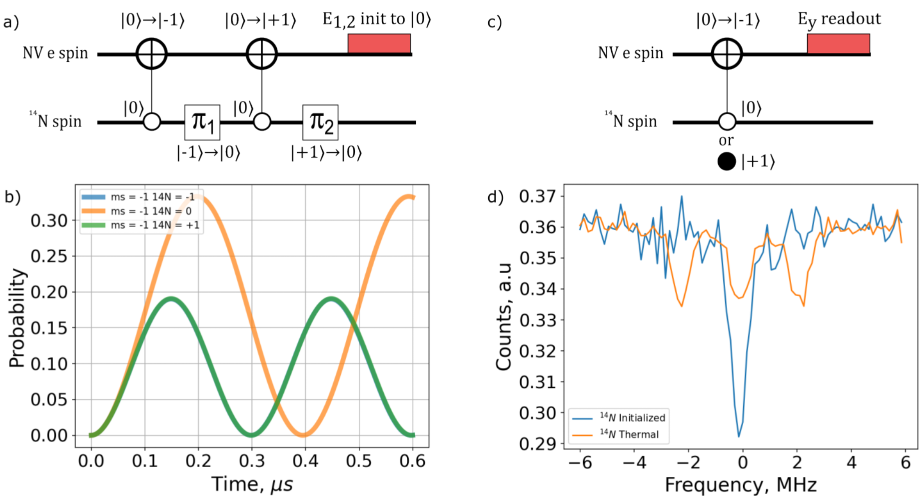

FIGURE 3.6: Quantum Gates. a) Quantum circuit to initialize ^{14}N spin ti state $|0\rangle$. b) A synchronized pulse approach is used to implement the CNOT gate. c) ^{14}N readout protocol - mapping to the electron spin with the following readout. d) ODMR picture, when ^{14}N is initialized (blue) and not initialized (orange)

spin. This method relies on the fact that the transition frequency of the electron spin qubit also varies with the projection of the nuclear spin (see Figure 3.1). Applying MW at the chosen frequency can execute a CNOT flip of the electron spin. It is crucial to utilize sufficiently low power of the MW drive to prevent undesired transitions caused by power broadening [117]. Another approach is to use so-called synchronized pulses [46] - when the duration and amplitude of the MW were chosen specifically in such a way that the desired spin projection does odd spin-flips and undesired projections do even amount of spin-flips (effectively coming to the initial state, see Figure 3.6 b).

With these basic quantum gates at disposal, it becomes feasible, for instance, to initialize and read the nuclear spin using the protocols depicted in the Figure 3.6.

The nuclear spin initialization and readout are the essential building blocks for all experiments with ^{14}N, including nuclear spin - photon entanglement [144].

Nuclear spin initialisation. To initialise ^{14}N the scheme shown on Figure 3.6 a is used.

- The protocol starts with NV electron - ^{14}N spins being in a state $|0, Thermal\rangle$.
- With the application of the CNOT gate (flip electron spin to $|m_s = -1\rangle$ if ^{14}N state is $|m_I = 0\rangle$), one 'stores' the $|m_I = 0\rangle$ projection of nuclear spin in the electron level space $|m_s = -1\rangle$.
- RF π - pulse flips the population from $|m_I = -1\rangle$ hyperfine sublevel to $|m_I = 0\rangle$.
- After this, the second CNOT gate stores again the $|m_I = 0\rangle$ projection, but now in $|m_s = +1\rangle$ electron state
- The second RF $\pi - pulse$ at frequency, corresponding to another hyperfine transition, flips the population from the $|m_I = +1\rangle$ hyperfine sublevel to $|m_I = 0\rangle$.
- After all the steps, a nuclear spin must be in state $|m_I = 0\rangle$, but the electron spin could be in any of three possible states. So the application of the $E_{1,2}$ laser will incoherently initialise electron spin to the $|m_S = 0\rangle$ state, while hardly influencing the nuclear spin - finally inititalizng the NV electron - ^{14}N system into the state $|0, 0\rangle$.

Nuclear readout. There is no direct optical access to the nuclear spin, so its readout could only be done via the electron spin of the NV center [96]. For this, both spins are getting entangled and the electron spin is measured (see Figure 3.6 c), for example via CNOT gate application - both CNOT on $|m_I = 0\rangle$ and $|m_I = +1\rangle$ are equivalent for this purpose.

3.4 Electron Spin Decoherence

As the NV center is located in a diamond crystal lattice, it is also influenced by it, which leads to decoherence, especially of the electron state. Phenomenologically, this could be explained as a decay to a "thermal" state and could be described using density matrix formalism Eq. 3.6. Because of relatively low collection efficiency, all experiments are repeated many times, and every time, the NV center experiences a slightly different ambient condition, so one cannot use pure states formalism to describe such an "averaged" result.

$$\dot{\rho} = \frac{1}{i\hbar}[H, \rho] - "(\rho - \rho^{Thermal})/T_{Equilibrium}" \tag{3.6}$$

Where ρ is a density matrix of the NV center, $\rho^{Thermal}$ is a density matrix corresponding to thermal equilibrium, the steady state of the system, and $T_{Equilibrium}$ is a characteristic time of decay to the thermal state. The Eq. 3.6 leads to an exponential decay pattern of the state. There are two types of relaxation - parallel (spin-lattice) and perpendicular (spin-spin).

3.4.1 Parallel relaxation

Parallel relaxation, also called spin-lattice relaxation, is a decay of the diagonal elements of the density matrix (also called populations) because of the interaction with lattice phonons [64]. The characteristic time of this decay is called T_1 time; sometimes, it could be just called "lifetime." To measure T_1, one can prepare NV center in state $|m_s = 0\rangle$ or $|m_s = 1\rangle$, let it evolve for time τ, which is a sweeping parameter, and then read out the spin state (see Figure 3.7 a). The probability to stay in the initial state will decay exponentially with T_1 time rate. Cooling the NV center to low temperatures significantly increases T_1 time. Thus, the attempt to

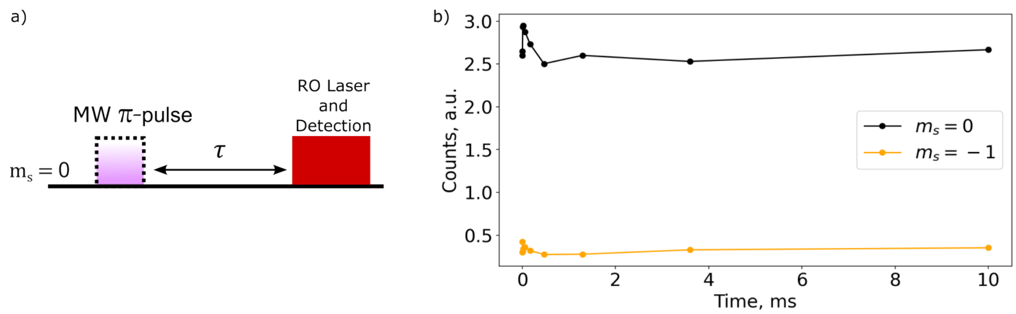

Figure 3.7: The T1 measurement. a) Scheme of the experiment - starting from the initial state $|m_s = 0\rangle$ (no MW $\pi - pulse$ application) or $|m_s = -1\rangle$ (if MW π - pulse is applied), the system evolves for time τ followed by the state readout. b) Experimental results: NV center was prepared in bright and dark states. There is no evidence of population decay after $\approx$ 10ms.

measure T_1 showed no noticeable decay seen for times of 10ms - which exceeds the timescale of any experiment covered in this thesis (see Figure 3.7 b).

3.4.2 Perpendicular relaxation

Perpendicular relaxation is the decay of a density matrix's off-diagonal elements, also called "coherences". The characteristic time is called T_2 [7], and it reflects how fast the phase between 2 states decays. The upper limit for T_2 is defined by T_1 - which makes sense - if populations get mixed, the phase between them no longer exists. More practical is to measure T_2^*, also called Free Induction Decay (FID) time - the decay due to spin-spin interaction with the surrounding bath. In the case of the NV center, the primary source of T_2^* decoherence is surrounding paramagnetic spins like ^{13}C or $P1$-centers. They create a local fluctuating magnetic field at the point of NV

center so that the resonance frequency is also fluctuating; because of this, the NV center acquires the additional random phase Equation 3.7 [151].

$$\phi = \gamma_e \int_0^\tau B(t)\, dt \tag{3.7}$$

This effect is called the Overhauser field [101] [78] [26], and it significantly limits the coherence of the NV center electron spin unless one uses dynamical-decoupling techniques to counteract this type of decoherence. One should also keep in mind that non-initialized ^{14}N nuclear spin gives $\pm A_{zz}(= 2.19MHz)$ uncertainty in qubit transition frequency. To measure the T_2^* time, one can use a technique called Ramsey spectrometry [110] Figure 3.8 a.

- Starting from initialized electron state $|m_s = 0\rangle$, a MW $\pi/2 - pulse$ rotates the state on the Bloch sphere around the x-axis to the equator Figure 3.8 c.

$$|\psi\rangle = \frac{1}{\sqrt{2}}(|0\rangle + |1\rangle) \tag{3.8}$$

- Then, during the free evolution time, the state vector starts to rotate in the equatorial plane with a frequency equal to detuning from the MW drive frequency (given that the drive is resonant). During each measurement, the detuning is random, so the "averaged" result is not a pure state, so the state vector does not have a full length and cannot be drawn on the Bloch sphere surface. Over time, its trajectory is a spiral leading to a completely mixed state, which is the center of the Bloch Sphere (blue line on second Bloch Sphere at Figure 3.8 c)

$$|\psi\rangle = \frac{1}{\sqrt{2}}(|0\rangle + e^{i\Delta\tau}\,|1\rangle) \tag{3.9}$$

- Second $\pi/2-pulse$ again rotates the state vector around the x-axis in the same direction, projecting it to the z-axis. The z-projection could be read directly by applying a resonant E_y laser. One can imagine that the signal will be sinusoidal but exponentially decaying; the characteristic time of the decay is the desired T_2^* time. Thus, the probability to read out the initial state $|m_s = 0\rangle$ is given by:

$$p(|m_s = 0\rangle) \sim sin(2\pi\Delta\tau) \cdot exp[-\frac{\tau}{T_2^*}] \tag{3.10}$$

Figure 3.8 b shows the effect of the detuning from the strongly coupled ^{14}N spin - when it is not initialized, the electron spin of the NV center experiences oscillations with a frequency corresponding to the hyperfine interaction ≈ 2.19 MHz, in accordance to Equation 3.10. In the case of the initialized nuclear $14N$ spin, it could not be seen. The decaying pattern is due to interaction with the surrounding spin bath [63]. It is worth mentioning that $1/T_2^*$ could be used to estimate the "strength" of the noise created by the surrounding spin bath, and this value also defines the width of transition (for example, in ODMR) measurements.

There is a way to counteract to some extent the perpendicular decoherence; it is called Dynamical Decoupling, in particular, Hahn echo sequence [55]. This method was borrowed from the conventional NMR field. It is similar to FID measurement mentioned above, but with the refocusing π - pulse after half of the free evolution time τ Figure 3.9 a. During the first $\tau/2$ the qubit acquires some phase ϕ_1 (Eq 3.6) because of the detuning, which can be understood as a movement on the equator of the Bloch sphere (the direction depends on the sign of detuning). Then the $\pi-pulse$ additionally rotates the state vector around the x-axis Figure 3.9 c, so that the phase ϕ_2, acquired during the next $\tau/2$ will be added to the ϕ_1 phase with a negative sign Eq.3.11

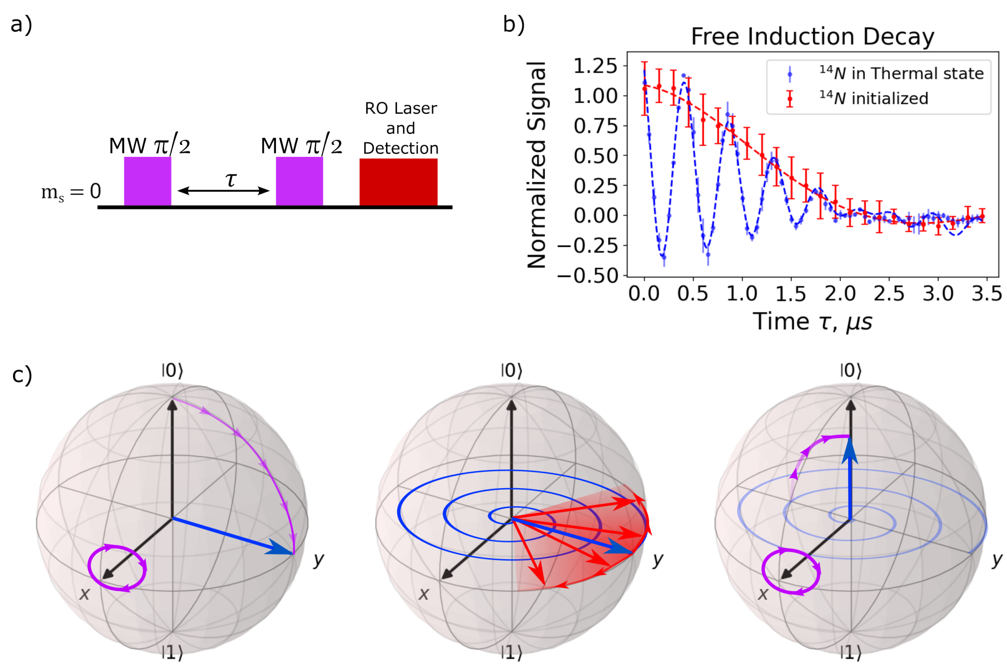

FIGURE 3.8: FID Ramsey measurement. a) Pulse diagram of the experiment - two separated by time τ MW $\pi/2$ pulses followed by state readout. b) Experimental results of FID measurements with initialized ^{14}N spin (red) and with ^{14}N spin in thermal state (blue). c) The electron spin state evolution on the Bloch sphere.

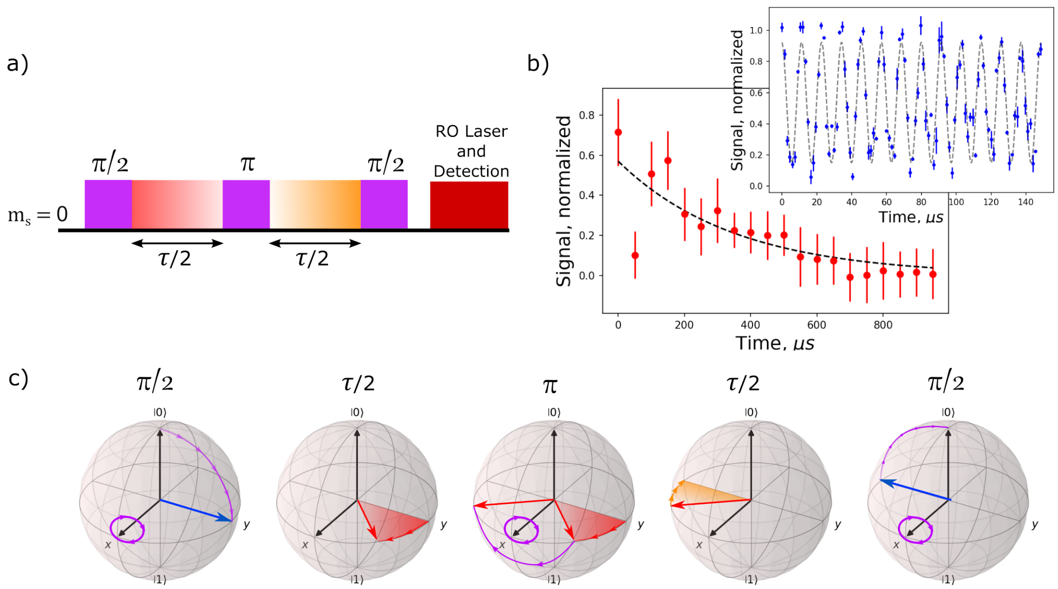

FIGURE 3.9: Hahn echo sequence. a) Pulse scheme, 2 MW $\pi/2$ pulses equidistant from MW π by time τ with the following state readout. b) Experimental results of the Hahn Echo measurement for relatively short and long times. Oscillations take place because of the interaction with surrounding ^{13}C spins

$$\phi = \phi_1 - \phi_2 = \gamma_e \left[\int_0^{\tau/2} B(t)\,dt - \int_{\tau/2}^{\tau} B(t)\,dt \right] \tag{3.11}$$

The Hahn echo method is good for refocusing static field contribution [27]. Of course, one can use many π - pulses with different phases to compensate for decoherence more efficiently. The protocols using such "refocusing" techniques are called Dynamical Decoupling techniques [128] [145] [93], they could significantly improve the coherence time of NV center [88]. The decaying exponent, measured with the

Hahn echo technique, is called T_2 time. The results are shown in Figure 3.9 b for long times (red) and short delay times (blue). One can see the decaying behavior of the signal on the long-range image. The oscillations on the short-range graph are due to interaction with the ^{13}C surrounding the NV center.

Chapter 4

Experimental Setup

A robust experimental setup is essential to implement spin-photon entanglement. This chapter details the arrangement used in the experiments, containing the optical and electrical parts. It begins with discussing the confocal setup, highlighting the excitation and detection paths, and includes specific methods for detecting Zero Phonon Line (ZPL) and Phonon Side Bands (PSB) emissions. The chapter then covers the interferometer's design and function, including using an Electro-Optical Deflector (EOD). Additionally, it provides an overview of the NV device used and the role of the Field Programmable Gate Arrays (FPGA) in the setup. This thorough examination of the experimental apparatus lays the groundwork for understanding the precise conditions and configurations necessary for successful spin-photon entanglement experiments.

4.1 Confocal Setup

All the experiments were performed on the home-built confocal setup, that is suitable for a wide range of applications. Conventionally, the setup can be divided into 2 parts - excitation, where all the lasers are getting coupled to the fibers and the excitation lights are getting delivered to the NV center, and collection - where the light emitted from the NV center is getting collected), see Figure 4.1.

4.1.1 Excitation path

The excitation part of the setup consists of 4 lasers

- 520nm green diode laser, which is mainly used to measure a fluorescence map and to focus on the NV center;
- 575nm yellow laser, resonant with NV^0 ZPL line, is used to repump from undesired NV^0 charge state back to NV^-;
- 637nm spin-reset laser, which is resonant to $E_{1,2}$ transitions of the NV^- and used to initialize electron spin to $|m_s = 0\rangle$ state;
- 637nm laser is resonant with E_y transition and is used for entangled photons generation and electron spin-state readout.

The light from E_y laser is divided into 3 paths - the first one is used for generating short optical π - pulses and coupled through an electro-optical modulator (EOM), followed by an acousto-optical modulator(AOM). The EOM is responsible for the creation of short Gaussian-shape excitation pulses (FWHM = 2ns). Still, it should

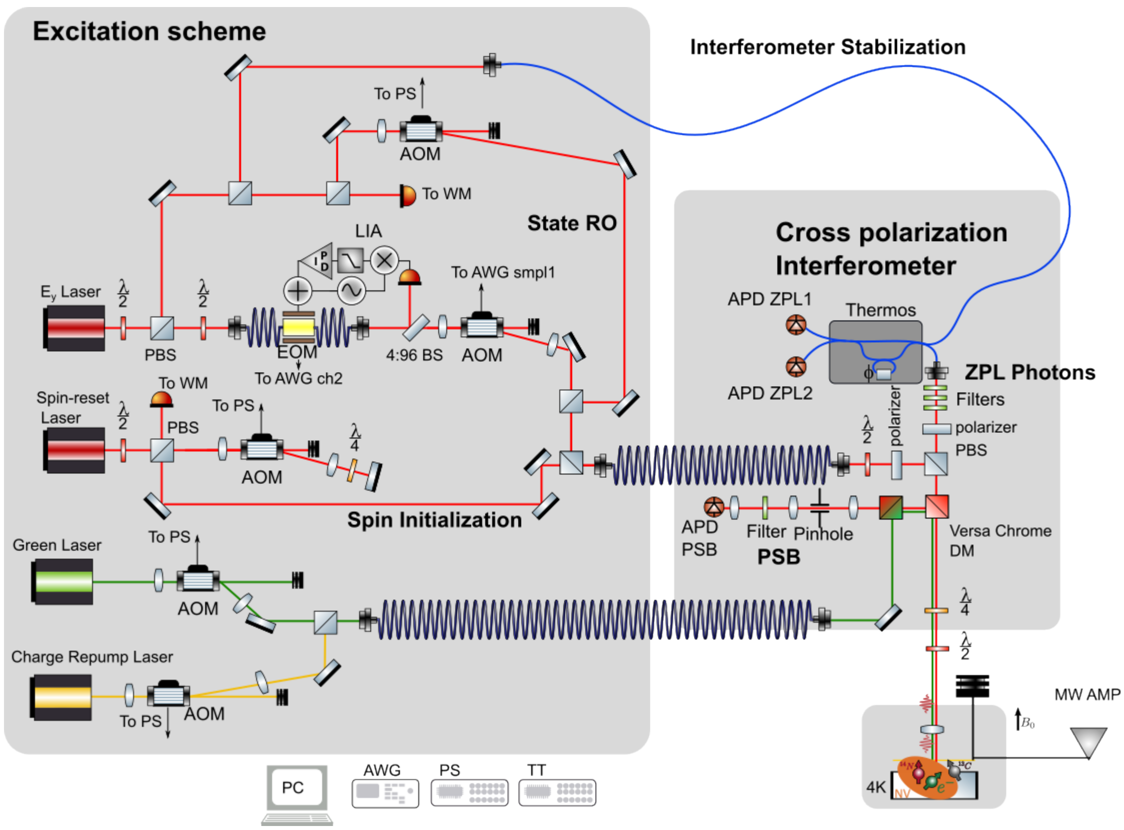

FIGURE 4.1: Confocal Setup. It could be divided into 2 parts - excitation and detection. The excitation part shows how lasers are coupled to the excitation fibers. The detection part has Zero Phonon Line (ZPL) detection and Phonon Side Band branches (PSB). The sample is located in the cryostation and operated under 4K.

be noted, that EOM alone is not sufficient because of its relatively low extinction ratio (1:1e3) - therefore following AOM (1:1e6) is required.

The second path also has another AOM and is used for resonant electron state readout - with this readout power can be controlled and to be different from optical π-pulse generation power. Notice, that AOM shifts laser light frequency, which is why it is important to have it coupled to the same order as with π pulse generating AOM. Otherwise laser light frequency in the first and the second path will have different frequencies.

The third path is coupled to the interferometer and used for phase stabilization. It doesn't go through AOM, so its frequency is shifted to two other paths, which leads to a constant phase difference measured on the interferometer with two other paths - $\pi - pulse$ generating one and the state readout path.

Spin-reset laser $E_{1,2}$ is also coupled through AOM so that it can be applied pulsed way. All the red lights are coupled to the same Polarization-Maintaining (PM) fiber, which serves as an excitation light source in the cross-polarization scheme. Green and yellow lasers are coupled in another polarization-maintaining fiber, through which the $NV - center$ can also be excited.

Optical π - pulses. The protocol implies the optical π - pulses excitation, to selectively address $|m_s = 0\rangle$. The optical $\pi - pulses$ have a Full Width Half Maximum (FWHM) of 2ns, to be shorter than the NV center lifetime ($\approx$ 12 ns [67]), but not too short - otherwise its broad spectrum can overlap with undesired transitions. To generate such optical pulses Gaussian-shape electrical pulses were sent from an Arbitrary Waveform Generator (AWG), trough amplifier to the EOM [59]. In the experiment an AC-coupled amplifier was used, and DC 50 Ohm coupled EOM. In such a connection scheme, there were some unwanted ringing effects, causing unwanted after-pulses. To compensate for this after-pulsing, electrical signal shape should be such, to have this after-pulsing coming after a certain delay, when AOM

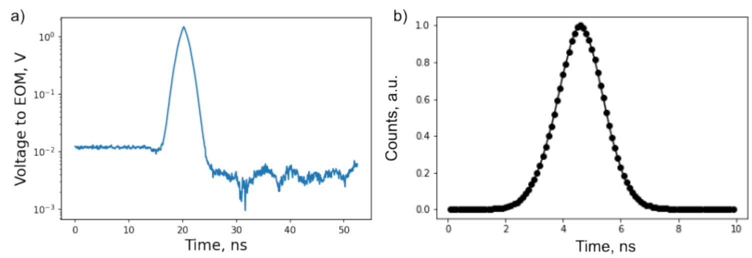

FIGURE 4.2: EOM pulses. a) Calculated waveform, that was sent to EOD from AWG, to get a Gaussian-shape pulse profile, exciting the *NV* center b) Measured on APD photon arrival time histogram, showing perfect Gaussian-shape laser pulse, FWHM = 2ns

completely blocks the light [91]. The resulting pulse shape sent to the EOM and measured on the APD signal are shown in the Figure 4.2.

4.1.2 Detection path

The detection path of the setup could be considered as two parts - a cross polarization scheme for Zero Phonon Line (ZPL) photons detection and path for Phonon Side Band (PSB) photons detection.

Phonon Side Bands (PSB) detection

Because of the relatively low Debye-Waller factor (only 3 % of the *NV* center fluorescence will be emitted in ZPL, and 97 % in PSB), PSB photons are normally used for reading out the state of the *NV* center, while ZPL photons could be used to generate spin-photon entanglement. To suppress the background light, the confocal microscope system was implemented - a pinhole was installed in the focus of the telescope system. The first lens is fixed on a stage mount and used to align the confocal system, the pinhole is placed to be in a "focus" of free-space Avalanche

Photo Detector (APD), so the pinhole adjustment implies a small re-adjustment of the APD (not big, because the APD detection surface is $\approx 300\mu m$, which is bigger than the pinhole size of 50 μm)

Zero Phonon Line (ZPL) detection

For the spin-photon entanglement, resonant excitation must be used, meaning all the ZPL photons emitted from the NV^- center have the same frequency as the laser. That is why only polarization filtering is possible, to filter the NV signal from the laser noise. Luckily, two ZPL transitions, that potentially could be used for entanglement generation $|0 \leftrightarrow E_x\rangle$ and $|0 \leftrightarrow E_y\rangle$, correspond to two different dipole moments, perpendicular to each other [72] [8]. So the emitted photons are also linearly polarized. Taking this fact into account, a cross-polarization scheme can be implemented[77]. In this scheme, the polarization of the excitation laser is perpendicular to the polarization of the collected photons[16](see Figure 4.3 a). To go more in detail, the cross-polarization scheme works as follows (see Figure 4.3 b): The optical setup involves linearly polarized laser beam coming from the optical fiber. This beam encounters a half-wave plate, which adjusts its polarization to align with that of the polarizer. Subsequently, the linearly polarized light is directed to the polarizing beam splitter, where it reflects and is guided toward the NV defect. Within the optical path, a quarter-wave plate plays a crucial role in compensating for the birefringence of the lens and the entire apparatus. Another half-wave plate is placed to align the incident light's polarization with the dipole moment of the NV center. The transition is excited, by the laser's polarization projection onto the dipole axis, resulting in an emitted photon with linear polarization corresponding to the dipole moment. A portion of this linearly polarized emitted light passes through the polarization beam splitter, and after traversing an additional polarizer and light filters, it enters the polarization-maintaining optical fiber. This optical fiber is responsible for collecting resonant photons emitted by the NV center and additionally acts as a confocal "pinhole". In this scheme, the excitation polarization won't be optimal (because the only projection of laser polarization to the NV-dipole axis can excite the transition), and also part of the collected photons will be lost, but this is an inevitable price that must be paid.

To check the cross-polarization setup performance two consecutive optical π-pulses were applied to the NV center with the following collection of fluorescence (i.e. measuring the lifetime of the excited state of the NV-center). The result is given in Figure 4.4, where laser leakage through the cross-polarization scheme (orange curve) and also signal from the NV center (blue curve) can clearly be seen. The cross-polarization setup doesn't suppress unwanted laser light completely, but the laser pulse and NV signal are well separated in time, so additional "time filtering" was also used, meaning only the photons, that arrived to the detector within the specified detection window (see grey area on Figure 4.4) are considered.

4.2 Unbalanced Mach-Zehnder interferometer

To convert the time-bin basis of the photon qubit into a spatial dual-rail one, an unbalanced Mach-Zehnder interferometer was used [90][129]. It is completely fiber-based and in the first version included two fiber beam splitters (the second version had an Electro-Optical Deflector, it will be detailed in the section 4.3), spliced with 2 arms - long and short, the difference in length of which is equal to

$$\Delta L = c\tau_{EL}/n \approx 11.5m \tag{4.1}$$

where c is the speed of light in vacuum, n is the refractive index of the fiber and τ_{EL} is the time difference between $|Late\rangle$ and $|Early\rangle$ time bin modes in the time-bin basis

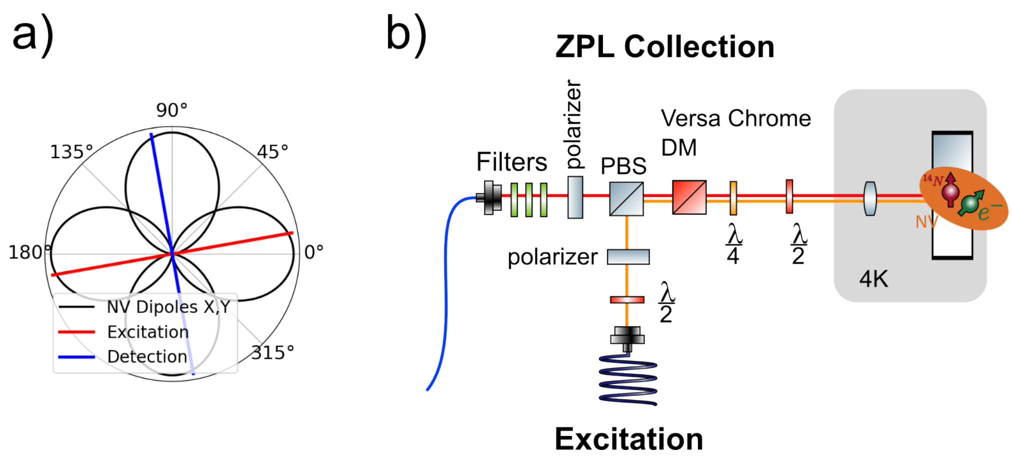

FIGURE 4.3: Cross polarization-excitation scheme. a) Collected polarization (blue) is perpendicular to the exciting one (red), allowing efficient filtering of the laser light. The radiation pattern of the 111 oriented NV center is two perpendicular in-plane dipoles (bold black lines) - corresponding to E_x and E_y transitions. The cross-polarization setup is aligned, to efficiently collect the majority of the emitted light, sacrificing the excitation efficiency. b) Cross polarization part of the setup. The laser polarization is getting reflected on the PBS. This results in the transmittance of perpendicular one from the NV center through the PBS and its coupling to polarization maintaining fiber. $\lambda/2$ is used to align the cross-polarization scheme to the polarization patterns of the NV center. $\lambda/4$ is used to compensate for the setup birefringence.

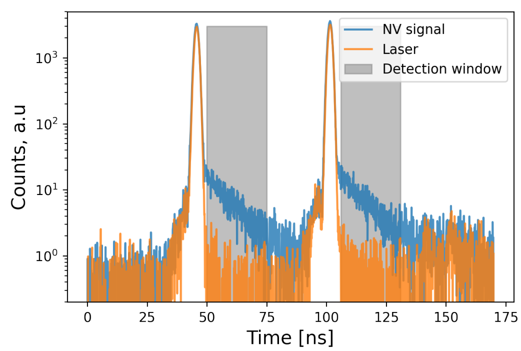

FIGURE 4.4: Cross Polarization Setup Performance. The histogram shows the photons detection time for the two consecutive Gaussian-shape excitation pulses applied. The orange curve depicts the background, measured next to the NV center and blue curve shows the NV center signal itself. The difference is due to photons emitted directly by the NV center. The exponential T_1 decay of ≈ 12 ns on a logarithmic scale looks like a line[67]

of the photonic qubit (see Figure 4.5 a). So that, at the end of the interferometer (after the second beam splitter) the detector can measure the photon in one out of three possible time windows:

- $|Early, Short\rangle$ - the most left peak, the shortest time
- $|Early, Long\rangle$ or $|Late, Short\rangle$ - the middle peak corresponding to the ideal overlap of two temporal modes and the redefinition of the temporal basis into a spatial one
- $|Late, Long\rangle$ - the most right peak, the longest time

In the entanglement experiments the central peak was used, because the information about "in which time bin the photon was emitted" is erased there and there is an one-to-one correspondence between time and spatial bases states (see Figure 4.5 c). The photon acquires different phases in the different arms of the interferometer, so that the phase difference could be expressed as:

$$\Delta\phi = 2\pi \frac{\Delta L + \delta L(t)}{\lambda} \tag{4.2}$$

where λ is wavelength of the photon, $DeltaL$ is the arms length difference 4.1 and δL is the length fluctuations due to a temperature drift. It can be seen, that the expansion of one arm to another by $\approx 637nm$ gives a 2π phase acquisition to the photon, so stabilization of the interferometer is important. Conversely, by manually adjusting the length of one arm, such as using a fiber-stretcher, the phase of the interferometer can be manipulated. This fiber-stretcher functions essentially as a piezo device attached to the fiber, enabling a phase control through a voltage application (see Figure 4.6 a). To solve the problem of the random temperature fluctuations, the interferometer was glued via tape to a styrofoam pallet, which in turn was placed

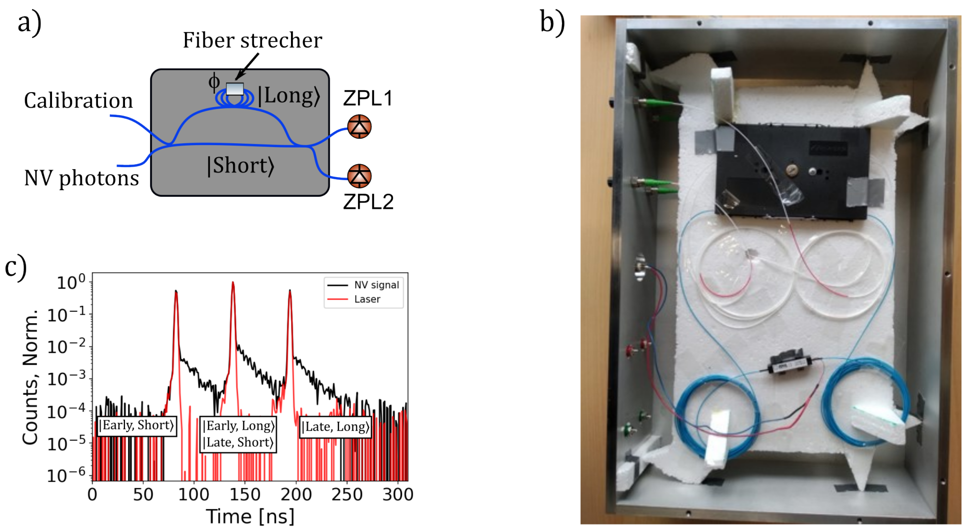

FIGURE 4.5: Interferometer a) Sketch of the interferometer, two inputs are used to couple the signals from the NV center and the calibration laser, two outputs are connected to two APDs (ZPL1 and ZPL2), the fiber stretcher is used to set the interferometer's phase b) Photo of the interferometer in the box c) Histogram of photon arrival times after two-pulse excitation - the NV signal can clearly be distinguished from the laser noise.

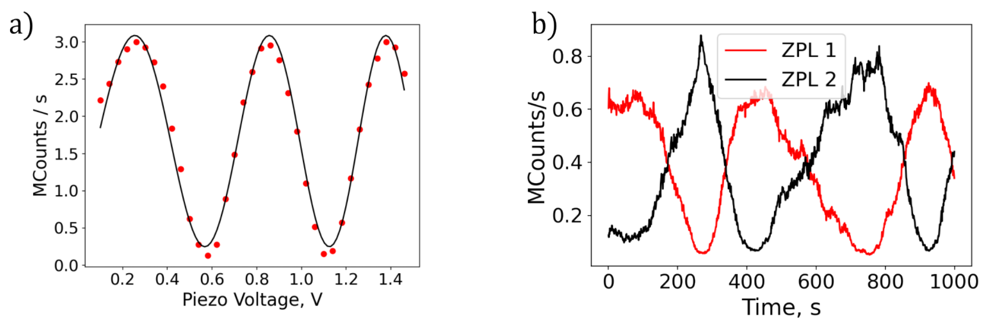

FIGURE 4.6: a) Interferometer scan, counts at one of the interferometer outputs vs the voltage applied to the fiber stretcher. b) Time drift of the interferometer, the signal at 2 different outputs vs time.

inside an aluminum box (see Figure 4.5 b), providing a good level of passive temperature stabilization (see Figure 4.6 b). In addition to this, the phase recalibration was done every ~ 3 seconds, i.e. refocusing the fluctuating phase sufficiently often. To be able to do this, the second input of the interferometer was used for the calibration - by sending the laser light and applying the voltage to the fiber stretcher, an interference pattern can be obtained (see Figure 4.6 a).

Another important feature was to use the polarization-maintaining fibers and to align the polarization of incoming photons. Otherwise, the photons start to acquire an uncontrolled phase due to the difference of refractive indexes between *ordinary* and *extraordinary* polarizations. In the setup PM630-HP fibers with FC/APC connectors, aligned along a slow axis were used.

4.3 Electro-optical Deflector in the interferometer

In the interferometer scheme described above, half of the photons are getting discarded ($|Early, Short\rangle$ and $|Late, Long\rangle$). A natural way to solve this problem is to

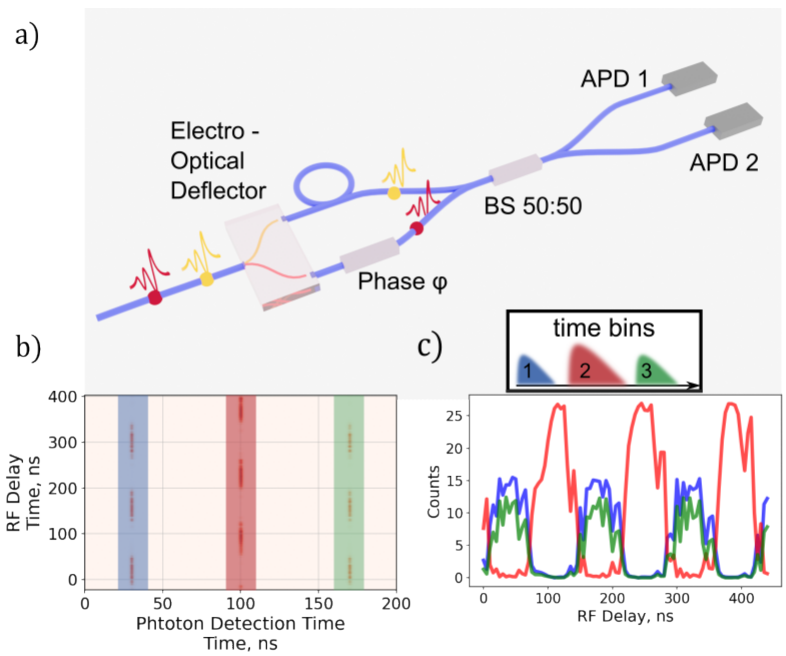

FIGURE 4.7: Interferometer with the EOD. a) Sketch of the interferometer with a built-in EOD b) 2D colormap of the photon detection probability (color encoded) at different times (horizontal axis) for the different delays of the EOD RF drive (vertical axis). The shaded area reflects the time bins from the inset in the picture c. c) Three Gaussian fit's amplitude of the picture b), in other words - the vertical cut of the picture b. Different colors correspond to the different time bins (see inset on top of the picture c)

direct the photons to the appropriate arm of the interferometer using some kind of active device, instead of a passive beam splitter. In the second version of the interferometer an Electro-Optical Deflector (EOD) [85] was integrated instead of first beam splitter (see Figure 4.7 a). The EOD is the device that can quickly switch between 2 states - in the one state the photons are sent to one arm of the interferometer (for example $|Long\rangle$) and in another state of the EOD, to another arm (for example $|Short\rangle$). With a correct synchronization between the EOD drive and the optical pulses, $|Early\rangle$ coming photon can be guided to the $|Long\rangle$ arm and $|Late\rangle$ photon to the $|Short\rangle$ arm, providing an efficient photon routing. The EOD is driven with a frequency corresponding to a 70ns switching rate between two different arms (7.143 MHz) - matching the length difference of the interferometer (second version) arms. In the Figure 4.7 b, the 2D colormap can be seen, it shows how the delay, between the RF driving (of the EOD) and the optical pulses, influences photon arrival time. In the case of the ideal delay, photons coming only in the central window (red-shaded area in the Figure 4.7 b) should be seen. For the each delay time, the photon detection time histogram was fitted with three Gaussians, and a graph Figure 4.7 c was constructed from the fit data - it shows the amplitude of each of the three Gaussian pulses against the delay time.

4.4 NV device in diamond

In this work, the synthetic diamond sample was used. It was grown homoepitaxially on a $\langle 100\rangle$-oriented synthetic diamond using a microwave-assisted chemical vapor deposition (CVD) technique, with the following cleaving to get $\langle 111\rangle$ oriented sample [144]. The resulting IIa diamond has a low nitrogen concentration ($< 5ppb$). The low-strain ($\approx$ 1.2 GHz), $\langle 111\rangle$-oriented NV center with no strongly coupled ^{13}C in proximity was chosen for further manipulations. To enhance collection efficiency, a Solid Immersion Lens (SIL) with a $10\mu m$ diameter was fabricated in Weierstrass geometry using Focus Ion Beam (FIB) technology (see (Figure 4.8 a), which together with an anti-reflection coating, deposited on top of the diamond and SIL letting to the saturation count rate above 0.9 MHz when paired with the ZEISS Objective EC EPN 100x/0.9 DIC. In turn, inside the cryostation, the diamond is located on movable scanners, with the help of which the NV center is located at the focus of the fixed objective. And also, with the help of the scanners, confocal image can be obtained.

For the MW and RF supply, the $20\mu m$ wire was placed next to the SIL. The wires inside cryostation have a distinctive transmission spectrum Figure 4.8 b - high frequencies pass through the sample with greater difficulty, thereby requiring a powerful amplifier.

Anti-Reflection coating.

Diamond has a high refractive index to the vacuum $n_{Diamond} = 2.4$, which results to a significant proportion of light being reflected from the interface between the two media ($\sim 15\%$ for the air-diamond interface) [104]. So, part of the excitation light is getting reflected and, what is more important, the signal from the NV center is also getting lost. Partially, the problem of efficient light collection is solved by using a Solid Immersion Lens (SIL), which helps to collect the light that in its absence would experience total internal reflection. Another possible improvement would be to deposit on the diamond surface an anti-reflection coating (see Figure 4.9). When light hits the interface between two media, some of it is getting reflected from the surface (this physics is described by Fresnel coefficients). The idea of applying the anti-reflective coating is to have a "special" layer of a given thickness and a given refractive index so that, the two waves reflected from the two surfaces of this layer interfere in anti-phase and cancel each other out.

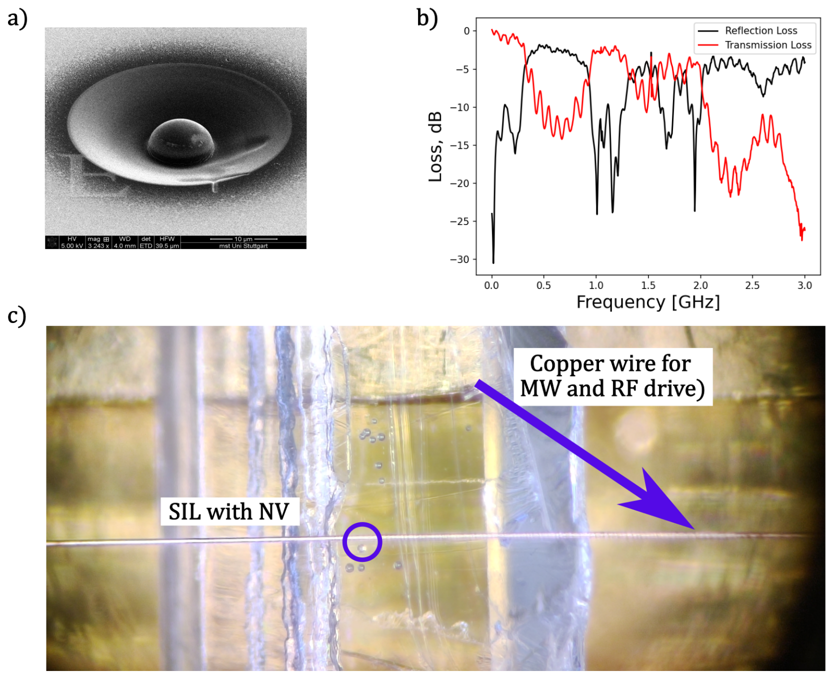

FIGURE 4.8: NV device in the cryostation. a) ESM image of the SIL with NV center b) Transmission Loss (red) and Reflection Loss (Black) characteristics of the microwave line in the cryostation. c) Sample image in an optical microscope (x40). SIL with the NV center is highlighted, arrow points to a $20\mu m$ copper wire. Other SILs in the picture can also be distinguished

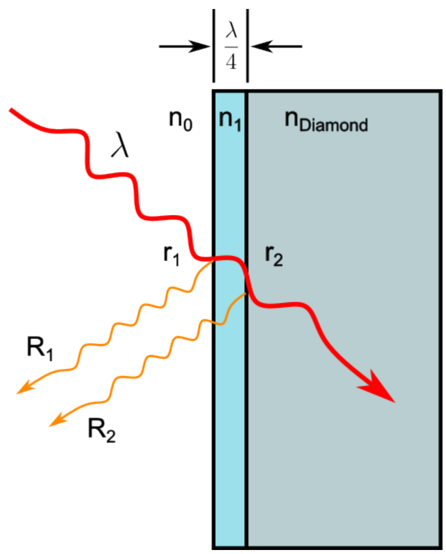

FIGURE 4.9: Anti-reflection coating. Reflective indices and layer width are chosen, to have reflected beams R_1 and R_2 to be in anti-phase and to interfere destructively.

If a plane wave described by the equation 4.3 is incident on the interface between two media, then two reflected plane waves could be described as in the equation 4.4:

$$I = I_0 cos(\omega t + kx) \tag{4.3}$$

$$\begin{aligned} R_1 &= I_0 r_1 cos(\omega t + kx) \\ R_2 &= I_0 r_2 cos(\omega t + kx - 2k_{film} d_{film}) \end{aligned} \tag{4.4}$$

Where I_0 is an amplitude of the incident light, r_1 and r_2 are reflection coefficients from the 1st and 2nd surfaces, d_{film} is a thickness of the AR-coating film and k_{film} is a wave number in the film, $k_{film} = \frac{2\pi n_1}{\lambda}$. To have the reflected beams interfere destructively, two following conditions must be satisfied: 1) $r_1 = r_2$ and $cos(\omega t + kx) = -cos(\omega t + kx - 2k_{film} d_{film})$. This happens, when $n_1 = \sqrt{n_0 n_{Diamond}} \approx 1.56$ and $d_{film} = \lambda/4$. In the experiment Al_2O_3 ($n = 1.77$ at 637nm) was used as an AR-coating material, due to the technical ease of its application. Despite of non-optimal refractive index, significant suppression in reflection light - about 4 times from 14% to 3.5% was achieved.

4.5 Electrical part of the setup

The electrical connection diagram is shown in the Figure 4.10. To generate analog signal two synchronized AWGs are used, they have in total four 12 GSample/s outputs, that are used to generate MW and RF signals as long as electrical pulses for EOM (to generate optical $\pi - pulses$) and driving signal for EOD. All the analog signals are amplified and sent to corresponding devices - the RF and MW signals are combined on a multiplexer and then wired to the cryostation. It is worth mentioning, that the MW amplifier, because of its wide-range parasitic noise, is coupled to the main experiment through a high-power switch. This prevents unwanted mixing of the NV center ground state sub-levels. The AWGs have only 8 digital outputs, which is not enough to control the whole setup, so Pulse Streamer with an additional 8 digital outputs was added. The internal clocks of the 2x AWGs and the Streamer Pulse were synchronized.

In the majority of experiments, when the FPGA is not used, the AWG number one serves as a master device, that triggers the second AWG and the Pulse Streamer - they both run the written sequence once, waiting for the next trigger from the master device to run the sequence for another round. In experiments that use the FPGA, the trigger sequence is looped - as soon as the FPGA completes its operation, a trigger signal is sent to the AWG one, which in turn sends a trigger to the AWG two and the Pulse Streamer. At the end of its sequence, the Pulse Streamer sends a trigger signal to the FPGA, that allows the FPGA to start its routine again. Access to some resources like lasers is required for both - the FPGA and the two AWGs + Pulse Streamer system. Because of this, set of logical "OR" gates are implemented on the FPGA board - the signal to (for example) a yellow laser is sent from the FPGA when either the FPGA wants to do it or when the corresponding signal comes from the Pulse Streamer (and the FPGA just pass it further). Additionally, the FPGA operation includes steps, that require access to the lasers and photon clicks, so that, all the APD signals are getting copied and sent to both - the FPGA and the Time Tagger. The Time Tagger is the main device to register signals arrival times, letting to efficient process of the data, control detection windows and simply counting the amount of detected photons. For the synchronized detection among the photons and all the signal-generating devices, a bunch of the synchronization signals are wired to the Time Tagger (magenta lines on the diagram). The two digital signals coming from the AWG one to the optical π-pulse AOM and to the Time Tagger are subject to increased requirements for synchronization and accuracy since they

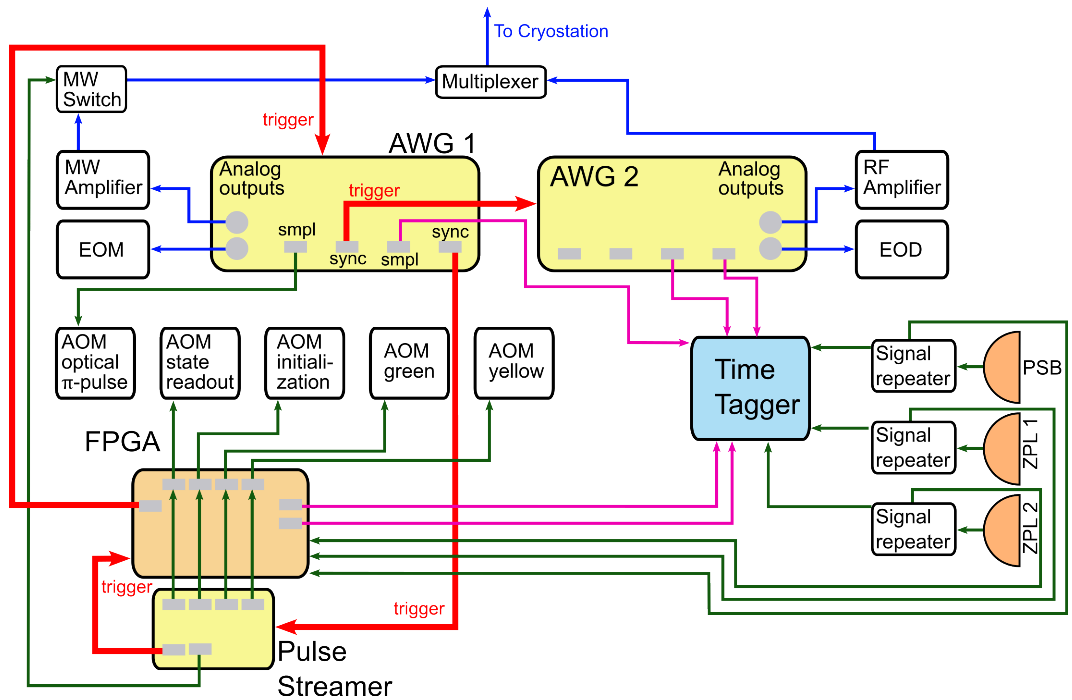

FIGURE 4.10: Electrical Part of the Setup. All the signals are generated on four devices - two AWGs + Pulse Streamer and FPGA (yellow and light-orange). Signals are detected on the Time Tagger (blue). Interdevice-triggering signals are shown as red bold lines, green lines represent digital control triggers to different setup parts, blue lines represent analog signals and magenta lines show synchronization signals to the TimeTagger. Clicks from the APDs (PSB, ZPL1, ZPl2) are getting copied and sent to the TimeTagger (main counting device) and the FPGA (for FPGA decision-making routine).

directly affect the accuracy of the detection time of the entangled photon - that is why it was better to have them on fast device like the AWG and not on the Pulse Streamer. Furthermore, two synchronized National Instruments cards were employed for confocal scanning of the sample, adjusting the wavelengths of the resonant lasers, controlling the interferometer's phase, and managing the powers of AOMs (laser powers) – as well as monitoring the voltage output of the photodetector for logging laser powers.

4.6 Field Programmable Gate Array (FPGA)

When subjected to a laser radiation, the NV center can undergo ionization, transitioning to the undesirable charge state NV^0. To efficiently and swiftly control the charge state of the NV center, a field programmable gate array (FPGA) was employed [104] (see Figure 4.11). The NV^0 exhibits a distinct system of levels where red lasers are non-resonant, causing the NV center to enter a "dark state." Therefore, by illuminating the NV center with two red lasers (resonant to transitions with spin projections $|m_s = 0\rangle$ and $|m_s = \pm 1\rangle$) and detecting a photon count exceeding a specified threshold, the NV center can be inferred is in a correct charge state NV^-. Conversely, if the photon count is below the threshold, the NV center can either be considered to be in the NV^0 charge state or NV^-, but not on resonance with the lasers anymore (for example, because of the spectral diffusion effect). This necessitate the application of a repump laser to bring the NV^0 back to the NV^- state in the first case or to "shake" the charge bath around the NV^- center to bring transitions back to the resonance in the second case. In both cases the efficiency of the repump laser application is probabilistic, and the process is iterated until the specified threshold in amount of the detected photons is met. Alternatively, if the number of unsuccessful attempts becomes sufficiently high, it becomes more practical to refocus the objective on the NV center and remeasure the positions of the resonant transitions. The algorithm refrains from repeating the charge checking routine after each measurement, because the lifetime of the NV^- center charge state is longer than a single sequence iteration. Instead, the system transitions into the charge state control mode every e.g. thousand measurements, resuming data collection only after confirming the NV center is in a functional state.

Moreover, in the entanglement experiments, the FPGA additionally used to speed up the experiment as follows: detecting an entangled photon is a low-probability process (due to the low Debye-Waller factor and low collection efficiency) - therefore, it makes sense to read out the electron spin state of the NV center only when the corresponding entangled photon has been detected (see Figure. 4.11, red shaded area). With that time can be saved, by not doing unnecessary state readouts.

The utilization of the FPGA is particularly crucial in the experiments involving the photon phase. The FPGA's role in controlling spectral diffusion ensures the ability to manipulate the phase acquired by the photon. Any frequency shifts of the photon results in a corresponding alteration of the acquired phase, emphasizing the significance of precise the spectral control facilitated by the FPGA (see Figure. 4.12a).

The resonance position of the NV^- center experiences spectral diffusion, so the distribution of the collected photons during charge state checks procedures, using the aforementioned procedure (count photons during two resonant laser illumination), is a sum of Poisson distributions, corresponding to different values of the spectral diffusion (detuning). Whereas with the FPGA resonance-filtering, only a few close Poissonians, corresponding to high average (i.e. small detuning) is not filtered out, giving a distribution, that can be fit as two Possonians - corresponding to NV^0 and NV^- states (see Figure. 4.12b). Thus, the use of the FPGA is an important tool in suppressing the spectral diffusion effect, as well as in accelerating the experiment.

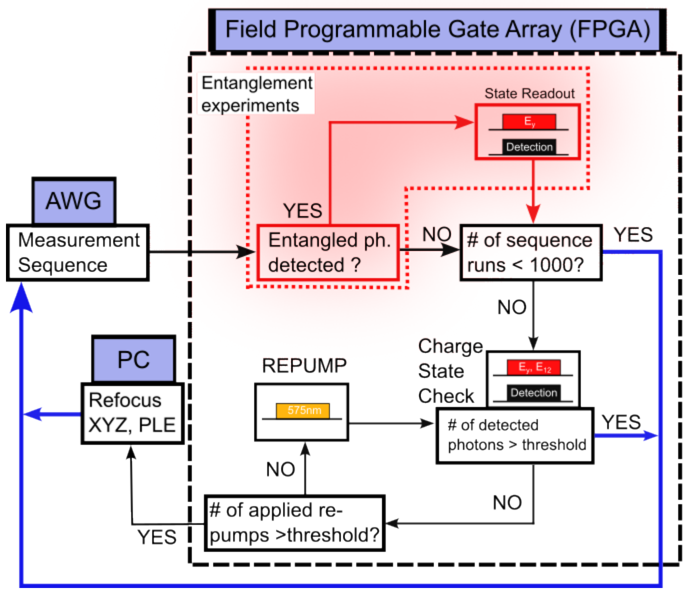

FIGURE 4.11: FPGA algorithm, FPGA performs charge state check and decides if the experiment can continue or repump routine must be applied. The red shaded area is optional and used only in the entanglement experiments.

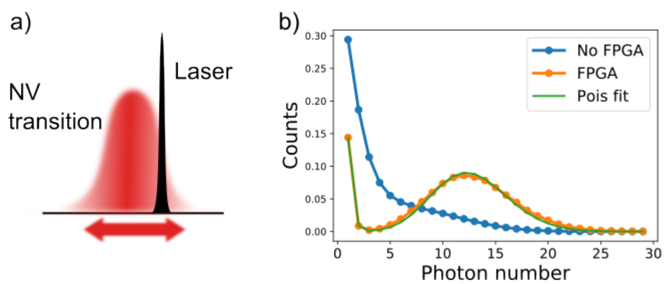

FIGURE 4.12: a) The idea of Spectral Diffusion, NV center transition is jumping because of the NV center interaction with electrical charges b) Distribution of the measured number of photons with (fitted with Poisson distribution) and without FPGA (sum of many Poisson distributions, not fitted).

Chapter 5

^{13}C spins as a quantum memories

This chapter focuses on identifying the nuclear ^{13}C spin bath surrounding the NV center to find optimal candidates for quantum memory applications, potentially offering advantages over the ^{14}N nuclear spin. It details the methods used to determine the nearby ^{13}C spins, beginning with Hahn Echo and XY4 techniques, followed by implementing the 5-pulse ESEEM method. The chapter concludes with a analysis of the HYSCORE technique, providing a comprehensive overview of the various approaches employed to characterize the ^{13}C spin environment. This investigation is crucial for enhancing the understanding of spin dynamics in the NV center and improving the performance of quantum memory systems.

5.1 Determination of the surrounding ^{13}C spins

The ^{14}N nucleus has been explored as a potential quantum bit for use as a quantum memory. Its strong coupling allows for the rapid operations, such as executing quantum gates that swap the electron spin quantum state with the ^{14}N nuclear spin [144]. However, this strong coupling also introduces an unwanted side effect. The excited state of the NV center has a different hyperfine coupling [36], and together with spontaneous relaxation to the ground state, it leads to the dephasing of the ^{14}N spin quantum state [130]. Consequently, there are better choices than the ^{14}N nucleus as a quantum memory for optically probed systems, which are often required in quantum networks [108]. A better candidate for quantum memory or error correction is the hyperfine coupled paramagnetic isotopes ^{13}C [23], which have a natural abundance of 1.1% in the diamond. The distance between them defines the coupling to the NV center. The ^{13}C spins with a coupling strength in the range of the 10 - 100 kHz are of interest, but the coherence time of the NV center electron spin is a limiting factor in their detection [141].

5.1.1 Hahn Echo and XY4

There are several well-established techniques to detect the weak hyperfine couplings longer than T_2^* ($\approx 1\mu s$) [147]. One of them is the Hahn echo method, which is a widely used technique in nuclear magnetic resonance (NMR) and electron spin resonance (ESR) to refocus the dephasing spins and measure their coherence times. The sequence has the refocusing π - pulse that inverts the direction of the dephasing. Figure 5.1 shows the measured echo signal. A strong modulation with a periodicity of around 33 μs is evident, which aligns with the Larmor precession [80] of ^{13}C nuclei at the applied magnetic field ($\approx 60kHz$). This specific modulation occurs in $S = 1$ systems because no hyperfine coupling happens in the $m_s = 0$ sublevel, causing all

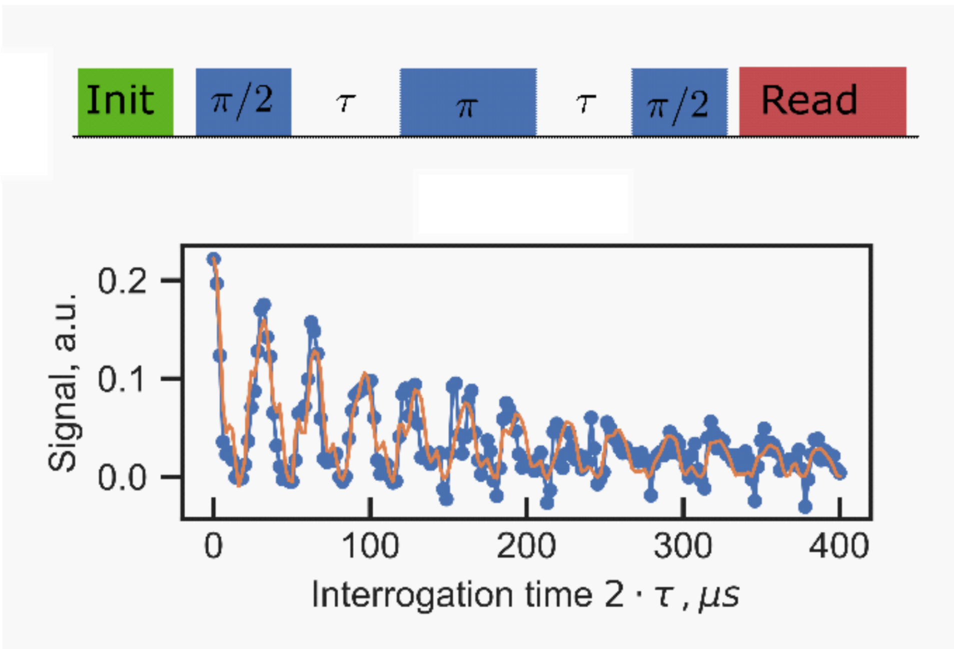

FIGURE 5.1: Hahn echo on the defect with π pulse lengths of 29 ns. The data panel shows the echo amplitude as a function of a waiting time, indicating a strong spin echo envelope modulation (ESEEM). The fit model presents an ESEEM analytical solution for two ^{13}C nuclei with fixed hyperfine coupling found from correlation spectroscopy and four other nuclear spins as the fitting parameters (see below).

nuclei in the sample to process at the same frequency. Additionally, on top of the revival pattern, ESEEM (Electron Spin Echo Envelope Modulation) features arise from individually coupled nuclear spins, showing extra modulation. However, due to the strong echo modulation from free precession, this pattern alone is insufficient to determine the hyperfine coupling parameters. To resolve these smaller hyperfine couplings, higher-order decoupling sequences can be used to extend the electron spin coherence time further, enabling the detection of even smaller couplings. These techniques have been previously developed for single spin detection and are suitable for discussing the detection of hyperfine couplings down to a few kilohertz. Many π pulses can be applied and, on top of this, their phase can be varied (having X and Y pulses) to compensate for the pulse duration and detuning errors. These pulse sequences detect nuclear spins by making the signal detected by the electron spin proportional to the phase Φ it acquires during the sequences. This accumulated phase is given by [33]:

$$\Phi = \int_0^t \gamma B_{nuc}(\tau)\delta(\tau)\, d\tau \tag{5.1}$$

where $\delta(\tau) = \pm 1$ - the modulation function, that alternates the sign after every π pulse. $B_{nuc}(\tau)$ is Larmor generated oscillating field at the point of the NV center.

As an example of the method, $XY4$ sequence was applied, and the signal was measured Figure 5.2. In this case the Equation 5.1 is given by [33]:

$$\Phi = \frac{\gamma B^{\alpha}_{nuc}}{2\pi\nu_{ac}}\left[\sin\alpha - (-1)^n \sin(2\pi\nu_{ac}t + \alpha) + 2\sum_{j=1}^{n}(-1)^j \sin(2\pi\nu_{ac}t + \alpha)\right] \tag{5.2}$$

where α is the detected phase of the signal, ν_{ac} is frequency of the signal and t is signal integration time from n nuclear spins.

For weakly coupled spins and high magnetic fields - the Larmor frequency will be much larger than the coupling frequency, so the peaks in the Equation 5.2 cause an apparent loss of coherence at the corresponding frequencies. The more decoupling pulses used, the weaker coupled spins could be identified [99]. In the case of the strongly coupled spins (i.e., their inverse coupling strength is larger than the decoherence time), the electron and nuclear spins interact coherently, so they become entangled throughout the pulse sequence. This is indicated in Figure 5.2, where the signal becomes equal to zero, making the traced-out electron spin state an effective thermal state. In such cases, assigning specific peaks in XY4 trace to specific values of the hyperfine coupling becomes a not easy task. Additionally, if the spectral density of couplings is large, individual peaks can no longer be resolved. This technique has been very successful in isolating the coupling to weakly coupled nuclear spins; however, it is not well-suited for spectroscopy on stronger coupled spins, like the ones used here [127]. This is mainly because strong coupling requires short pulse spacing, and the spin evolution does not correspond to classical noise but instead involves strong components due to coherent spin evolution.

5.1.2 5-pulse ESEEM

The main problem with the sequences mentioned above is that they are limited by T_2 - decay time of coherences (off-diagonal density matrix elements). It would be better to use a sequence limited by T_1 time - decay time of populations (diagonal elements) [1]. 5-pulse ESEEM is a well-known sequence for this Figure 5.3. The main idea is to create an entanglement of NV electron and ^{13}C nuclear spin via Echo Seqeuence and let it evolve for a time T_c and then apply a second Echo Seqeuence, that will interfere constructively or destructively with the first one - this depends on the duration of T_c. The approximate equation for the signal (valid for small signals when $\sin\alpha \approx \alpha$)

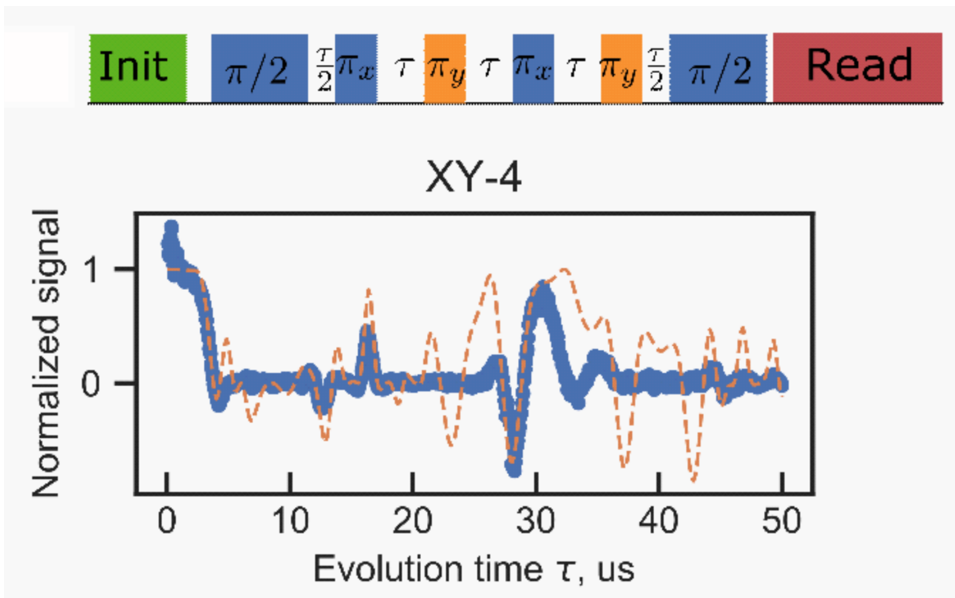

FIGURE 5.2: Pulse scheme of the $XY-4$ decoupling sequence(top) and the measured signal. The dashed line represents the simulation of the $XY-4$ sequence with nuclear spins identified from the fitting procedure in Figure 5.1

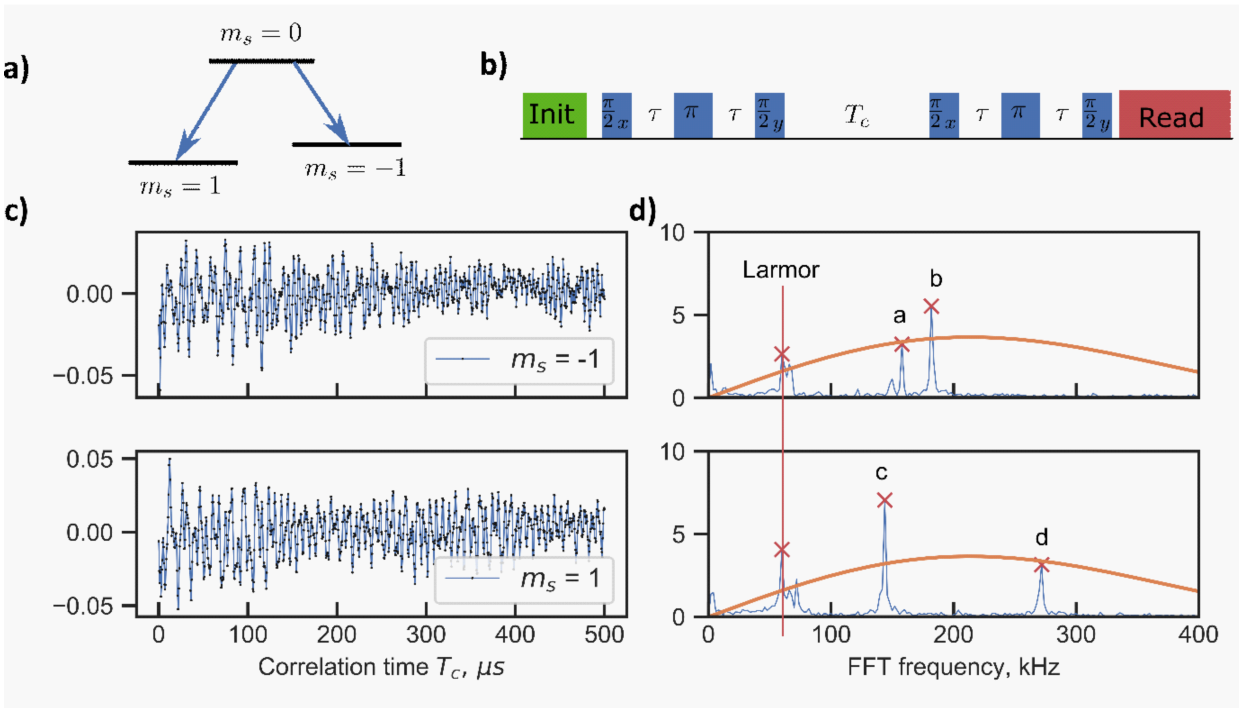

FIGURE 5.3: Correlation spectroscopy to resolve nuclear bath hyperfine spectra. a) Ground-state triplet energy level scheme. b) Correlation protocol pulse sequence, consisting of two Hahn echo sequences separated by a long correlation time T_c. The $\pi/2$ pulses at the end of each Hahn echo sequence are phase-shifted by 90°. c) Contrast data output from the measurement protocol, showing different beating features in the $|m_s = +1\rangle$ and $|m_s = -1\rangle$ sublevels. d) The absolute value of the FFT is applied to the data in (c), revealing the spectral features of the bath interacting with the central spin. The peak at approximately 60 kHz corresponds to the bare nuclear Larmor frequency, while other peaks represent the eigenfrequencies in the $|m_s = +1\rangle$ and $|m_s = -1\rangle$ sublevels for individual nuclear spins. The solid orange curve indicates the filter function of a single Hahn echo sequence, highlighting the resolution improvement achieved with the correlation sequence.

will be oscillating as [120]

$$S(t) \approx \sin^2(A^i_{zx}\tau)\left[\cos\omega_L T_c + \cos(\omega^i_{\pm 1}T_c)\right] \tag{5.3}$$

Where $A_{zx}\tau$ represents the maximum phase that can be accumulated during either of the two multi-pulse sequences, while ω_L and $\omega_{\pm 1}$ are the nuclear transition frequencies in the $m_s = 0$ and $m_s = \pm 1$ subspaces, respectively. As previously said, the resolution of $\approx (T_1)^{-1}$ is achievable because the signal is encoded in populations, not coherences. The resolution can be further improved if long-lived memory qubits are used [106].

The results of the measurement as a function of T_c for two different NV electron transitions $m_s = 0 \leftrightarrow \pm 1$ (Figure 5.3 a) are given on the Figure 5.3 c. Figure 5.3 d shows the Fourier transformations of both signals - peaks corresponding to different nuclear spins from 0 to 400 kHz can clearly be distinguished. The solid orange lines depict the signal resolution from Hahn Echo measurements, underlying the efficiency of the 5-pulse ESEEM method in terms of spectral resolution.

The peaks around 60kHz in Figure 5.3 d are identical on both Fourier transformations and related to Larmor frequency ω_L. However, the four other peaks (marked as a,b,c,d) are signals, coming from 2 unknown ^{13}C spins at frequencies given by [120]:

$$\omega_{\pm 1} = \sqrt{(\omega_L \pm A_{zz})^2 + A^2_{zx}} \tag{5.4}$$

Therefore, for the two ^{13}C spins, there are only two values for the combination of the four unknown parameters - $A^1_{zz}, A^2_{zz}, A^1_{zx}, A^2_{zx}$, which introduce an uncertainty in the unknown couplings parameters identification - which peak corresponds to which nuclear spin. A new measurement, which correlates signals between $m_s = \pm 1$ sublevels, is needed to resolve this issue.

5.1.3 HYSCORE

The idea of a HYSCORE [120] sequence is to separate T_c waiting time such that, during the first part t_1 the phase is getting accumulated in $m_s = -1$ subspace and then population conversion to the subspace $m_s = +1$ is happening to accumulate phase there during the second waiting part t_2 (Figure 5.4 a). This allows us to correlate nuclear coherences in different subspaces. 2D Fourier transformation yields correlated features (Figure 5.4 b) - which allows to extract coupling strengths (Table 5.1) and use them to fit the Hahn Echo results on the Figure 5.1 with the analytical model (in non-interacting spins approximation and with additional spins as free fitting parameters).

TABLE 5.1: Extracted ^{13}C spin couplings

Spin Number	1	2
A_{zz} (kHz)	-204.0(5)	51.5(5)
A_{zx} (kHz)	64.4(5)	143.6(5)

For the fitting, the Hamiltonian was represented in secular approximation and expressed as a tensor product of electron's eigenstates with N nuclear spins [118]:

$$H_i = |0\rangle\langle 0|\, \vec{\omega}_0^i \cdot \vec{I}_i + |\pm 1\rangle\langle \pm 1|\, \vec{\omega}_{\pm 1}^i \cdot \vec{I}_i \qquad (5.5)$$

The following analytical expression was used for the fit:

$$V(\tau) = \prod_{i=1}^{N} V_i(\tau) \qquad (5.6)$$

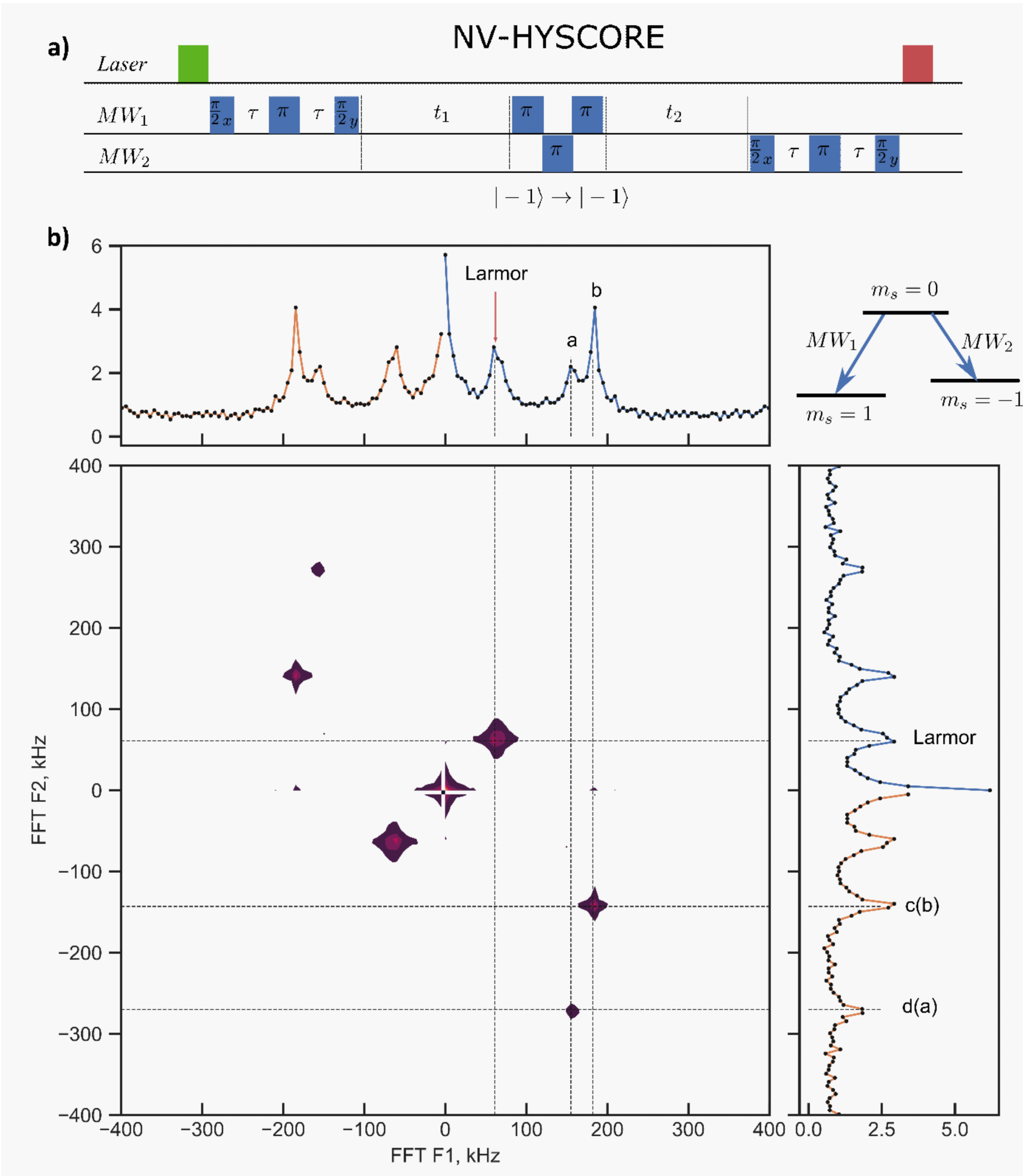

FIGURE 5.4: 2D correlation spectroscopy (HYSCORE) sequence performed with the NV center. a) Pulse sequence used for the experiment. b) 2D FFT of the obtained time-domain dataset. The peaks from the $|m_s = -1\rangle$ sublevel are clearly correlated with peaks from the $|m_s = +1\rangle$ electron sublevel. This correlation helps resolve the uncertainty in attributing spectral lines to individual nuclei, which was present in the 1D correlation measurements shown in Figure 5.3

Where V_i is given by:

$$V_i = V(0)\left[1 - 2\left(\frac{|\vec{\omega}_0^i \times \vec{\omega}_{\pm1}^i|}{|\vec{\omega}_0^i||\vec{\omega}_{\pm1}^i|}\right)^2 \sin^2\left(\frac{1}{2}|\vec{\omega}_0^i|\tau\right)\sin^2\left(\frac{1}{2}|\vec{\omega}_{\pm1}^i|\tau\right)\right] \tag{5.7}$$

The fit was run with a freedom to add another spins to the model as a free parameters with the initial guess $A_{zz} = A_{zx} = 1kHz$. The fit showed the best results with four additional ^{13}C spins with the couplings listed in Table 5.2.

TABLE 5.2: Fitted ^{13}C spin couplings

Spin Number	3	4	5	6
A_{zz} (kHz)	6(24)	49(31)	4(18)	76(1)
A_{zx} (kHz)	55(24)	101(28)	16(31)	1(2)

In this chapter, various methods were applied to identify the spin environment of the NV center. These approaches provided significant insights into the coupling and coherence properties of the surrounding spins. These results provide a valuable foundation for future applications, such as using these spins as long-term quantum memory or incorporating them into error correction schemes. The ability to accurately characterize and manipulate the spin environment enhances the potential of NV center applications.

Chapter 6

Spin Photon Entanglement results

This chapter presents the core experimental results, focusing on the entanglement of electron spin of the the NV center with the photon and also nuclear ^{14}N spin-photon systems. It outlines the protocols used to generate and measure these entangled states, starting with the initialization of the spins and progressing to the generation of spin-photon entanglement. The chapter includes detailed descriptions of the measurement techniques and data analysis procedures employed to evaluate the entanglement fidelity. The results highlight the successful implementation of these protocols and provide estimated fidelities for the generated entangled states.

6.1 Electron - Photon Entanglement

As a basis states of the NV qubit, the two electron levels of the ground state were used $|m_s = 0\rangle$ and $|m_s = -1\rangle$ - further in the text, they will be labeled as $|0\rangle$ and $|1\rangle$ respectively. For the photonic qubit, the time bin basis was chosen - $|Early\rangle$ (or $|E\rangle$) and $|Late\rangle$ ($|L\rangle$) [136][41], before the photon is generated, its state will be labeled as $|vaccum\rangle$ (or $|v\rangle$). The spin-photon entanglement generation protocol consists of three parts:

1. Electron spin initialization
2. Spin - photon entanglement generation
3. Measurement

6.1.1 Initialization

In the context of the spin-photon entanglement, the protocol must begin with the precise initialization of the involved spin states - the electron spin of the NV center and, for the cases of nuclear spin-photon entanglement, the nuclear spin of the ^{14}N nucleus. This is a basic requirement for the success of subsequent entanglement operations. The initialization procedure, detailed in other chapters of this thesis 2.2.1 and 3.3, ensures that both spins are prepared in well-defined quantum states. This step is vital as it sets the stage for the coherent manipulation of these states, allowing for the controlled generation of the entanglement between the spin and the photon. The ability to reliably initialize and manipulate spin states is fundamental to achieving high-fidelity entanglement, which is essential for practical applications in quantum communication and information processing.

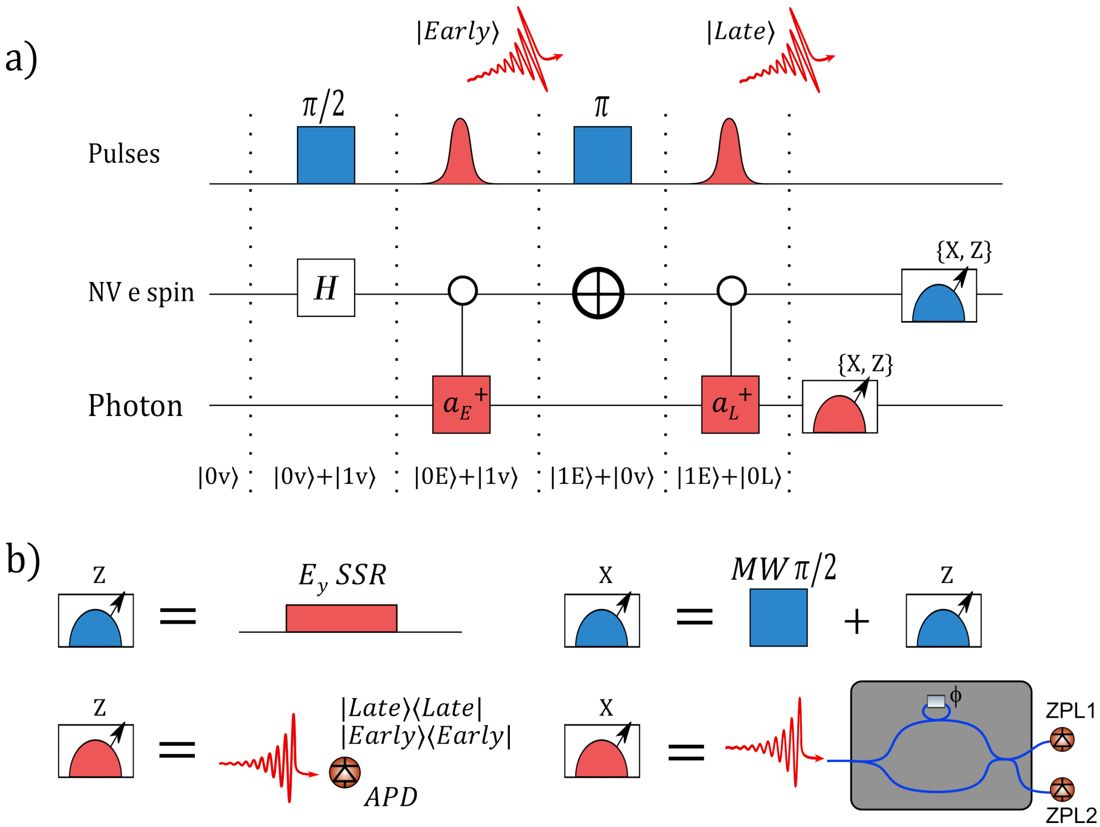

FIGURE 6.1: a) Quantum Circuit of the Entanglement Protocol. The top line represents the physical realization of gates, in the bottom line state of the system at each step is represented b) Experimental realization of Z, X readouts for electron NV spin (blue) and photonic qubit (red)

6.1.2 Electron spin - photon entanglement generation

Once the state of the NV center electron spin is initialized to $|m_s = 0\rangle$, the next step is creation of the equal superposition state:

$$|\Psi_1\rangle = \frac{1}{\sqrt{2}}\Big[|0\rangle + |1\rangle\Big] \otimes |v\rangle \tag{6.1}$$

Despite the Hadamard gate is a rotation of π around $(x+z)/\sqrt{2}$, the usual $pi/2$ Rabi rotation pulse can be called effective Hadamard gate because it does the same thing. Then, an optical π pulse is applied at the frequency of E_y transition. To remind - this transition is spin selective to $|0\rangle$, and happens between ground level $|0\rangle$ and the excited level $|E_y\rangle$, for electron state $|1\rangle$ the excitation will be off-resonant. So that, for $|0\rangle$ term of Equation 6.1, the NV center will go to E_y state of the excited level and then spontaneously decay back to $|0\rangle$, meanwhile emitting a photon in $|Early\rangle$ time mode - this can be considered this as the controlled $a_E^\dagger$ creation operator. So that, the state of the system will be:

$$|\Psi_2\rangle = \frac{1}{\sqrt{2}}\Big[|0, Early\rangle + |1, v\rangle\Big] \tag{6.2}$$

Then, a π pulse between basis states of NV qubit $|0\rangle \leftrightarrow |1\rangle$ swaps the respective states in Equation 6.2, bringing the system into the state:

$$|\Psi_3\rangle = \frac{1}{\sqrt{2}}\Big[|0, v\rangle + |1, Early\rangle\Big] \tag{6.3}$$

After this, a second optical π pulse is applied, and again it influences only $|0\rangle$ projection of NV spin qubit; the only difference is that now the photon is created in

$|Late\rangle$ mode and corresponding operator is controlled $a_L^\dagger$. The state of the system is

$$|\Psi_4\rangle = \frac{1}{\sqrt{2}}\Big[|0, Late\rangle + |1, Early\rangle\Big] \tag{6.4}$$

As can be seen, the state Equation 6.4 is entangled between the Z projection of NV center spin and the time bin of the photon.

6.1.3 Measurement

Now, it must be proven, that the correct Bell state was indeed generated. The formula to estimate the fidelity of the generated entangled state is given by[19][16]:

$$F \geq \frac{1}{2}(\rho_{22} + \rho_{33} - 2\sqrt{\rho_{11}\rho_{44}} + \tilde{\rho_{11}} + \tilde{\rho_{44}} - \tilde{\rho_{22}} - \tilde{\rho_{33}}) \tag{6.5}$$

where ρ_{ii} are the diagonal elements of the density matrix measured in S_zS_z basis and $\tilde{\rho_i}i$ are the diagonal elements of the density matrix measured in S_xS_x basis. So, what are those bases in the context of the experiment?

1. $\underline{S_zS_z}$
   It is easier to start with S_zS_z - these are probabilities to find the system in the basis states $|0, E\rangle$,$|0, L\rangle$,$|1, E\rangle$ and $|1, L\rangle$ - which is straightforward to measure. The arrival time of the photon to the detector needs to be measured first and then the state of NV center - by counting the number of detected photons when applying a readout pulse of low power resonant with E_y transition (see 2.2.2 and Figure 6.1 b).

2. $\underline{S_xS_x}$ The measurement in the S_xS_x is more complicated — the projection of each qubit on the Bloch sphere's $x|axis$ needs to be measured. To do this for the NV qubit, a $\pi/2$ pulse must be applied, mapping the $x - axis$ projection

to the $z - axis$, with the following S_z measurement, which was previously discussed. *It can be understood as a rotation of the Bloch Sphere itself by the $\pi/2$ angle.*

In the experiment, fidelity of the $|0\rangle$ state measurement is higher than for $|1\rangle$ - so experimentally it is more efficient to apply $\pm\pi/2$ pulses and always measure probability to be in the state $|0\rangle$, than to apply only $+\pi/2$ pulse and measure both probabilities $|0\rangle$ and $|1\rangle$

The photon qubit projection is measured via an unbalanced Mach-Zehnder interferometer (UMZI). It is important to follow all the intermediate states of the quantum system - the photon is routed to the interferometer, and the state of the system after it is

$$|\Psi_5\rangle = \frac{1}{2}\Big[|0, D_1\rangle + |0, D_2\rangle + e^{i\phi}|1, D_1\rangle - e^{i\phi}|1, D_1\rangle\Big] \tag{6.6}$$

Where D_1 and D_2 are spatial modes corresponding to the two different detectors (the interferometer redefines time modes to spatial modes). The minus sign before the last term appears due to the properties of the quantum beam splitter operator. Therefore, if the terms are regrouped:

$$|\Psi_5\rangle = \frac{1}{\sqrt{2}}|D_1\rangle \otimes \Big[|0\rangle + e^{i\phi}|1\rangle\Big] + \frac{1}{2}|D_2\rangle \otimes \Big[|0\rangle - e^{i\phi}|1\rangle\Big] \tag{6.7}$$

meaning that detection of the photon in the path, for example, D_1 projects the NV center onto the state

$$|\psi\rangle_{D_1} = \frac{1}{\sqrt{2}}(|0\rangle + e^{i\phi}|1\rangle) \tag{6.8}$$

and detection on the detector D_2, projects to the state

$$|\psi\rangle_{D_2} = \frac{1}{\sqrt{2}}(|0\rangle - e^{i\phi}|1\rangle) = \frac{1}{\sqrt{2}}(|0\rangle + e^{i(\phi+\pi)}|1\rangle) \tag{6.9}$$

it can be shown, that application of $\pi/2$ MW pulse to the NV center in such states gives the following probabilities for system state:

$$\begin{aligned} p(|0\rangle, D_1) &= \frac{1-\cos\phi}{4} \\ p(|1\rangle, D_1) &= \frac{1+\cos\phi}{4} \\ p(|0\rangle, D_2) &= \frac{1+\cos\phi}{4} \\ p(|1\rangle, D_2) &= \frac{1-\cos\phi}{4} \end{aligned} \tag{6.10}$$

In the experiment, the photon entangled with the NV center spin was created. The photon then acquired the phase on the interferometer, and in the end, this phase can be measured on the NV center, even though the NV center itself never experienced the phase directly.

In the actual experiments, one needs to consider different imperfections of the real-world equipment; for example, one must account for a small disbalance between coupling into the short and long arms of the interferometer. It is worth analyzing how this will change the Equations 6.10. For this, the following state of the system just before the second beam splitter can be considered.

$$|\Psi\rangle_0^{Real} = \alpha\,|0, Short\rangle + e^{i\phi}\beta\,|1, Long\rangle \tag{6.11}$$

where $\alpha^2 + \beta^2 = 1$ and ϕ is the phase acquired by the photon in the long arm of the interferometer. It can be shown that the state of the system after the second beam splitter is changed from Equation 6.7 to

$$|\Psi\rangle_1^{Real} = \frac{1}{\sqrt{2}} |D_1\rangle \left[\alpha |0\rangle + \beta e^{i\phi} |1\rangle\right] + \frac{1}{\sqrt{2}} |D_2\rangle \left[\alpha |0\rangle - \beta e^{i\phi} |1\rangle\right] \tag{6.12}$$

Consider, for example, the case that the photon was detected on $|D_1\rangle$, the application of the $\pi/2$ pulse to the NV spin (according to protocol) brings the NV center to the state:

$$|\Psi\rangle_2^{Real} \overset{|D_1\rangle}{=} e^{\frac{i\phi}{2}} |0\rangle \left[\alpha \cos\frac{\phi}{2} + \frac{\beta-\alpha}{2} e^{\frac{i\phi}{2}}\right] + e^{\frac{i\phi}{2}} |1\rangle \left[-\alpha i \sin\frac{\phi}{2} - \frac{\beta-\alpha}{2} e^{\frac{i\phi}{2}}\right] \tag{6.13}$$

here the assumption $\alpha < \beta$ was made. So the probability to find the NV center in state, for example $|0\rangle$, given that the photon was detected on the detector $|D_1\rangle$ is given by:

$$p(|0\rangle\, |D_1) = \alpha\beta \cos^2\frac{\phi}{2} + \left(\frac{\beta-\alpha}{2}\right)^2 \tag{6.14}$$

The contrast is usually calculated as:

$$\text{Contrast} = \frac{\text{Max} - \text{Min}}{\text{Max}} \tag{6.15}$$

Where Max and Min are the maximum and minimum values of the function. This yields for Equation 6.14:

$$\text{Contrast} = \frac{\alpha\beta}{\alpha\beta + \left(\frac{\beta-\alpha}{2}\right)^2} = \frac{\alpha\sqrt{1-\alpha^2}}{\alpha\sqrt{1-\alpha^2} + \left(\frac{\sqrt{1-\alpha^2}-\alpha}{2}\right)^2} \tag{6.16}$$

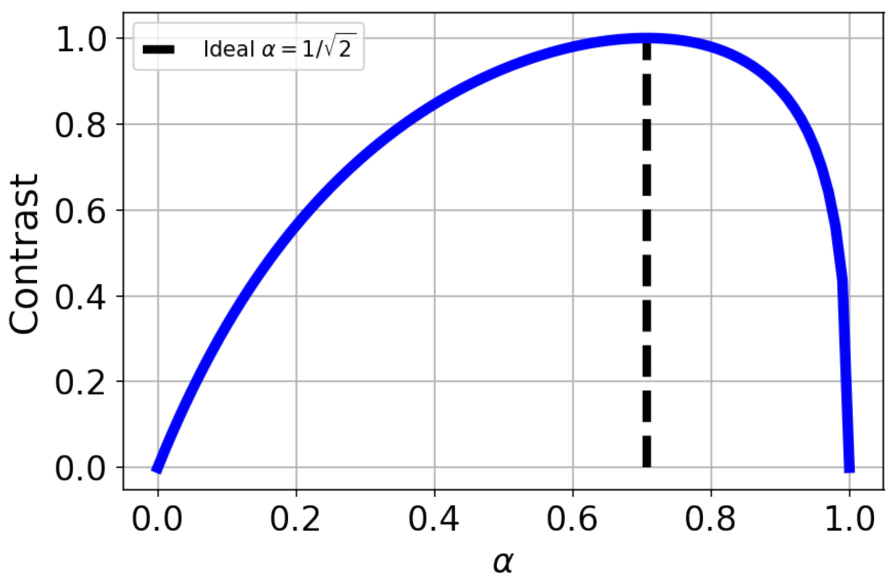

FIGURE 6.2: Interferometer misalignment effect. Dependence of the oscillation contrast vs degree of the initial state disproportion

6.1.4 Data Analysis

The experiment generates a significant amount of data, but not all is worth storing. This is mainly because of low collection efficiency and low probability of emitting in ZPL — which are of interest in spin photon entanglement. A flexible approach with two main parts is used to manage this: on-the-fly analysis and post-processing. **On-the-fly analysis** processes the data as it is produced, enabling a real-time evaluation and quick decisions about its relevance. As the data is received, preliminary algorithms check vital criteria for further examination to determine if it meets them. This immediate filtering ensures that only potentially significant data is retained for more detailed analysis, reducing the volume of data that needs long-term storage and focusing on the most promising results. Moreover, the data is stored in the format of raw time stamps, allowing a more flexible approach in further post-analysis. After the initial filtering, the selected data undergoes thorough **post-processing**. This stage employs more advanced and computationally intensive analysis techniques on the reduced dataset. Post-processing allows for fine-tuning the hyperparameters like the ZPL detection window, SSR detection window, SSR threshold, etc. This two-step approach optimizes data storage and enhances the efficiency and effectiveness of data analysis. Together, these methods create a robust system for handling large datasets, ensuring that important information is noticed while keeping data volumes manageable. This approach balances the need for thorough data analysis with practical storage and processing limitations.

To estimate the probabilities in the Equation 6.10 the method described in [136] was used:

$$P(|m_s = 0, 1\rangle, ZPL_i) = \frac{N_{ZPL_i \wedge |m_s=0,1\rangle}(\phi) - N_{BKG \wedge |m_s=0,1\rangle}(\phi)}{N_{ZPL_i}(\phi) - N_{BKG}(\phi)} \tag{6.17}$$

particularly, a number of different events were measured, and then the probability function was built out of it:

- $N_{ZPL_i \wedge |m_s=0,1\rangle}(\phi)$ - number of events as a function of the interferometer phase, when the ZPL photon was detected on the detector D_i (within **ZPL** detection window) and NV center was found in the state $|m_s = 0, 1\rangle$ (i.e during SSR the number of detected photon within SSR detection window was above certain SSR threshold)

- $N_{BKG \wedge |m_s=0,1\rangle}(\phi)$ - number of events as a function of the interferometer phase, when the ZPL photon was detected on the detector D_i (within **BACKGROUND** detection window) and NV center was found in state $|m_s = 0, 1\rangle$ (i.e during SSR the number of detected photon within SSR detection window was above certain SSR threshold)

- $N_{ZPL_i}(\phi)$ - number of events as a function of interferometer phase, when the ZPL photon was detected on the detector D_i (within **ZPL** detection window) and independent on NV center state at all

- $N_{BKG}(\phi)$ - number of events as a function of interferometer phase, when the ZPL photon was detected on the detector D_i (within **BACKGROUND** detection window) and independent on NV center state at all

As mentioned, the hyperparameters like ZPL and SSR detection windows and SSR threshold could be adjusted to find a balance between high fidelity and a manageable data acquisition rate.

6.1.5 Results

As mentioned, examining the spin-photon entanglement included the estimations in the ZZ and XX bases. So, using the measurements' results, the Fidelity of the

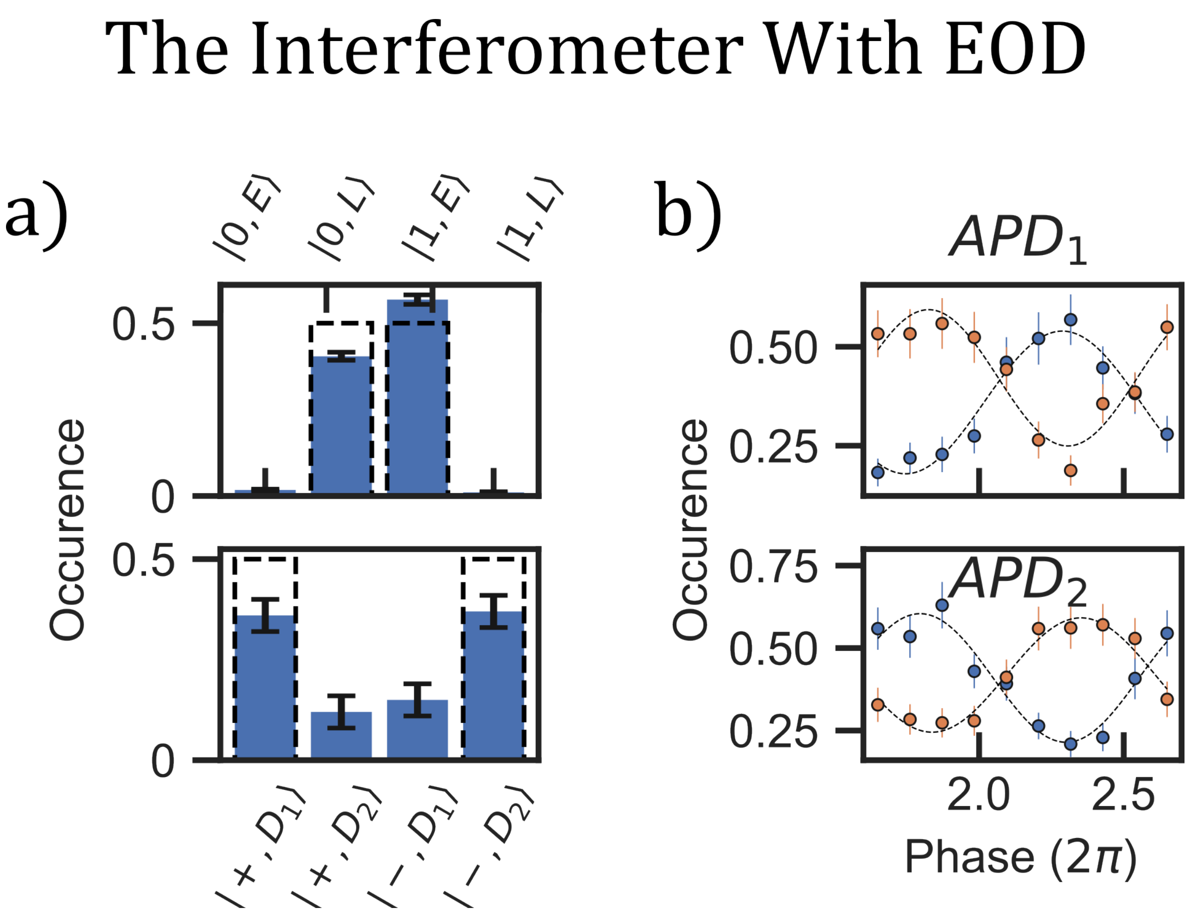

FIGURE 6.3: Electron Photon Entanglement with EOD a) Barplots reflect the probabilities to find the NV center and photon in different states, when measured in ZZ basis (top) or XX basis (bottom) b) Probability to find the NV center in state $|m_s = 0\rangle$ (blue) and $|m_s = \pm 1\rangle$ (orange) vs phase of the interferometer and given, that photon was detected on the first detector (top) or second (bottom).

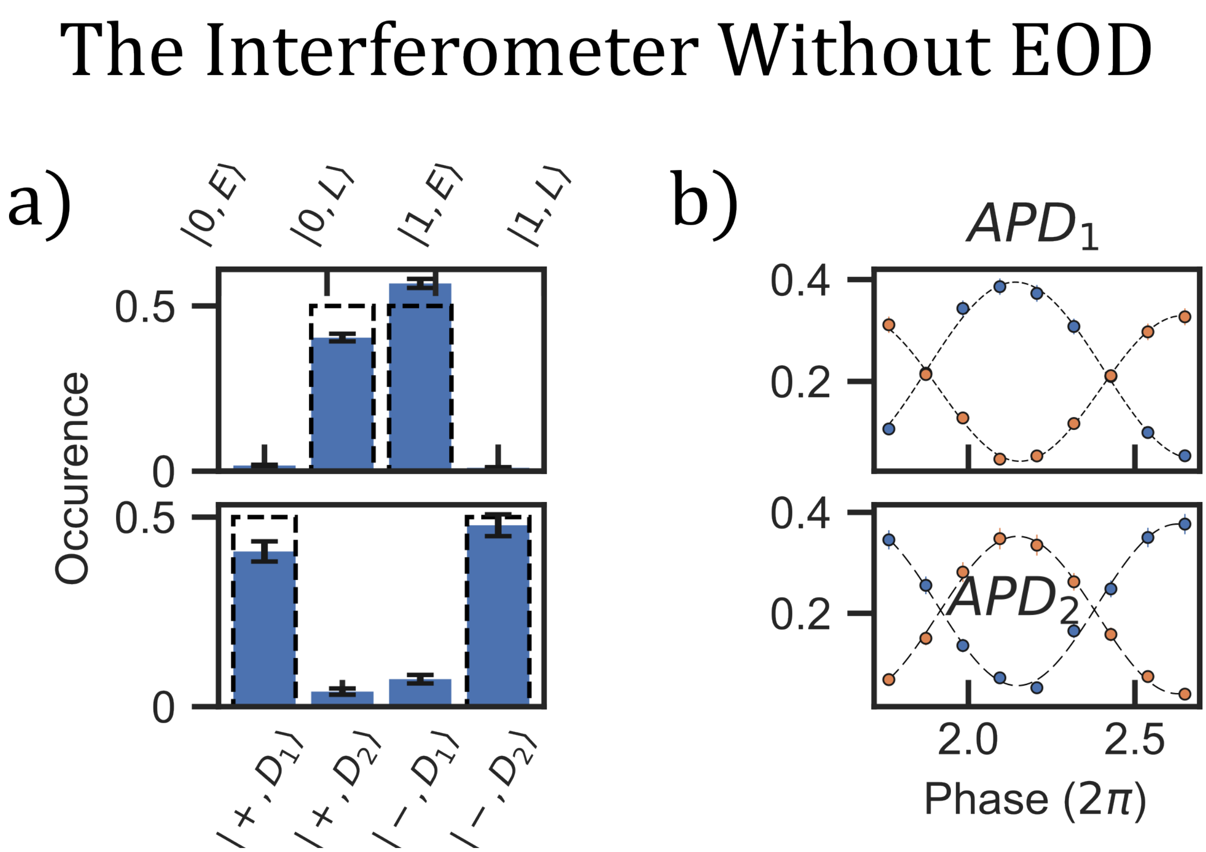

FIGURE 6.4: Electron Photon Entanglement without EOD a) Barplots reflect the probabilities to find the NV center and photon in the different states, when measured in ZZ basis (top) or XX basis (bottom) b) Probability to find the NV center in state $|m_s = 0\rangle$ (blue) and $|m_s = \pm 1\rangle$ (orange) vs phase of the interferometer and given, that photon was detected on the first detector (top) or second (bottom).

generated state can be estimated. The measurement on a ZZ basis is not phase-sensitive, so does not require the interferometer, therefore the resulting fidelity is not influenced by the factors associated with it (which are considered as a primary infidelity source for XX measurements). So, after the state Equation 6.4 was prepared, the photon detection time was measured with the following readout of the NV state. The probabilities of finding the system in one out of four possible states are shown as a bar plot on the picture 6.3 and on the top picture. With this, the fidelity for ZZ basis measurement of $F_{ZZ} = 0.95 \pm 0.02$ was obtained under the following hyperparameters - ZPL detection window of 25ns, SSR detection window of 3ns and SSR threshold of 3.

The XX experiment is way more complicated to perform because it is sensitive to the phase between two entangled states, so it requires the interferometer to introduce X-phase shift to the photon qubit. The XX measurement was done with two different Unbalanced Mach-Zehnder interferometers - one with a beam splitter at the input and another one with EOD (see 4.3). Following the Equations 6.10, one expects to see that the probability of detecting the NV center in its basis states oscillates with the phase of the interferometer and depends on which detector has clicked. This can be seen in Figures 6.4b and 6.3 b, where the blue lines correspond to $m_s = 0$ state and orange lines to the state $m_s = -1$. It can also be noticed that sinusoids with the same m_s states projection are in anti-phase with each other depending on the detector clicked. So, the phase obtained by the photon could be measured on the electron spin of the NV center. To get the measurement on a particularly XX basis, the interferometer was set to the point where the X phase is applied to the photon. Because it is way faster to measure one point instead of ten for the whole phase scan, the data acquisition for just X photon state rotation is way faster. This allows the application of more strict hyperparameter filters than in the case of a full-phase scan, increasing the measured state fidelity. The picture just in XX basis is shown as a bar plot on the Figures 6.4 and 6.3 a) in the bottom. With this, the following values were obtained:

- without EOD interferometer - $F_{XX} = 0.78 \pm 0.04$ (ZPL detection window is equal to 3 ns, SSR detection window of 3ns and SSR threshold of 3) and
- with EOD interferometer - $F_{XX} = 0.46 \pm 0.08$ (ZPL detection window of 5ns, SSR detection window of 15ns and SSR threshold of 0). This value was extracted from the fit of the full phase scan Figure 6.3 b.

The lower and more noisy values for the EOD interferometer could be explained by additional infidelity sources as an EOD alignment (which could also not be stable in time), and on top of this, smaller measurement time. Still, the fidelity level is well above the classical limit, allowing to claim the quantum entanglement [65]:

$$\boxed{\begin{aligned} &F \geq \frac{1}{2}(F_{ZZ} + F_{XX}) = \\ &= 0.70 \pm 0.08 \text{ (with EOD)} \\ &= 0.86 \pm 0.05 \text{ (without EOD)} \end{aligned}} \tag{6.18}$$

6.2 Nuclear- Photon Entanglement

To create the nuclear-photon entanglement, the electron spin of the NV center is used as an intermediate mediator. In this process, the electron spin first becomes entangled with a ^{14}N spin [97][148]. Then, a photon entangled with the electron spin is generated, resulting in the three qubits being entangled. It all starts with the initialization of the spins of the electron and nucleus into the $|00\rangle$ state and the subsequent application of a $\pi/2$ RF pulse to the nuclear spin, which transfers the

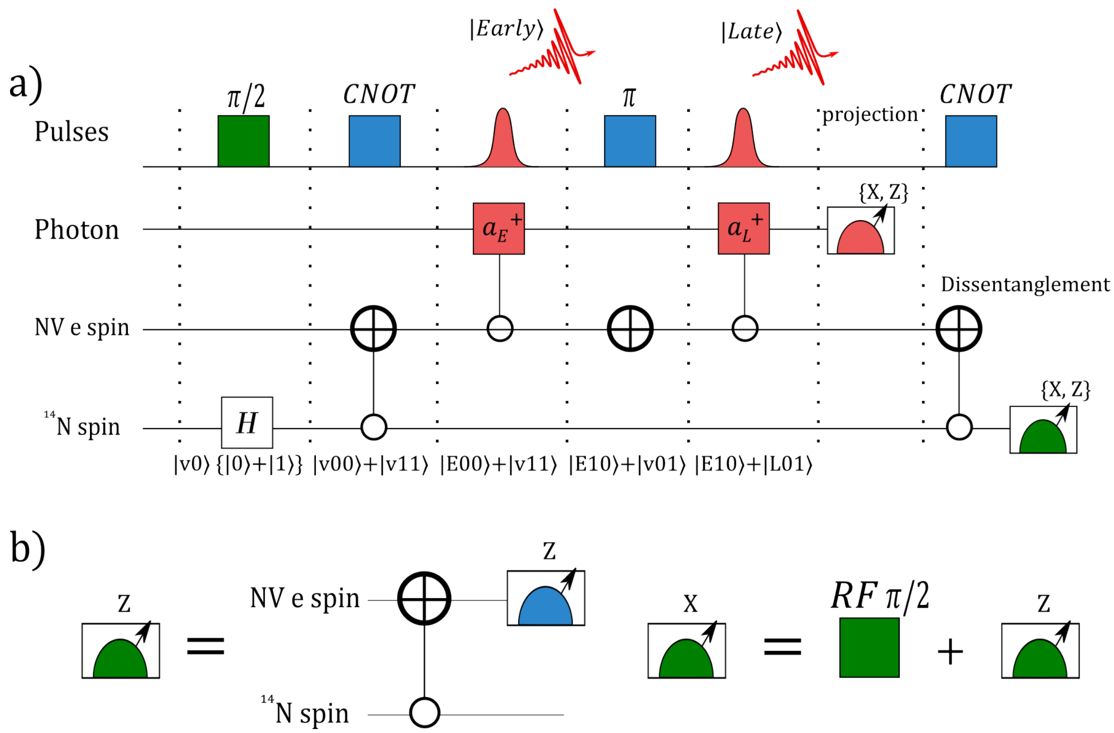

FIGURE 6.5: a) Quantum circuit of the nuclear spin - photon Entanglement protocol. The top line represents the physical realization of gates. Green - operation on ^{14}N spin, blue - on NV electron spin, in the bottom line, the state of the system at each step is represented. b) Experimental realization of Z, X readouts for nuclear ^{14}N spin

system into the state

$$\left|\Psi_1^N\right\rangle = \frac{1}{\sqrt{2}}\left|0\right\rangle \otimes \Big[\left|0\right\rangle + \left|1\right\rangle\Big] \otimes \left|v\right\rangle \tag{6.19}$$

and following CNOT gate on the electron spin entangles it with the nuclear one:

$$\left|\Psi_2^N\right\rangle = \frac{1}{\sqrt{2}}\Big[\left|00\right\rangle + \left|11\right\rangle\Big] \otimes \left|v\right\rangle \tag{6.20}$$

Then, the photon generation scheme repeats one from the previous section (Electron-Photon entanglement generation), bringing the system of three qubits into the state:

$$\left|\Psi_3^N\right\rangle = \frac{1}{\sqrt{2}}\Big[\left|01, Late\right\rangle + \left|10, Early\right\rangle\Big] \tag{6.21}$$

And after the interferometer, just before the photon detection:

$$\left|\Psi_4^N\right\rangle = \frac{1}{\sqrt{2}}\left|D_1\right\rangle \otimes \Big[\left|01\right\rangle + e^{i\phi}\left|10\right\rangle\Big] + \frac{1}{2}\left|D_2\right\rangle \otimes \Big[\left|01\right\rangle - e^{i\phi}\left|10\right\rangle\Big] \tag{6.22}$$

The coherence time of nuclear spin is much longer than that of the electron spin (which is often used as a good sensor). To store the phase acquired by the photon for a longer period, it is necessary to disentangle the electron spin from the nuclear spin by applying another CNOT gate, giving the state of the system, depending on the clicked detector :

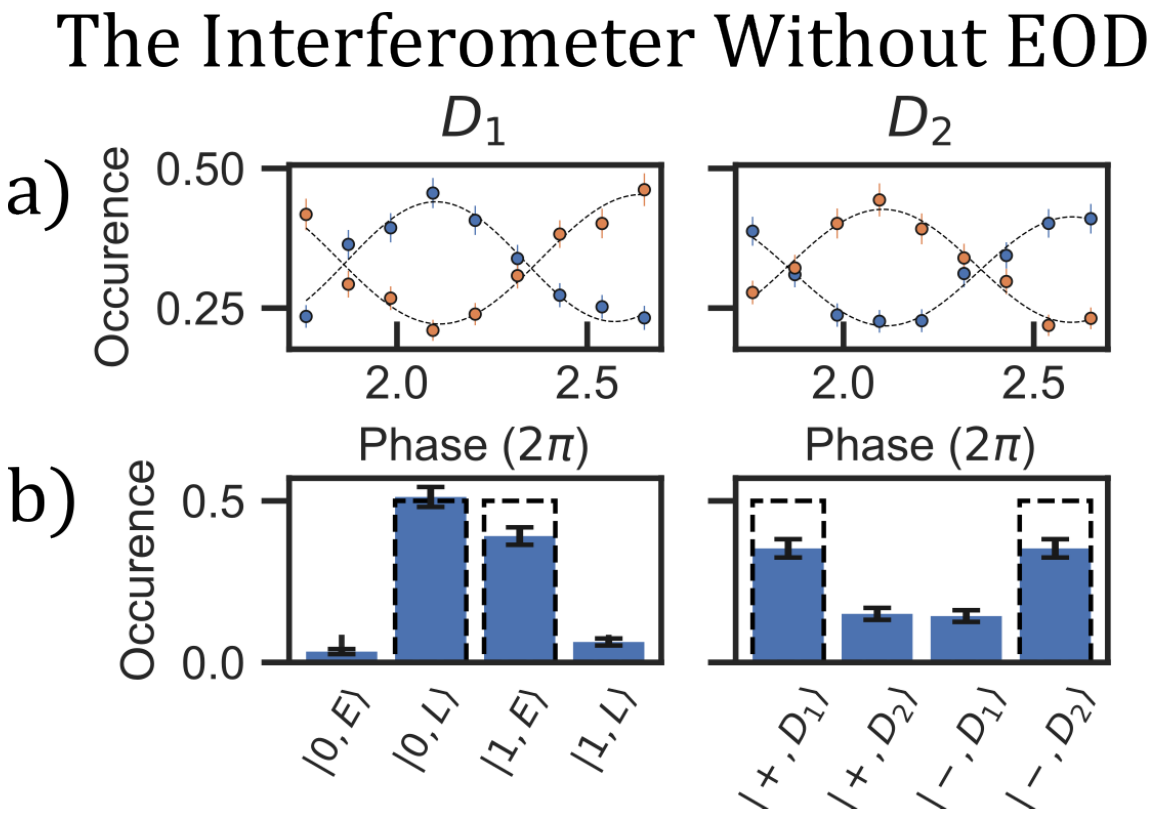

FIGURE 6.6: Nuclear Photon Entanglement without EOD a) Probability to find the NV center in state $|m_s = 0\rangle$ (blue) and $|m_s = \pm 1\rangle$ (orange) vs. phase of the interferometer and given, that photon was detected on the first detector (left) or second (right). b) Barplots reflect the probabilities to find the NV center and photon in different states,when measured in ZZ basis (left) or XX basis (right)

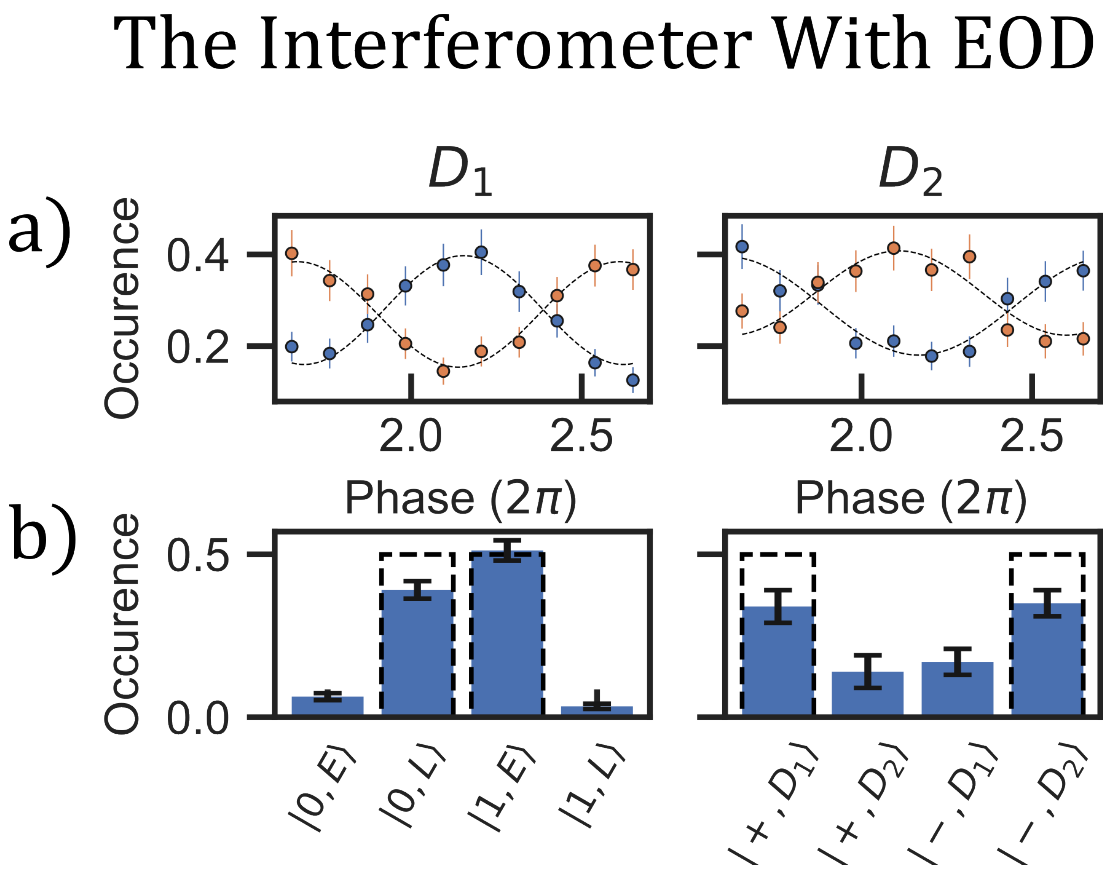

FIGURE 6.7: Nuclear Photon Entanglement with EOD a) Probability to find the NV center in state $|m_s = 0\rangle$ (blue) and $|m_s = \pm 1\rangle$ (orange) vs. phase of the interferometer and given, that photon was detected on the first detector (left) or second (right). b) Barplots reflect the probabilities to find the NV center and photon in different states,when measured in ZZ basis (left) or XX basis (right)

$$\begin{aligned} \left|\Psi_5^N\right\rangle_{D_1} =& \frac{1}{\sqrt{2}}\left|0\right\rangle \otimes \left[\left|1\right\rangle + e^{i\phi}\left|0\right\rangle\right] \\ \left|\Psi_5^N\right\rangle_{D_2} =& \frac{1}{\sqrt{2}}\left|0\right\rangle \otimes \left[\left|1\right\rangle - e^{i\phi}\left|0\right\rangle\right] \end{aligned} \tag{6.23}$$

Again, the phase acquired by the photon could be measured on the ^{14}N spin. It is essential to say that nuclear spin cannot in general be measured directly, and it is always done through mapping onto electron spin of the NV via CNOT gate, (see Figure 6.5 b).

The processing of the results for the nuclear spin photon entanglement is the same as that for the electron-photon entanglement case. The obtained value for ZZ measurement is $F_{ZZ} = 0.81 \pm 0.04$. The XX measurement was also done twice without and with the EOD type of interferometer, yielding the following results: 0.38 ± 0.09 with EOD and 0.42 ± 0.05 without EOD. So, the final values for the state fidelity[65]:

$$\boxed{\begin{aligned} &F \geq \frac{1}{2}(F_{ZZ} + F_{XX}) = \\ =&0.6 \pm 0.1 \text{ (with EOD)} \\ =&0.62 \pm 0.06 \text{ (without EOD)} \end{aligned}} \tag{6.24}$$

Chapter 7

Conclusion and Outlook

The experimental realization of the spin-photon entanglement interface is a fundamental unit of scalable quantum networks[17]. In this thesis, spin-photon entanglement with electron spin of the NV center and later with ^{14}N nuclear spin has successfully been demonstrated. The time-bin basis was chosen for the photon qubit because of its experimental robustness and practical applicability, making it a reliable choice for real-world implementations.

The NV center was used as an emitter of Zero Phonon Line photons (wavelength $\approx$ 637 nm) that are entangled with its electron spin. The generated state 7.1 was measured in ZZ and XX bases.

$$|\Psi\rangle = \frac{|0, Late\rangle + |1, Early\rangle}{\sqrt{2}} \tag{7.1}$$

Two unbalanced Mach-Zehnder Interferometers were made for the phase-sensitive XX measurements - standard one with a Beam Splitter at the input and with the Electro-Optical Deflector (EOD). The phase acquired by the photon in the interferometer was later measured at the NV center. The EOD approach is a novel technique utilizing photon guiding, which improves the efficiency of the photon basis redefinition from time-bin to spatial for phase-sensitive operations. This approach also opens new paths for integrating spin-photon interfaces into more complex quantum systems. The technique's ability to efficiently manage and manipulate photon states is expected to play a crucial role in developing advanced quantum communication protocols and quantum information processing applications. The resulting fidelity of the generated Bell state was estimated as $F \geq 0.7 \pm 0.08$ with EOD and $F \geq 0.86 \pm 0.05$ without EOD.

The primary achievement is the implementation of spin photon Entanglement with nuclear ^{14}N spin of the NV center. The nuclear spin has a longer coherence time ($\geq$ 100 ms was measured) but can't be accessed optically directly. So, the entangled state was generated via NV center electron spin as a mediator. The resulting fidelity of the nuclear spin-photon entangled state was estimated as $F \geq 0.6 \pm 0.1$ with EOD and $F \geq 0.62 \pm 0.06$ without EOD.

Moreover, initial steps have been taken to explore the use of even longer-lived ^{13}C spins, which hold promise for extending coherence times and further advancing quantum memory applications [137], for this initial characterization of the ^{13}C spin bath was made using Hahn Echo, XY-4 and HYSCORE techniques. Two coupled ^{13}C spins with the coupling strength A_{zz} of approximately 50 and -200 kHz were found. The strengths of four weakly coupled spins were also extracted from the measured data, which serve as a first guess for their detailed study.

Overall, the developed approach could also be applied to other "defect-like" platforms, such as T centers in silicon [62], V2 centers in 4H-SiC [60], rare-earth ions [75][103], or Group-IV defects [124][73]. These systems can potentially be integrated into a cavity [4][142][98], which naturally enhances the defect's characteristics, opens new possibilities for implementing quantum networks, and is a logical extension of the current research. This marks a significant advancement in the field of quantum information science.

This thesis adds a valuable contribution to the practical implementation of quantum technologies, offering new possibilities for the future development of scalable quantum networks.

Bibliography

[1] M. H. Abobeih, J. Cramer, M. A. Bakker, N. Kalb, M. Markham, D. J. Twitchen, and T. H. Taminiau. One-second coherence for a single electron spin coupled to a multi-qubit nuclear-spin environment. *Nature Communications*, 9(1):2552, Jun 2018.

[2] N Aslam, G Waldherr, P Neumann, F Jelezko, and J Wrachtrup. Photo-induced ionization dynamics of the nitrogen vacancy defect in diamond investigated by single-shot charge state detection. *New Journal of Physics*, 15(1):013064, jan 2013.

[3] Alain Aspect, Jean Dalibard, and Gérard Roger. Experimental test of bell's inequalities using time-varying analyzers. *Phys. Rev. Lett.*, 49:1804–1807, Dec 1982.

[4] Charles Babin, Rainer Stöhr, Naoya Morioka, Tobias Linkewitz, Timo Steidl, Raphael Wörnle, Di Liu, Erik Hesselmeier, Vadim Vorobyov, Andrej Denisenko, Mario Hentschel, Christian Gobert, Patrick Berwian, Georgy V. Astakhov, Wolfgang Knolle, Sridhar Majety, Pranta Saha, Marina Radulaski, Nguyen Tien Son, Jawad Ul-Hassan, Florian Kaiser, and Jörg Wrachtrup. Fabrication and nanophotonic waveguide integration of silicon carbide colour centres with preserved spin-optical coherence. *Nature Materials*, 21(1):67–73, Jan 2022.

[5] S. Baier, C. E. Bradley, T. Middelburg, V. V. Dobrovitski, T. H. Taminiau, and R. Hanson. Orbital and spin dynamics of single neutrally-charged nitrogen-vacancy centers in diamond. *Phys. Rev. Lett.*, 125:193601, Nov 2020.

[6] C. H. Baldwin, B. J. Bjork, J. P. Gaebler, D. Hayes, and D. Stack. Subspace benchmarking high-fidelity entangling operations with trapped ions. *Phys. Rev. Res.*, 2:013317, Mar 2020.

[7] N. Bar-Gill, L. M. Pham, A. Jarmola, D. Budker, and R. L. Walsworth. Solid-state electronic spin coherence time approaching one second. *Nature Communications*, 4(1):1743, Apr 2013.

[8] A. Batalov, V. Jacques, F. Kaiser, P. Siyushev, P. Neumann, L. J. Rogers, R. L. McMurtrie, N. B. Manson, F. Jelezko, and J. Wrachtrup. Low temperature studies of the excited-state structure of negatively charged nitrogen-vacancy color centers in diamond. *Phys. Rev. Lett.*, 102:195506, May 2009.

[9] K. Beha, A. Batalov, N. B. Manson, R. Bratschitsch, and A. Leitenstorfer. Optimum photoluminescence excitation and recharging cycle of single nitrogen-vacancy centers in ultrapure diamond. *Phys. Rev. Lett.*, 109:097404, Aug 2012.

[10] J. S. Bell. On the einstein podolsky rosen paradox. *Physics Physique Fizika*, 1:195–200, Nov 1964.

[11] J. S. Bell. La nouvelle cuisine. In John Stewart Bell, editor, *Speakable and unspeakable in quantum mechanics: collected papers on quantum philosophy*, pages 232–248. Cambridge University Press, 1987.

[12] J. S. Bell and Alain Aspect. *Speakable and Unspeakable in Quantum Mechanics: Collected Papers on Quantum Philosophy.* Cambridge University Press, 2 edition, 2004.

[13] JOHN S. BELL. On the problem of hidden variables in quantum mechanics. *Rev. Mod. Phys.*, 38:447–452, Jul 1966.

[14] Charles H. Bennett and Gilles Brassard. Quantum cryptography: Public key distribution and coin tossing. *Theoretical Computer Science*, 560:7–11, 2014. Theoretical Aspects of Quantum Cryptography – celebrating 30 years of BB84.

[15] Charles H. Bennett, Gilles Brassard, Claude Crépeau, Richard Jozsa, Asher Peres, and William K. Wootters. Teleporting an unknown quantum state via dual classical and einstein-podolsky-rosen channels. *Phys. Rev. Lett.*, 70:1895–1899, Mar 1993.

[16] H. Bernien, B. Hensen, W. Pfaff, G. Koolstra, M. S. Blok, L. Robledo, T. H. Taminiau, M. Markham, D. J. Twitchen, L. Childress, and R. Hanson. Heralded entanglement between solid-state qubits separated by three metres. *Nature*, 497(7447):86–90, May 2013.

[17] Eric Bersin, Madison Sutula, Yan Qi Huan, Aziza Suleymanzade, Daniel R. Assumpcao, Yan-Cheng Wei, Pieter-Jan Stas, Can M. Knaut, Erik N. Knall, Carsten Langrock, Neil Sinclair, Ryan Murphy, Ralf Riedinger, Matthew Yeh, C.J. Xin, Saumil Bandyopadhyay, Denis D. Sukachev, Bartholomeus Machielse, David S. Levonian, Mihir K. Bhaskar, Scott Hamilton, Hongkun Park, Marko Lončar, Martin M. Fejer, P. Benjamin Dixon, Dirk R. Englund, and Mikhail D. Lukin. Telecom networking with a diamond quantum memory. *PRX Quantum*, 5:010303, Jan 2024.

[18] Hans K.C. Beukers, Matteo Pasini, Hyeongrak Choi, Dirk Englund, Ronald Hanson, and Johannes Borregaard. Remote-entanglement protocols for stationary qubits with photonic interfaces. *PRX Quantum*, 5:010202, Mar 2024.

[19] B. B. Blinov, D. L. Moehring, L.-. M. Duan, and C. Monroe. Observation of entanglement between a single trapped atom and a single photon. *Nature*, 428(6979):153–157, Mar 2004.

[20] D. Bohm and Y. Aharonov. Discussion of experimental proof for the paradox of einstein, rosen, and podolsky. *Phys. Rev.*, 108:1070–1076, Nov 1957.

[21] Dik Bouwmeester, Jian-Wei Pan, Klaus Mattle, Manfred Eibl, Harald Weinfurter, and Anton Zeilinger. Experimental quantum teleportation. *Nature*, 390(6660):575–579, Dec 1997.

[22] Thomas K. Bracht, Florian Kappe, Moritz Cygorek, Tim Seidelmann, Yusuf Karli, Vikas Remesh, Gregor Weihs, Vollrath Martin Axt, and Doris E. Reiter. Theory of time-bin entangled photons from quantum emitters, 2024.

[23] C. E. Bradley, J. Randall, M. H. Abobeih, R. C. Berrevoets, M. J. Degen, M. A. Bakker, M. Markham, D. J. Twitchen, and T. H. Taminiau. A ten-qubit solid-state spin register with quantum memory up to one minute. *Phys. Rev. X*, 9:031045, Sep 2019.

[24] Anne Broadbent, Joseph Fitzsimons, and Elham Kashefi. Universal blind quantum computation. In *2009 50th Annual IEEE Symposium on Foundations of Computer Science*, pages 517–526, 2009.

[25] Nicolas Brunner, Daniel Cavalcanti, Stefano Pironio, Valerio Scarani, and Stephanie Wehner. Bell nonlocality. *Rev. Mod. Phys.*, 86:419–478, Apr 2014.

[26] Dominik B. Bucher, David R. Glenn, Hongkun Park, Mikhail D. Lukin, and Ronald L. Walsworth. Hyperpolarization-enhanced nmr spectroscopy with femtomole sensitivity using quantum defects in diamond. *Phys. Rev. X*, 10:021053, Jun 2020.

[27] L. Childress, M. V. Gurudev Dutt, J. M. Taylor, A. S. Zibrov, F. Jelezko, J. Wrachtrup, P. R. Hemmer, and M. D. Lukin. Coherent dynamics of coupled electron and nuclear spin qubits in diamond. *Science*, 314(5797):281–285, 2006.

[28] Yiwen Chu and Mikhail D. Lukin. Quantum optics with nitrogen-vacancy centers in diamond, 2015.

[29] John F. Clauser, Michael A. Horne, Abner Shimony, and Richard A. Holt. Proposed experiment to test local hidden-variable theories. *Phys. Rev. Lett.*, 23:880–884, Oct 1969.

[30] Severin Daiss, Stefan Langenfeld, Stephan Welte, Emanuele Distante, Philip Thomas, Lukas Hartung, Olivier Morin, and Gerhard Rempe. A quantum-logic gate between distant quantum-network modules. *Science*, 371(6529):614–617, 2021.

[31] B. D'Anjou and W. A. Coish. Optimal post-processing for a generic single-shot qubit readout. *Phys. Rev. A*, 89:012313, Jan 2014.

[32] G Davies. Dynamic jahn-teller distortions at trigonal optical centres in diamond. *Journal of Physics C: Solid State Physics*, 12(13):2551, jul 1979.

[33] C. L. Degen, F. Reinhard, and P. Cappellaro. Quantum sensing. *Rev. Mod. Phys.*, 89:035002, Jul 2017.

[34] D. Dieks. Communication by epr devices. *Physics Letters A*, 92(6):271–272, 1982.

[35] David P. DiVincenzo. The physical implementation of quantum computation. *Fortschritte der Physik*, 48(9-11):771–783, 2000.

[36] Marcus W. Doherty, Neil B. Manson, Paul Delaney, Fedor Jelezko, Jörg Wrachtrup, and Lloyd C.L. Hollenberg. The nitrogen-vacancy colour centre in diamond. *Physics Reports*, 528(1):1–45, 2013. The nitrogen-vacancy colour centre in diamond.

[37] F. Dolde, H. Fedder, M. W. Doherty, T. Nöbauer, F. Rempp, G. Balasubramanian, T. Wolf, F. Reinhard, L. C. L. Hollenberg, F. Jelezko, and J. Wrachtrup. Electric-field sensing using single diamond spins. *Nature Physics*, 7(6):459–463, Jun 2011.

[38] F. Dolde, I. Jakobi, B. Naydenov, N. Zhao, S. Pezzagna, C. Trautmann, J. Meijer, P. Neumann, F. Jelezko, and J. Wrachtrup. Room-temperature entanglement between single defect spins in diamond. *Nature Physics*, 9(3):139–143, Mar 2013.

[39] Florian Dolde, Ville Bergholm, Ya Wang, Ingmar Jakobi, Boris Naydenov, Sébastien Pezzagna, Jan Meijer, Fedor Jelezko, Philipp Neumann, Thomas Schulte-Herbrüggen, Jacob Biamonte, and Jörg Wrachtrup. High-fidelity spin entanglement using optimal control. *Nature Communications*, 5(1):3371, Feb 2014.

[40] A. Dréau, M. Lesik, L. Rondin, P. Spinicelli, O. Arcizet, J.-F. Roch, and V. Jacques. Avoiding power broadening in optically detected magnetic resonance of single nv defects for enhanced dc magnetic field sensitivity. *Phys. Rev. B*, 84:195204, Nov 2011.

[41] Anaïs Dréau, Anna Tchebotareva, Aboubakr El Mahdaoui, Cristian Bonato, and Ronald Hanson. Quantum frequency conversion of single photons from a nitrogen-vacancy center in diamond to telecommunication wavelengths. *Phys. Rev. Appl.*, 9:064031, Jun 2018.

[42] L.-M. Duan and H. J. Kimble. Efficient engineering of multiatom entanglement through single-photon detections. *Phys. Rev. Lett.*, 90:253601, Jun 2003.

[43] A. Einstein, B. Podolsky, and N. Rosen. Can quantum-mechanical description of physical reality be considered complete? *Phys. Rev.*, 47:777–780, May 1935.

[44] A. Einstein, K. Przibram, and M.J. Klein. *Letters on Wave Mechanics: Correspondence with H. A. Lorentz, Max Planck, and Erwin Schrödinger*. Philosophical Library/Open Road, 2011.

[45] Xun-Li Feng, Zhi-Ming Zhang, Xiang-Dong Li, Shang-Qing Gong, and Zhi-Zhan Xu. Entangling distant atoms by interference of polarized photons. *Phys. Rev. Lett.*, 90:217902, May 2003.

[46] Regina Finsterhoelzl, Wolf-Rüdiger Hannes, and Guido Burkard. High-fidelity entangling gates for electron and nuclear spin qubits in diamond, 2024.

[47] Stuart J. Freedman and John F. Clauser. Experimental test of local hidden-variable theories. *Phys. Rev. Lett.*, 28:938–941, Apr 1972.

[48] T. Gaebel, M. Domhan, C. Wittmann, I. Popa, F. Jelezko, J. Rabeau, A. Greentree, S. Prawer, E. Trajkov, P. R. Hemmer, and J. Wrachtrup. Photochromism in single nitrogen-vacancy defect in diamond. *Applied Physics B*, 82(2):243–246, Feb 2006.

[49] Jay Gambetta, W. A. Braff, A. Wallraff, S. M. Girvin, and R. J. Schoelkopf. Protocols for optimal readout of qubits using a continuous quantum nondemolition measurement. *Phys. Rev. A*, 76:012325, Jul 2007.

[50] Jianpei Geng, Tetyana Shalomayeva, Mariia Gryzlova, Amlan Mukherjee, Santo Santonocito, Dzhavid Dzhavadzade, Durga Bhaktavatsala Rao Dasari,

Hiromitsu Kato, Rainer Stöhr, Andrej Denisenko, Norikazu Mizuochi, and Jörg Wrachtrup. Dopant-assisted stabilization of negatively charged single nitrogen-vacancy centers in phosphorus-doped diamond at low temperatures. *npj Quantum Information*, 9(1):110, Oct 2023.

[51] M. L. Goldman, T. L. Patti, D. Levonian, S. F. Yelin, and M. D. Lukin. Optical control of a single nuclear spin in the solid state. *Phys. Rev. Lett.*, 124:153203, Apr 2020.

[52] Daniel Gottesman, Thomas Jennewein, and Sarah Croke. Longer-baseline telescopes using quantum repeaters. *Phys. Rev. Lett.*, 109:070503, Aug 2012.

[53] Simon Gröblacher, Tomasz Paterek, Rainer Kaltenbaek, Caslav Brukner, Marek Zukowski, Markus Aspelmeyer, and Anton Zeilinger. An experimental test of non-local realism. *Nature*, 446(7138):871–875, 2007. DOI: 10.1038/nature05677 Coden: NATUA Affiliations: Faculty of Physics, University of Vienna, Boltzmanngasse 5, A-1090 Vienna, Austria; Institute for Quantum Optics and Quantum Information (IQOQI), Austrian Academy of Sciences, Boltzmanngasse 3, A-1090 Vienna, Austria; Institute of Theoretical Physics and Astrophysics, University of Gdansk, ul. Wita Stwosza 57, PL-08-952 Gdansk, Poland; Erwin Schrödinger International Institute for Mathematical Physics (ESI), Boltzmanngasse 9, A-1090 Vienna, Austria Adressen: Aspelmeyer, M.; Faculty of Physics; University of Vienna; Boltzmanngasse 5 A-1090 Vienna, Austria; email: markus.aspelmeyer@quantum.at Source-File: PhysicsScopus200208.csv Import aus Scopus: 2-s2.0-34247361229 Importdatum: 21.02.2008 15:52:23 25.02.2008: Datenanforderung 2152 (Import Sachbearbeiter).

[54] A. Gruber, A. Dräbenstedt, C. Tietz, L. Fleury, J. Wrachtrup, and C. von Borczyskowski. Scanning confocal optical microscopy and magnetic resonance on single defect centers. *Science*, 276(5321):2012–2014, 1997.

[55] E. L. Hahn. Spin echoes. *Phys. Rev.*, 80:580–594, Nov 1950.

[56] Xing-Fei He, Neil B. Manson, and Peter T. H. Fisk. Paramagnetic resonance of photoexcited n-v defects in diamond. ii. hyperfine interaction with the ^{14}N nucleus. *Phys. Rev. B*, 47:8816–8822, Apr 1993.

[57] B. Hensen, H. Bernien, A. E. Dréau, A. Reiserer, N. Kalb, M. S. Blok, J. Ruitenberg, R. F. L. Vermeulen, R. N. Schouten, C. AbellÃ¡n, W. Amaya, V. Pruneri, M. W. Mitchell, M. Markham, D. J. Twitchen, D. Elkouss, S. Wehner, T. H. Taminiau, and R. Hanson. Loophole-free bell inequality violation using electron spins separated by 1.3 kilometres. *Nature*, 526(7575):682–686, Oct 2015.

[58] S. L. N. Hermans, M. Pompili, H. K. C. Beukers, S. Baier, J. Borregaard, and R. Hanson. Qubit teleportation between non-neighbouring nodes in a quantum network. *Nature*, 605(7911):663–668, May 2022.

[59] F. Herzog, K. Kudielka, D. Erni, and W. Bachtold. Optical phase locking by local oscillator phase dithering. *IEEE Journal of Quantum Electronics*, 42(10):973–985, 2006.

[60] Erik Hesselmeier, Pierre Kuna, Wolfgang Knolle, Florian Kaiser, Nguyen Tien Son, Misagh Ghezellou, Jawad Ul-Hassan, Vadim Vorobyov, and Jörg Wrachtrup. High-fidelity optical readout of a nuclear-spin qubit in silicon carbide. *Phys. Rev. Lett.*, 132:180804, May 2024.

[61] M. Żukowski, A. Zeilinger, M. A. Horne, and A. K. Ekert. "event-ready-detectors" bell experiment via entanglement swapping. *Phys. Rev. Lett.*, 71:4287–4290, Dec 1993.

[62] Photonic Inc, :, Francis Afzal, Mohsen Akhlaghi, Stefanie J. Beale, Olinka Bedroya, Kristin Bell, Laurent Bergeron, Kent Bonsma-Fisher, Polina Bychkova, Zachary M. E. Chaisson, Camille Chartrand, Chloe Clear, Adam Darcie, Adam DeAbreu, Colby DeLisle, Lesley A. Duncan, Chad Dundas Smith, John Dunn, Amir Ebrahimi, Nathan Evetts, Daker Fernandes Pinheiro, Patricio Fuentes, Tristen Georgiou, Biswarup Guha, Rafael Haenel, Daniel Higginbottom, Daniel M. Jackson, Navid Jahed, Amin Khorshidahmad, Prasoon K. Shandilya, Alexander T. K. Kurkjian, Nikolai Lauk, Nicholas R. Lee-Hone, Eric Lin, Rostyslav Litynskyy, Duncan Lock, Lisa Ma, Iain MacGilp, Evan R. MacQuarrie, Aaron Mar, Alireza Marefat Khah, Alex Matiash, Evan Meyer-Scott, Cathryn P. Michaels, Juliana Motira, Narwan Kabir Noori, Egor Ospadov, Ekta Patel, Alexander Patscheider, Danny Paulson, Ariel Petruk, Adarsh L. Ravindranath, Bogdan Reznychenko, Myles Ruether, Jeremy Ruscica, Kunal Saxena, Zachary Schaller, Alex Seidlitz, John Senger, Youn Seok Lee, Orbel Sevoyan, Stephanie Simmons, Oney Soykal, Leea Stott, Quyen Tran, Spyros Tserkis, Ata Ulhaq, Wyatt Vine, Russ Weeks, Gary Wolfowicz, and Isao Yoneda. Distributed quantum computing in silicon, 2024.

[63] P. Jamonneau, M. Lesik, J. P. Tetienne, I. Alvizu, L. Mayer, A. Dréau, S. Kosen, J.-F. Roch, S. Pezzagna, J. Meijer, T. Teraji, Y. Kubo, P. Bertet, J. R. Maze, and V. Jacques. Competition between electric field and magnetic field noise in the decoherence of a single spin in diamond. *Phys. Rev. B*, 93:024305, Jan 2016.

[64] A. Jarmola, V. M. Acosta, K. Jensen, S. Chemerisov, and D. Budker. Temperature- and magnetic-field-dependent longitudinal spin relaxation in nitrogen-vacancy ensembles in diamond. *Phys. Rev. Lett.*, 108:197601, May 2012.

[65] Javid Javadzade, Majid Zahedian, Florian Kaiser, Vadim Vorobyov, and Jörg Wrachtrup. Efficient nuclear spin - photon entanglement with optical routing, 2024.

[66] F. Jelezko, T. Gaebel, I. Popa, M. Domhan, A. Gruber, and J. Wrachtrup. Observation of coherent oscillation of a single nuclear spin and realization of a two-qubit conditional quantum gate. *Phys. Rev. Lett.*, 93:130501, Sep 2004.

[67] F. Jelezko and J. Wrachtrup. Single defect centres in diamond: A review. *physica status solidi (a)*, 203(13):3207–3225, 2006.

[68] Cody Jones, Kristiaan De Greve, and Yoshihisa Yamamoto. A high-speed optical link to entangle quantum dots, 2013.

[69] Cody Jones, Danny Kim, Matthew T Rakher, Paul G Kwiat, and Thaddeus D Ladd. Design and analysis of communication protocols for quantum repeater networks. *New Journal of Physics*, 18(8):083015, aug 2016.

[70] Richard Jozsa. Fidelity for mixed quantum states. *Journal of Modern Optics*, 41(12):2315–2323, 1994.

[71] F. Kaiser, V. Jacques, A. Batalov, P. Siyushev, F. Jelezko, and J. Wrachtrup. Polarization properties of single photons emitted by nitrogen-vacancy defect in diamond at low temperature, 2009.

[72] F. Kaiser, V. Jacques, A. Batalov, P. Siyushev, F. Jelezko, and J. Wrachtrup. Polarization properties of single photons emitted by nitrogen-vacancy defect in diamond at low temperature, 2009.

[73] Ioannis Karapatzakis, Jeremias Resch, Marcel Schrodin, Philipp Fuchs, Michael Kieschnick, Julia Heupel, Luis Kussi, Christoph Sürgers, Cyril Popov, Jan Meijer, Christoph Becher, Wolfgang Wernsdorfer, and David Hunger. Microwave control of the tin-vacancy spin qubit in diamond with a superconducting waveguide, 2024.

[74] H. J. Kimble. The quantum internet. *Nature*, 453(7198):1023–1030, Jun 2008.

[75] Adam Kinos, David Hunger, Roman Kolesov, Klaus Molmer, Hugues de Riedmatten, Philippe Goldner, Alexandre Tallaire, Loic Morvan, Perrine Berger, Sacha Welinski, Khaled Karrai, Lars Rippe, Stefan Kröll, and Andreas Walther. Roadmap for rare-earth quantum computing, 2021.

[76] P. Komar, E. M. Kessler, M. Bishof, L. Jiang, A. S. Sorensen, J. Ye, and M. D. Lukin. A quantum network of clocks. *Nature Physics*, 10(8):582–587, Aug 2014.

[77] Andreas V. Kuhlmann, Julien Houel, Daniel Brunner, Arne Ludwig, Dirk Reuter, Andreas D. Wieck, and Richard J. Warburton. A dark-field microscope for background-free detection of resonance fluorescence from single semiconductor quantum dots operating in a set-and-forget mode. *Review of Scientific Instruments*, 84(7):073905, 07 2013.

[78] Karl F. Kuhlmann, David M. Grant, and Robin K. Harris. Nuclear Overhauser Effects and 13C Relaxation Times in 13C-{H} Double Resonance Spectra. *The Journal of Chemical Physics*, 52(7):3439–3448, 04 1970.

[79] P. G. Kwiat, A. M. Steinberg, and R. Y. Chiao. High-visibility interference in a bell-inequality experiment for energy and time. *Phys. Rev. A*, 47:R2472–R2475, Apr 1993.

[80] J. Larmor. Lxiii. on the theory of the magnetic influence on spectra; and on the radiation from moving ions. *The London, Edinburgh, and Dublin Philosophical Magazine and Journal of Science*, 44(271):503–512, 1897.

[81] A. Lenef and S. C. Rand. Electronic structure of the n-v center in diamond: Theory. *Phys. Rev. B*, 53:13441–13455, May 1996.

[82] D. S. Levonian, R. Riedinger, B. Machielse, E. N. Knall, M. K. Bhaskar, C. M. Knaut, R. Bekenstein, H. Park, M. Lončar, and M. D. Lukin. Optical entanglement of distinguishable quantum emitters. *Phys. Rev. Lett.*, 128:213602, May 2022.

[83] J H N Loubser and J A van Wyk. Electron spin resonance in the study of diamond. *Reports on Progress in Physics*, 41(8):1201, aug 1978.

[84] D. Luong, L. Jiang, J. Kim, and N. Lütkenhaus. Overcoming lossy channel bounds using a single quantum repeater node. *Applied Physics B*, 122(4):96, Apr 2016.

[85] Lars S. Madsen, Fabian Laudenbach, Mohsen Falamarzi. Askarani, Fabien Rortais, Trevor Vincent, Jacob F. F. Bulmer, Filippo M. Miatto, Leonhard Neuhaus, Lukas G. Helt, Matthew J. Collins, Adriana E. Lita, Thomas Gerrits, Sae Woo Nam, Varun D. Vaidya, Matteo Menotti, Ish Dhand, Zachary Vernon, Nicolás Quesada, and Jonathan Lavoie. Quantum computational advantage with a programmable photonic processor. *Nature*, 606(7912):75–81, Jun 2022.

[86] N.B. Manson and J.P. Harrison. Photo-ionization of the nitrogen-vacancy center in diamond. *Diamond and Related Materials*, 14(10):1705–1710, 2005.

[87] J R Maze, A Gali, E Togan, Y Chu, A Trifonov, E Kaxiras, and M D Lukin. Properties of nitrogen-vacancy centers in diamond: the group theoretic approach. *New Journal of Physics*, 13(2):025025, feb 2011.

[88] S. Meiboom and D. Gill. Modified Spin-Echo Method for Measuring Nuclear Relaxation Times. *Review of Scientific Instruments*, 29(8):688–691, 08 1958.

[89] C. Monroe, D. M. Meekhof, B. E. King, W. M. Itano, and D. J. Wineland. Demonstration of a fundamental quantum logic gate. *Phys. Rev. Lett.*, 75:4714–4717, Dec 1995.

[90] Naoya Morioka, Charles Babin, Roland Nagy, Izel Gediz, Erik Hesselmeier, Di Liu, Matthew Joliffe, Matthias Niethammer, Durga Dasari, Vadim Vorobyov, Roman Kolesov, Rainer Stöhr, Jawad Ul-Hassan, Nguyen Tien Son, Takeshi Ohshima, Péter Udvarhelyi, Gergő Thiering, Adam Gali, Jörg Wrachtrup, and Florian Kaiser. Spin-controlled generation of indistinguishable and distinguishable photons from silicon vacancy centres in silicon carbide. *Nature Communications*, 11(1):2516, May 2020.

[91] Naoya Morioka, Di Liu, Öney O. Soykal, Izel Gediz, Charles Babin, Rainer Stöhr, Takeshi Ohshima, Nguyen Tien Son, Jawad Ul-Hassan, Florian Kaiser, and Jörg Wrachtrup. Spin-optical dynamics and quantum efficiency of a single v1 center in silicon carbide. *Phys. Rev. Appl.*, 17:054005, May 2022.

[92] W. J. Munro, K. A. Harrison, A. M. Stephens, S. J. Devitt, and Kae Nemoto. From quantum multiplexing to high-performance quantum networking. *Nature Photonics*, 4(11):792–796, Nov 2010.

[93] Boris Naydenov, Florian Dolde, Liam T. Hall, Chang Shin, Helmut Fedder, Lloyd C. L. Hollenberg, Fedor Jelezko, and Jörg Wrachtrup. Dynamical decoupling of a single-electron spin at room temperature. *Phys. Rev. B*, 83:081201, Feb 2011.

[94] Kae Nemoto, Michael Trupke, Simon J. Devitt, Burkhard Scharfenberger, Kathrin Buczak, Jörg Schmiedmayer, and William J. Munro. Photonic quantum networks formed from nv- centers. *Scientific Reports*, 6(1):26284, May 2016.

[95] P Neumann, R Kolesov, V Jacques, J Beck, J Tisler, A Batalov, L Rogers, N B Manson, G Balasubramanian, F Jelezko, and J Wrachtrup. Excited-state spectroscopy of single nv defects in diamond using optically detected magnetic resonance. *New Journal of Physics*, 11(1):013017, jan 2009.

[96] Philipp Neumann, Johannes Beck, Matthias Steiner, Florian Rempp, Helmut Fedder, Philip R. Hemmer, Jörg Wrachtrup, and Fedor Jelezko. Single-shot readout of a single nuclear spin. *Science*, 329(5991):542–544, 2010.

[97] C. T. Nguyen, D. D. Sukachev, M. K. Bhaskar, B. Machielse, D. S. Levonian, E. N. Knall, P. Stroganov, C. Chia, M. J. Burek, R. Riedinger, H. Park, M. Lončar, and M. D. Lukin. An integrated nanophotonic quantum register based on silicon-vacancy spins in diamond. *Phys. Rev. B*, 100:165428, Oct 2019.

[98] C. T. Nguyen, D. D. Sukachev, M. K. Bhaskar, B. Machielse, D. S. Levonian, E. N. Knall, P. Stroganov, R. Riedinger, H. Park, M. Lončar, and M. D. Lukin. Quantum network nodes based on diamond qubits with an efficient nanophotonic interface. *Phys. Rev. Lett.*, 123:183602, Oct 2019.

[99] Michael A. Nielsen and Isaac L. Chuang. *Quantum Computation and Quantum Information: 10th Anniversary Edition*. Cambridge University Press, 2010.

[100] Adeline Orieux, Marijn A M Versteegh, Klaus D Jöns, and Sara Ducci. Semiconductor devices for entangled photon pair generation: a review. *Reports on Progress in Physics*, 80(7):076001, may 2017.

[101] Albert W. Overhauser. Polarization of nuclei in metals. *Phys. Rev.*, 92:411–415, Oct 1953.

[102] P. K. Pathak and S. Hughes. Coherent generation of time-bin entangled photon pairs using the biexciton cascade and cavity-assisted piecewise adiabatic passage. *Phys. Rev. B*, 83:245301, Jun 2011.

[103] Robert M. Pettit, Farhang Hadad Farshi, Sean E. Sullivan, Álvaro Véliz-Osorio, and Manish Kumar Singh. A perspective on the pathway to a scalable quantum internet using rare-earth ions. *Applied Physics Reviews*, 10(3):031307, 08 2023.

[104] W. Pfaff, B. J. Hensen, H. Bernien, S. B. van Dam, M. S. Blok, T. H. Taminiau, M. J. Tiggelman, R. N. Schouten, M. Markham, D. J. Twitchen, and R. Hanson. Unconditional quantum teleportation between distant solid-state quantum bits. *Science*, 345(6196):532–535, 2014.

[105] Wolfgang Pfaff, Tim H. Taminiau, Lucio Robledo, Hannes Bernien, Matthew Markham, Daniel J. Twitchen, and Ronald Hanson. Demonstration of entanglement-by-measurement of solid-state qubits. *Nature Physics*, 9(1):29–33, Jan 2013.

[106] Matthias Pfender, Nabeel Aslam, Hitoshi Sumiya, Shinobu Onoda, Philipp Neumann, Junichi Isoya, Carlos A Meriles, and Jörg Wrachtrup. Nonvolatile

nuclear spin memory enables sensor-unlimited nanoscale spectroscopy of small spin clusters. *Nat. Commun.*, 8(1), October 2017.

[107] Taras Plakhotnik, Marcus W. Doherty, Jared H. Cole, Robert Chapman, and Neil B. Manson. All-optical thermometry and thermal properties of the optically detected spin resonances of the nv- center in nanodiamond. *Nano Letters*, 14(9):4989–4996, Sep 2014.

[108] M. Pompili, S. L. N. Hermans, S. Baier, H. K. C. Beukers, P. C. Humphreys, R. N. Schouten, R. F. L. Vermeulen, M. J. Tiggelman, L. dos Santos Martins, B. Dirkse, S. Wehner, and R. Hanson. Realization of a multinode quantum network of remote solid-state qubits. *Science*, 372(6539):259–264, 2021.

[109] I. I. Rabi. Space quantization in a gyrating magnetic field. *Phys. Rev.*, 51:652–654, Apr 1937.

[110] Norman F. Ramsey. A new molecular beam resonance method. *Phys. Rev.*, 76:996–996, Oct 1949.

[111] Stephan Ritter, Christian Nölleke, Carolin Hahn, Andreas Reiserer, Andreas Neuzner, Manuel Uphoff, Martin Mücke, Eden Figueroa, Joerg Bochmann, and Gerhard Rempe. An elementary quantum network of single atoms in optical cavities. *Nature*, 484(7393):195–200, Apr 2012.

[112] Lucio Robledo, Lilian Childress, Hannes Bernien, Bas Hensen, Paul F. A. Alkemade, and Ronald Hanson. High-fidelity projective read-out of a solid-state spin quantum register. *Nature*, 477(7366):574–578, Sep 2011.

[113] L J Rogers, M W Doherty, M S J Barson, S Onoda, T Ohshima, and N B Manson. Singlet levels of the nv centre in diamond. *New Journal of Physics*, 17(1):013048, jan 2015.

[114] L J Rogers, R L McMurtrie, M J Sellars, and N B Manson. Time-averaging within the excited state of the nitrogen-vacancy centre in diamond. *New Journal of Physics*, 11(6):063007, jun 2009.

[115] L Rondin, J-P Tetienne, T Hingant, J-F Roch, P Maletinsky, and V Jacques. Magnetometry with nitrogen-vacancy defects in diamond. *Reports on Progress in Physics*, 77(5):056503, may 2014.

[116] Eric I. Rosenthal, Souvik Biswas, Giovanni Scuri, Hope Lee, Abigail J. Stein, Hannah C. Kleidermacher, Jakob Grzesik, Alison E. Rugar, Shahriar Aghaeimeibodi, Daniel Riedel, Michael Titze, Edward S. Bielejec, Joonhee Choi, Christopher P. Anderson, and Jelena Vuckovic. Single-shot readout and weak measurement of a tin-vacancy qubit in diamond, 2024.

[117] Marco Rossignolo, Thomas Reisser, Alastair Marshall, Phila Rembold, Alice Pagano, Philipp J. Vetter, Ressa S. Said, Matthias M. Müller, Felix Motzoi, Tommaso Calarco, Fedor Jelezko, and Simone Montangero. Quocs: The quantum optimal control suite. *Computer Physics Communications*, 291:108782, 2023.

[118] L. G. Rowan, E. L. Hahn, and W. B. Mims. Electron-spin-echo envelope modulation. *Phys. Rev.*, 137:A61–A71, Jan 1965.

[119] E. Schrödinger. Die gegenwã¤rtige situation in der quantenmechanik. *Naturwissenschaften*, 23(48):807–812, Nov 1935.

[120] Arthur Schweiger and Gunnar Jeschke. *Principles of Pulse Electron Paramagnetic Resonance*. Oxford University Press, 05 2001.

[121] Chang S. Shin, Mark C. Butler, Hai-Jing Wang, Claudia E. Avalos, Scott J. Seltzer, Ren-Bao Liu, Alexander Pines, and Vikram S. Bajaj. Optically detected nuclear quadrupolar interaction of ^{14}N in nitrogen-vacancy centers in diamond. *Phys. Rev. B*, 89:205202, May 2014.

[122] Christoph Simon and William T. M. Irvine. Robust long-distance entanglement and a loophole-free bell test with ions and photons. *Phys. Rev. Lett.*, 91:110405, Sep 2003.

[123] P. Siyushev, H. Pinto, M. Vörös, A. Gali, F. Jelezko, and J. Wrachtrup. Optically controlled switching of the charge state of a single nitrogen-vacancy center in diamond at cryogenic temperatures. *Phys. Rev. Lett.*, 110:167402, Apr 2013.

[124] P.-J. Stas, Y. Q. Huan, B. Machielse, E. N. Knall, A. Suleymanzade, B. Pingault, M. Sutula, S. W. Ding, C. M. Knaut, D. R. Assumpcao, Y.-C. Wei, M. K. Bhaskar, R. Riedinger, D. D. Sukachev, H. Park, M. Lončar, D. S. Levonian, and M. D. Lukin. Robust multi-qubit quantum network node with integrated error detection. *Science*, 378(6619):557–560, 2022.

[125] Ph. Tamarat, T. Gaebel, J. R. Rabeau, M. Khan, A. D. Greentree, H. Wilson, L. C. L. Hollenberg, S. Prawer, P. Hemmer, F. Jelezko, and J. Wrachtrup. Stark shift control of single optical centers in diamond. *Phys. Rev. Lett.*, 97:083002, Aug 2006.

[126] T. H. Taminiau, J. Cramer, T. van der Sar, V. V. Dobrovitski, and R. Hanson. Universal control and error correction in multi-qubit spin registers in diamond. *Nature Nanotechnology*, 9(3):171–176, Mar 2014.

[127] T. H. Taminiau, J. J. T. Wagenaar, T. van der Sar, F. Jelezko, V. V. Dobrovitski, and R. Hanson. Detection and control of individual nuclear spins using a weakly coupled electron spin. *Phys. Rev. Lett.*, 109:137602, Sep 2012.

[128] J. M. Taylor, P. Cappellaro, L. Childress, L. Jiang, D. Budker, P. R. Hemmer, A. Yacoby, R. Walsworth, and M. D. Lukin. High-sensitivity diamond magnetometer with nanoscale resolution. *Nature Physics*, 4(10):810–816, Oct 2008.

[129] Anna Tchebotareva, Sophie L. N. Hermans, Peter C. Humphreys, Dirk Voigt, Peter J. Harmsma, Lun K. Cheng, Ad L. Verlaan, Niels Dijkhuizen, Wim de Jong, Anaïs Dréau, and Ronald Hanson. Entanglement between a diamond spin qubit and a photonic time-bin qubit at telecom wavelength. *Phys. Rev. Lett.*, 123:063601, Aug 2019.

[130] Gergő Thiering and Adam Gali. Nuclear spin relaxation in solid state defect quantum bits via electron-phonon coupling in their optical excited state, 2024.

[131] E. Togan, Y. Chu, A. S. Trifonov, L. Jiang, J. Maze, L. Childress, M. V. G. Dutt, A. S. Sorensen, P. R. Hemmer, A. S. Zibrov, and M. D. Lukin. Quantum entanglement between an optical photon and a solid-state spin qubit. *Nature*, 466(7307):730–734, Aug 2010.

[132] David M. Toyli, Charles F. de las Casas, David J. Christle, Viatcheslav V. Dobrovitski, and David D. Awschalom. Fluorescence thermometry enhanced by the quantum coherence of single spins in diamond. *Proceedings of the National Academy of Sciences*, 110(21):8417–8421, 2013.

[133] T. van der Sar, Z. H. Wang, M. S. Blok, H. Bernien, T. H. Taminiau, D. M. Toyli, D. A. Lidar, D. D. Awschalom, R. Hanson, and V. V. Dobrovitski.

Decoherence-protected quantum gates for a hybrid solid-state spin register. *Nature*, 484(7392):82–86, Apr 2012.

[134] Tim van Leent, Matthias Bock, Florian Fertig, Robert Garthoff, Sebastian Eppelt, Yiru Zhou, Pooja Malik, Matthias Seubert, Tobias Bauer, Wenjamin Rosenfeld, Wei Zhang, Christoph Becher, and Harald Weinfurter. Entangling single atoms over 33 km telecom fibre. *Nature*, 607(7917):69–73, Jul 2022.

[135] E van Oort, N B Manson, and M Glasbeek. Optically detected spin coherence of the diamond n-v centre in its triplet ground state. *Journal of Physics C: Solid State Physics*, 21(23):4385, aug 1988.

[136] Rui Vasconcelos, Sarah Reisenbauer, Cameron Salter, Georg Wachter, Daniel Wirtitsch, Jorg Schmiedmayer, Philip Walther, and Michael Trupke. Scalable spin-photon entanglement by time-to-polarization conversion. *npj Quantum Information*, 6(1):9, Jan 2020.

[137] V. Vorobyov, J. Javadzade, M. Joliffe, F. Kaiser, and J. Wrachtrup. Addressing single nuclear spins quantum memories by a central electron spin. *Applied Magnetic Resonance*, 53(7):1317–1330, Sep 2022.

[138] Stephanie Wehner, David Elkouss, and Ronald Hanson. Quantum internet: A vision for the road ahead. *Science*, 362(6412):eaam9288, 2018.

[139] Stephen C. Wein, Juan C. Loredo, Maria Maffei, Paul Hilaire, Abdelmounaim Harouri, Niccolo Somaschi, Aristide Lemaître, Isabelle Sagnes, Loïc Lanco, Olivier Krebs, Alexia Auffèves, Christoph Simon, Pascale Senellart, and Carlos Antón-Solanas. Photon-number entanglement generated by sequential excitation of a two-level atom. *Nature Photonics*, 16(5):374–379, May 2022.

[140] W. K. Wootters and W. H. Zurek. A single quantum cannot be cloned. *Nature*, 299(5886):802–803, Oct 1982.

[141] J. Wrachtrup, S. Ya. Kilin, and A. P. Nizovtsev. Quantum computation using the 13c nuclear spins near the single nv defect center in diamond. *Optics and Spectroscopy*, 91(3):429–437, Sep 2001.

[142] Kangwei Xia, Fiammetta Sardi, Colin Sauerzapf, Thomas Kornher, Hans-Werner Becker, Zsolt Kis, Laszlo Kovacs, Denis Dertli, Jonas Foglszinger, Roman Kolesov, and Jörg Wrachtrup. Tunable microcavities coupled to rare-earth quantum emitters. *Optica*, 9(4):445–450, Apr 2022.

[143] Tianyu Xie, Zhiyuan Zhao, Shaoyi Xu, Xi Kong, Zhiping Yang, Mengqi Wang, Ya Wang, Fazhan Shi, and Jiangfeng Du. 99.92 *Phys. Rev. Lett.*, 130:030601, Jan 2023.

[144] Sen Yang, Ya Wang, D. D. Bhaktavatsala Rao, Thai Hien Tran, Ali S. Momenzadeh, M. Markham, D. J. Twitchen, Ping Wang, Wen Yang, Rainer Stöhr, Philipp Neumann, Hideo Kosaka, and Jörg Wrachtrup. High-fidelity transfer and storage of photon states in a single nuclear spin. *Nature Photonics*, 10(8):507–511, Aug 2016.

[145] Tatsuro Yuge, Susumu Sasaki, and Yoshiro Hirayama. Measurement of the noise spectrum using a multiple-pulse sequence. *Phys. Rev. Lett.*, 107:170504, Oct 2011.

[146] Majid Zahedian, Max Keller, Minsik Kwon, Javid Javadzade, Jonas Meinel, Vadim Vorobyov, and Jörg Wrachtrup. On readout and initialisation fidelity by finite demolition single shot readout. *Quantum Science and Technology*, 9(1):015023, dec 2023.

[147] Majid Zahedian, Vadim Vorobyov, and Jörg Wrachtrup. Blueprint for efficient nuclear spin characterization with color centers. *Phys. Rev. B*, 109:214111, Jun 2024.

[148] Sebastian Zaiser, Torsten Rendler, Ingmar Jakobi, Thomas Wolf, Sang-Yun Lee, Samuel Wagner, Ville Bergholm, Thomas Schulte-Herbrüggen, Philipp Neumann, and Jörg Wrachtrup. Enhancing quantum sensing sensitivity by a quantum memory. *Nature Communications*, 7(1):12279, Aug 2016.

[149] Yifan Zhang, Hao Wu, Xiaodong Yang, Tianyu Xie, Ye-Xin Wang, Chang Liu, Qing Zhao, Jiyang Ma, Jun Li, and Bo Zhang. Robust quantum control for the manipulation of solid-state spins. *Phys. Rev. Appl.*, 19:034068, Mar 2023.

[150] Yunzhe Zheng, Hemant Sharma, and Johannes Borregaard. Entanglement distribution with minimal memory requirements using time-bin photonic qudits. *PRX Quantum*, 3:040319, Nov 2022.

[151] Ádám Gali. Ab initio theory of the nitrogen-vacancy center in diamond. *Nanophotonics*, 8(11):1907–1943, 2019.

Acknowledgments

Well, the chapter of my life called ”PhD” is about to be finished... It was long 6 years full of good and bad moments, these years has changed me a lot, and I hope, in a good way. Here I want to thank all the people, that were around me during this time.
I will start with Professor Dr. Jörg Wrachtrup, whose support and trust I felt throughout the years, even in those moments when I thought I had reached a dead end. Thank you very much for the opportunity to do work at this institute - I have learned a lot during this time, and not only in the context of physics. I also would like to thank Prof. Dr. Peter Michler for being the second examiner and Prof. Dr. Eric Lutz for being the chair of my defense.

Of course, also people, who helped me with the setup itself - I will start with Vadim, who has been by my side since my bachelor's degree in Moscow. Thank you very much, I am sure it would have been much harder to do this PhD without your help. I hope you have a great future in your career as a scientist. Florian, who hired me and, especially in the beginning, helped me a lot with the setup and accommodation in Germany. Certainly, Majid for helping me with the FPGA - it was a key component to make the entanglement working. I'm glad we met - I wish you success in your PhD, and wish you become successful enough to feel at home in fancy places. I hope we will play football together again. Special thanks to Roman, who helped me, a newly started PhD student, to align the setup. Thank you to Rainer, who was very fast responsive and helpful, whenever I asked you for the cleanroom or other type of help. Thanks to Peter, unfortunately we couldn't work for long, but at least I became much better at gluing wire to the sample after your master classes. And thanks to Naoya for his help and responsiveness. Furthermore, I am grateful to Claudia Unger, Dr. Andrea Zappe, Sabrina Jenne, and Marion Moll for managing a solving all the administrative issues I ever had.

I would like to thank all the other PI3 members with whom I have traveled this journey side by side. Jonas, Minsik, Tanya, Rouven, Sreehari, Rita, Farida, Matt, Santo, Malik, Julian, Mario, Tom, Andrew, Joey - Thank you for the pleasant emotions during the lunch seminar and after work, I don't know how I would have managed without you. I am grateful to my friends from Ulm - Ilia, Yuliya, Takuya and Raul. We had a great time traveling and celebrating New Years and Christmas. Special thanks to all my friends, with whom we are separated by distance - Vlad, Luda, Ilya, Dima, Alex, Jane, Dameli, Julia - You were always there, ready to listen and give advice, I am grateful to you for many hours of calls and messages. Of course, my friends, who live in Stuttgart - Veronika, Vlad, Anya, Masha, Sasha, Gosha and Vera - Thank you so much for making my life more interesting and just for being you.

I would like to emphasize the special role of all my teachers, especially my school teachers Михаил Юрьевич и Татьяна Владимировна, who laid the foundation that made this dissertation possible.

И, наверное, самые важные благодарности будут в сторону моей семьи - Папа, Мама, Джавад и Джамал, это были непростые 6 лет для нас, спасибо вам за вашу поддержку. Мне очень повезло родиться в такой замечательной семье. Я вас очень люблю! Еще раз спасибо вам, вы классные! ;)

CV, Dzhavid Dzhavadzade

E-mail: javidjzd@gmail.com

Education

2016-2018 Master of Science (Applied Mathematics and Physics)
Moscow Institute of Physics and Technology (State University)
Department of General and Applied Physics

2012-2016 Bachelor of Science (Applied Mathematics and Physics)
Moscow Institute of Physics and Technology (State University)
Department of General and Applied Physics

List of Publications:

- Coupling of single NV center to adiabatically tapered optical single mode fiber, Vadim V. Vorobyov, Vladimir V. Soshenko, Stepan V. Bolshedvorskii, **Javid Javadzade**, Nikolay Lebedev, Andrey N. Smolyaninov, Vadim N. Sorokin and Alexey V. Akimov; Eur. Phys. J. D 70, 269 (2016).

- Single bright NV centers in aggregates of detonation nanodiamonds Stepan V. Bolshedvorskii, Vadim V. Vorobyov, Vladimir V. Soshenko, Vladimir A. Shershulin, **Javid Javadzade**, Anton I. Zeleneev, Sofya A. Komrakova, Vadim N. Sorokin, Peter I. Belobrov, Andrey N. Smolyaninov, and Alexey V. Akimov; Opt. Mater. Express 7, 4038-4049 (2017)

- Addressing Single Nuclear Spins Quantum Memories by a Central Electron Spin, V. Vorobyov, **Javid Javadzade**, M. Joliffe, F. Kaiser and J. Wrachtrup; Appl Magn Reson 53, 1317–1330 (2022)

- Control of photoluminescence of nitrogen-vacancy centers embedded in diamond nanoparticles coupled to silicon nanoantennas, Anastasiia Zalogina, **Javid Javadzade**, Roman Savelev, Filipp Komissarenko, Alexander Uvarov, Ivan Mukhin, Ilya Shadrivov, Alexey Akimov, Dmitry Zuev; Appl. Phys. Lett. 6 March 2023; 122 (10): 101101 (2023)

- Dopant-assisted stabilization of negatively charged single nitrogen-vacancy centers in phosphorus-doped diamond at low temperatures, Jianpei Geng, Tetyana Shalomayeva, Mariia Gryzlova, Amlan Mukherjee, Santo Santonocito, **Dzhavid Dzhavadzade**, Durga Dasari, Hiromitsu Kato, Rainer Stöhr, Andrej Denisenko, Norikazu Mizuochi, Jörg Wrachtrup; npj Quantum Inf 9, 110 (2023)

- On readout and initialisation fidelity by finite demolition single shot readout, Majid Zahedian, Max Keller, Minsik Kwon, **Javid Javadzade**, Jonas Meinel, Vadim Vorobyov, Jörg Wrachtrup; Quantum Sci. Technol. 9 015023 (2023)

- Efficient nuclear spin - photon entanglement with optical routing, **Javid Javadzade**, Majid Zahedian, Florian Kaiser, Vadim Vorobyov, Jörg Wrachtrup; arXiv:2408.01824 (2024)